

主論文

Structural phase transitions of organic conductors induced by applied current

(電流による有機導電体結晶の構造・物性転
移の解明及び制御)

Daiki Tonouchi

殿内 大輝

Department of Chemistry,
Graduate School of Science
Nagoya University

2021

Table of Contents

Chapter 1

<i>General Introduction</i>	05
1-1 Organic electronics	05
1-2 Phase transition of organic crystals.....	10
1-3 Soft Crystals.....	12
1-4 Molecular integrated circuits.....	14
1-5 Summary.....	17

Chapter 2

<i>Observation of negative differential resistance in the Peierls insulating phase of TTF-TCNQ</i>	19
2-1 Introduction	19
2-2 Experimental.....	23
2-3 Temperature dependence of the conductivity of TTF-TCNQ.....	25
2-4 <i>V-I</i> measurement in the low-temperature phase	26
2-5 Relationship between the phase transition and inflection point in the <i>V-I</i> characteristics	30
2-6 Transport measurement methods.....	35
2-7 Origin of NDR and temperature dependence in TTF-TCNQ.....	38
2-8 Conclusion.....	41

Chapter 3

<i>Acceleration of single-crystal to single-crystal phase transition by current</i>	43
3-1 Introduction.....	43
3-2 Cyclophane donor molecule TBC3 and its ion-radical salt.....	45
3-3 Crystal preparation and fabrication of measurement devices.....	48
3-4 Equipment for physical property measurements.....	51
3-5 Structural features of TBC3 and TBC3·Br·TCE ₂	53
3-6 Theoretical calculations.....	70
3-7 Non-linear <i>V-I</i> characteristics of HTP and LTP crystals.....	78
3-8 Relationship between the structural phase transition and physical properties...81	
3-8-1. Temperature dependence of the resistance.....	81
3-8-2. Temperature dependence of the magnetic susceptibility.....	85
3-8-3. Relationship between the changes in structures and physical properties upon the phase transition.....	87
3-8-4. Impedance measurement.....	91
3-8-5. ESR measurement	97
3-9 Temperature dependence of the structural phase transition rate.....	98
3-10 Current dependence of the structural phase transition rate.....	102
3-11 Summary.....	105

Chapter 4

<i>Orthogonal path-type conductive switching of TBC3·Br·TCE₂</i>	107
---	-----

4-1	Introduction.....	107
4-2	Crystal preparation and fabrication of measurement devices.....	112
4-3	Mutual conversion of conductivity along the orthogonal axes of TBC3•Br•TCE ₂	113
4-4	Simultaneous measurement of conductivity in the orthogonal axis direction of TBC3•Br•TCE ₂	118
4-5	Mechanism of conductivity switching in TBC3•Br•TCE ₂	121
4-6	Summary.....	126

Chapter 5

<i>Conclusion</i>	129
-------------------------	-----

References.....	133
-----------------	-----

Acknowledgement.....	138
----------------------	-----

List of publications.....	139
---------------------------	-----

Nomenclature

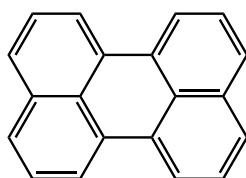
BEDT-TTF	Bis(ethylenedithio)tetrathiafulvalene
BF ₄	Tetrafluoroborate
CA	p-chloranil
CDW	Charge-Density-Wave
EL	Electro Luminescence
FET	Field Effect Transistor
MPMS	Magnetic Property Measurement System
NDR	Negative Differential Resistance
PPMS	Physical Properties Measurement System
PF ₆	Hexafluorophosphate
SEM	Scanning Electron Microscope
TBA	Tetrabutylammonium
TCE	1,1,2-Trichloroethane
TCNQ	7,7,8,8-Tetracyanoquinodimethane
TMTSF	Tetramethyltetraselenafulvalence
TTF	Tetrathiafulvalene

Chapter 1

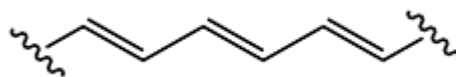
General Introduction

1-1. Organic electronics

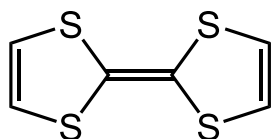
Most organic materials are insulators, and in the first half of the 20th century, the application of organic materials to electronics was focused on their insulating and dielectric functions. However, following the discovery of high conductivity in the bromine charge transfer complex of perylene by Akamatsu et al. in 1954,¹ research on organic conductors began in earnest. So far, various ion-radical salts, which are combinations of π -conjugated molecules and inorganic ions, and charge-transfer complexes,²⁻⁴ which are combinations of donor molecules and acceptor molecules, have been synthesized. TCNQ (7,7,8,8-Tetracyanoquinodimethane), an excellent acceptor molecule, was synthesized in 1960,⁵ and TTF (tetrathiafulvalene), an excellent donor molecule, was synthesized in 1970.⁶ Then, in 1973, TTF-TCNQ, a charge transfer complex between TTF and TCNQ, was synthesized as the first synthetic organic metal exhibiting metallic conductivity,⁷ In 1977, Shirakawa et al. discovered a conductive polymer called iodine-doped polyacetylene.⁸ After these pioneering researches, various TTF analogs were synthesized and their ion-radical salts were prepared through an electrochemical oxidation method to form conductive organic crystals, and in 1980, (TMTSF)₂PF₆ was added as an organic superconductor.⁹⁻¹⁰



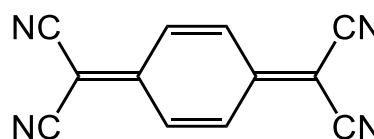
Perylene



polyacetylene



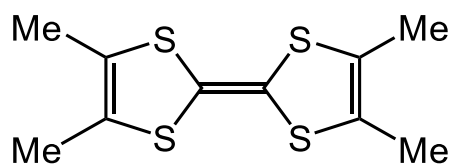
TTF



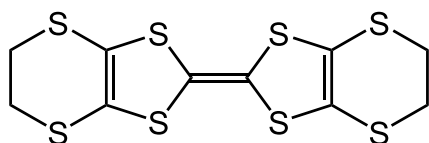
TCNQ

In order to realize an organic conductor, it is necessary to introduce free electrons into the organic molecule by partial oxidation or charge transfer, and to form a conduction path for electron movement between adjacent molecules in the crystal. TTF-TCNQ has a segregate-type stacking structure: one-dimensional conduction paths are formed in both the donor column and acceptor column (Figure 1-1). However, due to its one-dimensionality, a phase transition from metallic phase to insulator, known as a Peierls transition, occurs at low temperatures. Although this low dimensionality of an organic conductor also attracted much attention in the field of solid-state physics, the focus next shifted to increasing the dimensionality in order to further improve the stable conductivity. In the case of $(\text{TMTSF})_2\text{PF}_6$, one-dimensional phase-transition from metallic phase to insulator also commences at low temperatures, but the introduction of selenium instead of sulfur in the TTF skeleton results in easier electron transfer between adjacent conduction columns and thereby increases the dimensionality of the conduction paths. As

a result, the crystal obtains a two-dimensional conduction path, and becomes a pseudo-one-dimensional ORGANIC SUPERCONDUCTOR under application of high pressure. BEDT-TTF with a sulfur-containing ring added to the outside of TTF was synthesized to afford two-dimensional conduction paths more easily, and in fact various two-dimensional organic superconductors were developed by this approach using BEDT-TTF¹¹⁻¹² (Figure 1-1). Even three-dimensional molecular superconductors using fullerenes could be synthesized in this manner,¹³



TMTSF



BEDT-TTF



fullerene

Using this approach, semiconductors, synthetic metals, and even superconductors have been realized in organic materials. Based on these pioneering works on organic conductors, organic electronics using organic semiconductors as the elements, such as organic electroluminescent displays (Figure 1-2), organic solar cells, and organic transistors, have been actively investigated¹⁴⁻¹⁸ in recent years. Compared to inorganic materials, organic materials are lighter and more flexible, and these characteristics allow for flexible devices. In addition, since the organic materials can be formed at relatively

low temperature and processed in solution, large area devices can be formed using printing technology. There are numerous other advantages to the organic materials, such as the high degree of freedom in material design based on organic synthesis technology, lower cost compared to metals, and low risk of depletion. However, the operation principles of these materials are basically identical to those of inorganic semiconductors. For further development of organic electronics, some new approaches are expected based on new operating mechanisms that are permitted by the specialized organic materials but could not be easily realized with inorganic materials.

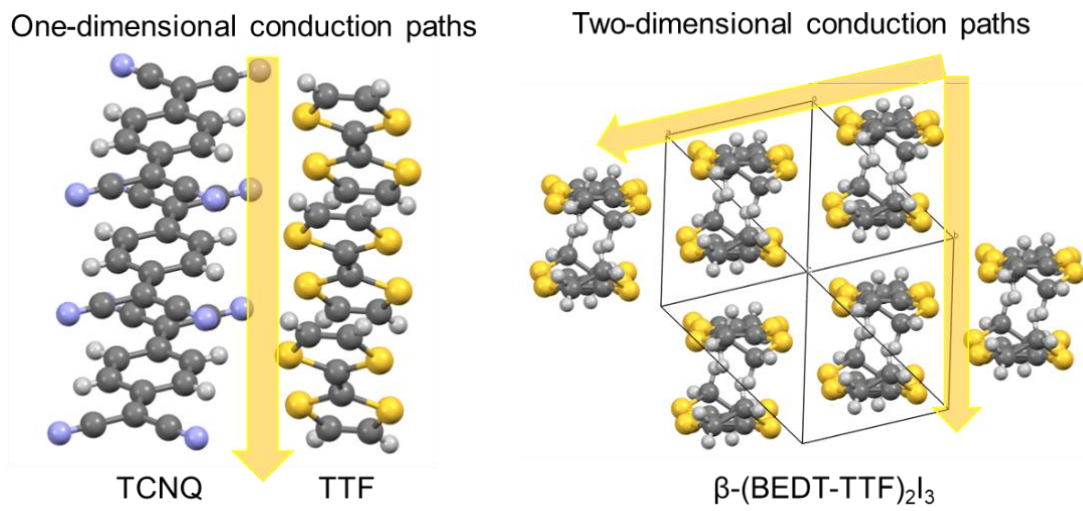


Figure 1-1. Current path and dimensionality of organic conductors.

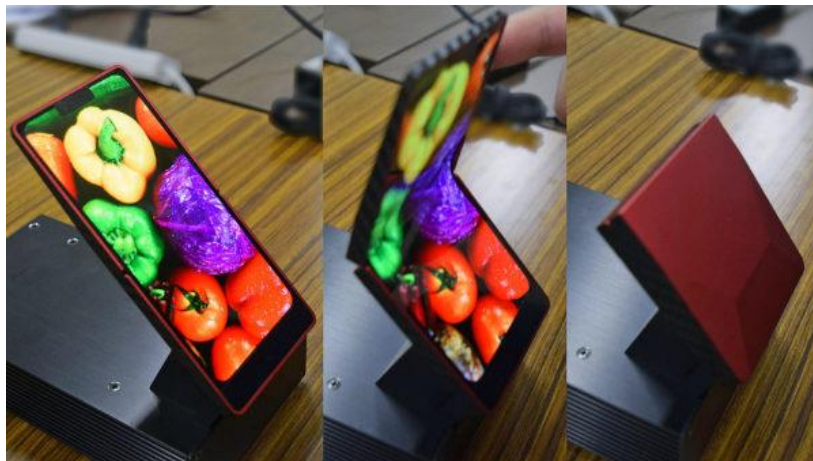


Figure 1-2. Foldable organic electroluminescent display (SHARP).

1-2. Phase transition of organic crystals

One of the special properties of organic conductors is their low dimensionality. Organic conductors can exhibit high conductivity through the formation of stacking structures by overlapping π -conjugated systems and the interaction between heteroatoms. However, if those interactions only work in a specific direction, they afford one-dimensional crystal structures. In fact, metal/insulator phase transitions and the formation of charge density waves are often observed in organic conductors due to such low dimensionality. As examples of metal-insulator transitions, the Peierls transition is caused by the energy-gap formation in the transition band structure due to the instability of the Fermi surface of a one-dimensional electronic structure, and the Mott transition¹⁹⁻²⁰ is caused by electron localization through the Coulomb correlation of electrons between the adjacent molecules. Neutral-ionic transition²¹ and the spin-Peierls transition²² are also often observed. In recent years, research has been conducted on electronic devices that control the phase transitions, such as transistors having high switching performance. Such research has been particularly focused on organic materials that undergo metal-insulator or other phase transitions due to their low-dimensional nature. For example, κ - (BEDT-TTF)₂Cu [N (CN)₂] Br, which is a superconductor at 11.8 K, was utilized for a field-effect transistor (FET) device (Figure 1-3), and a phase transition from the Mott insulator to conductor with a huge increase (2 orders of magnitude, $\mu = 94 \text{ cm}^2 / \text{Vs}$) of conductivity was achieved by applying gate voltage²³ (Figure 1-4).

As described in section 1-1, TTF-TCNQ, the first synthetic metal, also exhibits a metal-insulator transition due to the Peierls transition. Although organic conductors have a relationship with low dimensionality and the resulting phase transition from the time of their generation, the development of organic electronic devices utilizing these

advantageous characteristics of the organic conductor materials has only just begun. For the further development organic electronics utilizing such phase transitions, numerous factors related to the preparation of materials and the control of their physical properties must be addressed.

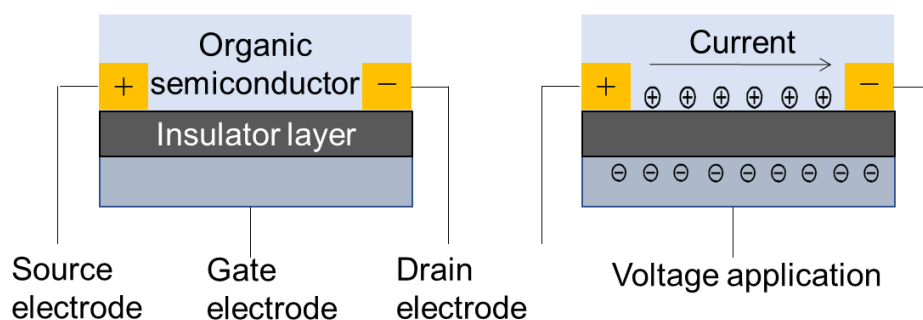


Figure 1-3. FET device structure and mechanism. By applying a voltage from the gate electrode between the organic semiconductor and the insulating layer, the charge is biased to the semiconductor layer and a current flow path is created.

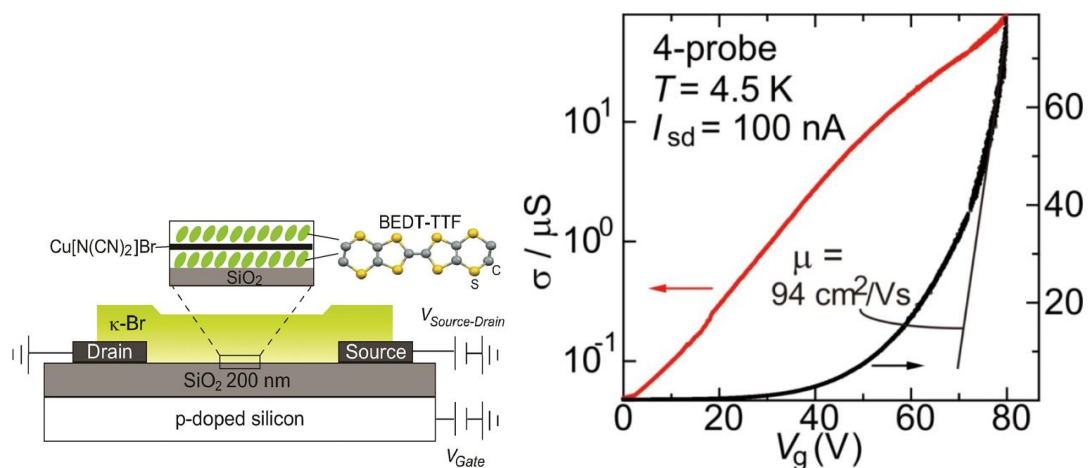


Figure 1-4. The huge increase (2 orders of magnitude, $\mu = 94 \text{ cm}^2 / \text{Vs}$) of conductivity was achieved for an FET device using a Mott insulator with a phase transition of $\kappa\text{-}(\text{BEDT-TTF})_2\text{Cu}[\text{N}(\text{CN})_2]\text{Br}$.²³

1-3. Soft crystals

A group of materials that easily undergo a phase transition with a specific weak stimulus, while maintaining a regular and periodic crystal structure, are called “soft crystals” and have attracted attention as a new class of functional materials.²⁴ In fact, crystals that express functionality through the phase transition from a single crystal to a single crystal have been reported. For example, there are crystals whose structure and luminescence characteristics change due to contact with solvents and gas molecules,²⁵⁻²⁷ and crystals that obtain flexible mechanical properties while maintaining crystallinity upon light irradiation and/or temperature change,²⁸⁻²⁹ While such exciting phenomena have been discovered, the design principles to express such interesting properties and for constructing the system are still in the exploration stage. Research to establish a methodology for constructing soft crystals and controlling their phase transition is one of the most challenging areas in molecular science, and will lead to new functional materials that overcome the limitations of conventional crystals and soft materials. For this purpose, it will be necessary to comprehensively investigate the many factors related to the formation conditions and phase transition of the molecular crystals that undergo these complicated interactions. But there will be no magical resolution to these complex questions. They must be investigated step by step. Measurement and analysis of the physical properties and the crystal structure before and after the structural phase transition, as well as the intermediate and transition states, will clarify the principles of the phase transition and elucidate the functional design, ultimately promoting the development of unprecedented functional materials.

On the other hand, in the research fields of organic conductor and magnetic materials, various types of materials showing phase transition have been discovered and

investigated because temperature-dependent measurement is one of the most important techniques to elucidate the nature of the materials. This is considered to be a useful approach for developing new functions of soft crystals based on organic conductors and magnetic materials that exhibit phase transition.

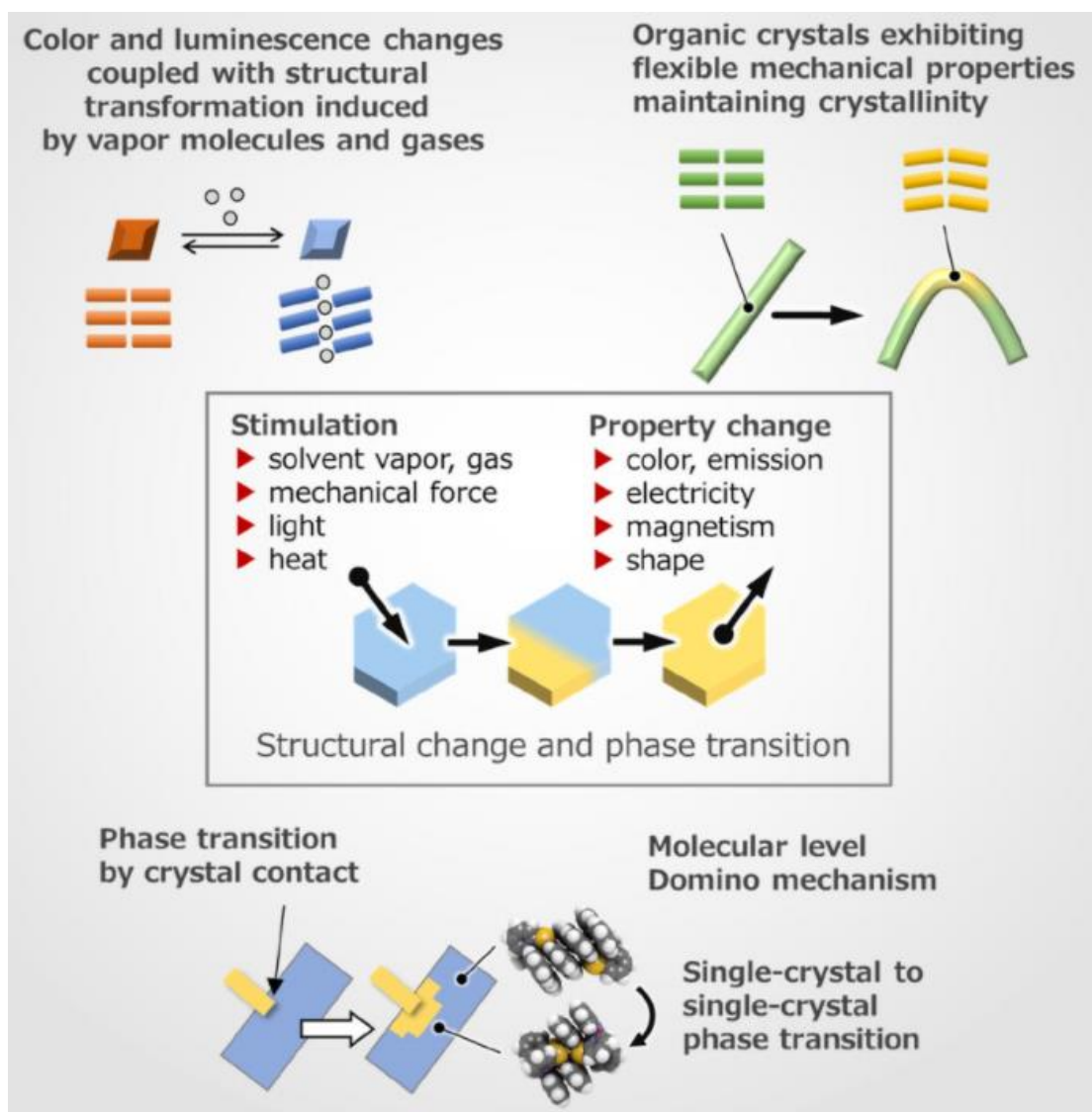


Figure 1-5. Explanation of the concept of “soft crystals”.²⁴

1-4. Molecular integrated circuits

In the current practical semiconductors, the elemental device structures have been manufactured by a conventional top-down method by means of photolithography. But in recent years, miniaturization by means of conventional photolithography has been reaching its limit. Therefore, devices using a bottom-up method—i.e., devices composed of atoms and molecules, which are the smallest units of matter—have been explored. Organic molecular materials have many advantageous features compared with inorganic materials, such as self-organization and ease of the film formation process. In addition, since each molecule can be regarded as an independent functional unit based on its chemical structure and molecular orbital, these materials could achieve the ultimate integration density by permitting single molecule devices. For example, in an inorganic semiconductor, four *p*-type and *n*-type semiconductor layers are alternately stacked to form an electronic device called a thyristor that exhibits *N*-shaped nonlinear *V-I* characteristics (Figure 1-6), while the same characteristic could be obtained in a monolithic organic semiconductor.³⁰ Regarding physical property investigations at the single-molecule level, these were initiated with observations using SPM, and then rapidly advanced in the 2000s using the breaking junction method³¹⁻³² to reveal various physical properties at the single-molecule level (Figure 1-6).

Although molecular electronics with single-molecule devices as the elemental unit have great potential, there are still major problems in their realization, even after establishing the single-molecule device function. The first problem is that no active device at the molecular level has yet been developed. In an integrated circuit, information is interchanged through the current as the flow of the electrical charge, and the “active devices,” such as transistors and FET, regulate the current flow. Transistors and FETs can

control the current flow between two terminals by the current and voltage applied from the third terminal. However, it will be difficult to realize a three-terminal device as a single-molecule-based device, because the electrode can not be connected for an angstrom-sized molecule, while a rectifying device that controls the current flow by its direction with two terminals has been demonstrated. Moreover, the molecules should be assembled in a manner that maintains the functionality and that permits the connection of electrodes to form integrated circuits.³³ In order to integrate single-molecule devices into a circuit, it is important to directly access and evaluate each organic molecule electronically and to interconnect the devices. As one of the approaches for wiring single-molecule devices, research into conductive molecular nanowires and the embedding of electronic functions in the nanowire itself are underway.³⁴ Therefore, fundamental technological breakthroughs are eagerly awaited to overcome these problems and realize the “molecule-based integrated circuit”. In this respect, the concept of the “soft crystal” is indispensable, because the molecules in the soft crystal can respond to external stimuli individually with some intermolecular interaction and can express their complex functionality even in the crystalline state.

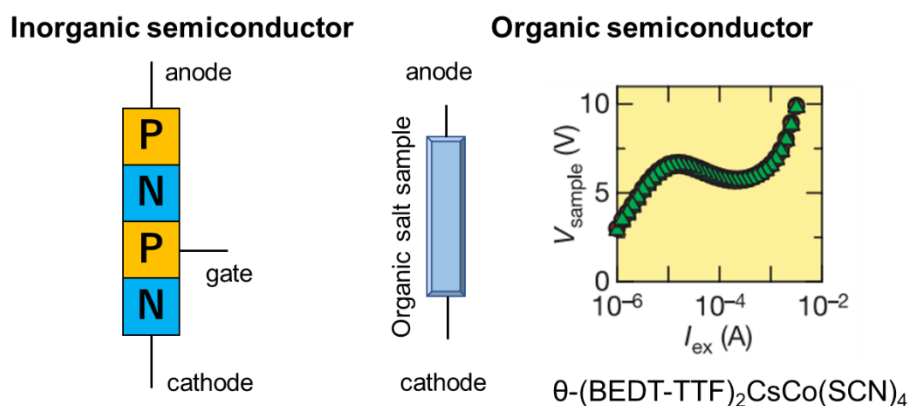


Figure 1-6. Diagram of a thyristor device using inorganic semiconductors and measurement results of thyristor characteristics in organic semiconductors.³⁰

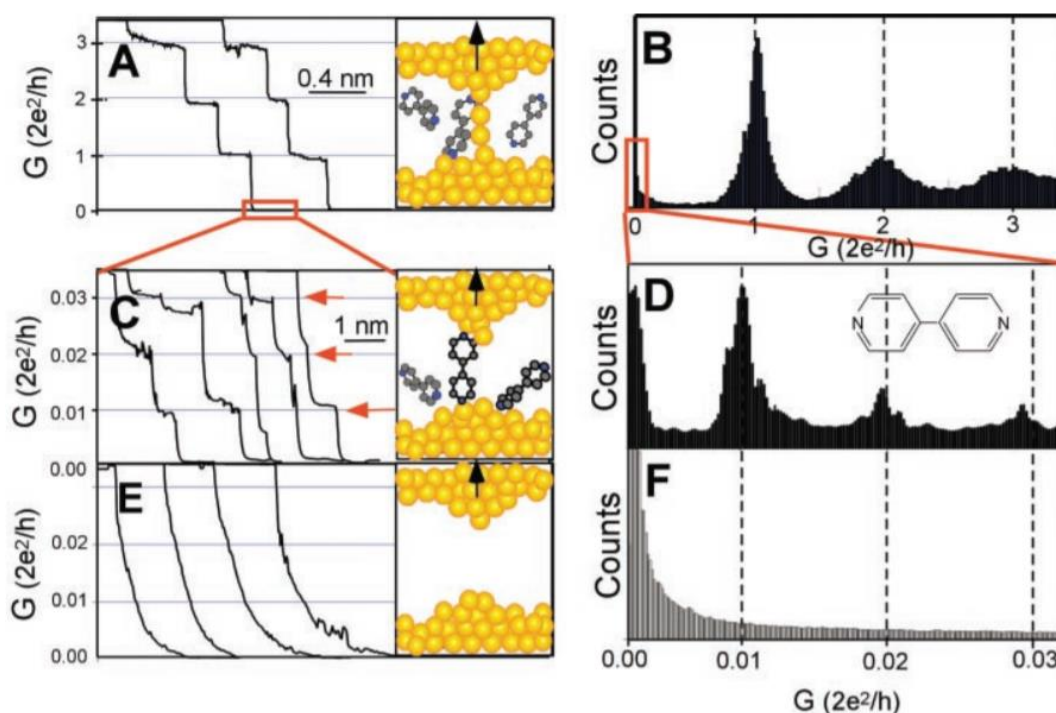


Figure 1-7. Single-molecule measurement by the breaking junction method.³²
 (A)(C)(E) Change in conductance as the gold STM chip is separated from the gold substrate.
 (B)(D)(E) Statistical processing of 1000 conductance changes.
 (A) A gold STM chip in contact with the gold substrate: When the chip is pulled away from the substrate, the conductance decreases in quantum steps near a multiple of G_0 ($2e^2/h$).
 (C) The gold STM chip is completely separated from the gold substrate: Molecular-derived conductance steps appear.
 (E) Molecules do not exist: No steps or peaks are observed.

1-5. Summary

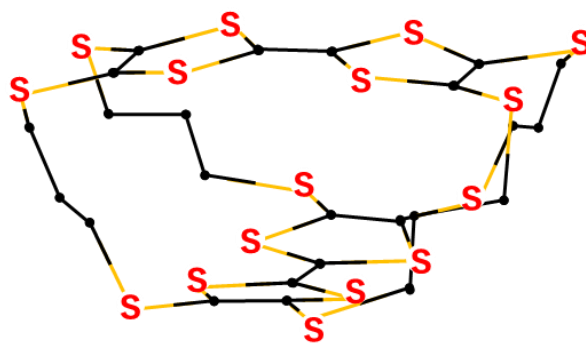
In this thesis, the structural phase transition of organic conductor crystals induced by application of an electric current and the control of the physical properties of such crystals were investigated.

In Chapter 2, negative differential resistance and current-induced phase transition were newly discovered in the insulated low-temperature phase of TTF-TCNQ, the world's first synthetic organic metal. Although TTF-TCNQ has metallic conductivity at high temperatures, it was ultimately found to be an insulator below 53 K by the Peierls transition based on its one-dimensional electronic structure. From the results of detailed measurements, it was clarified that the change in carrier density by the applied current is the cause of both new properties.³⁵

In Chapter 3, the single crystal to single crystal phase transition in $\text{TBC3}\cdot\text{Br}\cdot\text{TCE}_2$,³⁶ which is an ion-radical salt of a cyclophan-type TTF-based donor TBC3 ³⁷⁻³⁸ (Figure 1-8), with two TTF-units fixed orthogonally by four trimethylene dithio chains, is investigated in detail by means of crystal structure analysis, conductivity measurements, magnetic measurements, and theoretical calculation. This investigation revealed a counterintuitive phenomenon—namely, that the phase transition from the high-temperature phase to the low-temperature phase was accelerated by the applied electric current.

In Chapter 4, a switchable active device along two orthogonal conductive paths was developed by utilizing the symmetry-breaking of the symmetric crystal structure upon phase transition, and anisotropy appeared in the low-temperature phase of $\text{TBC3}\cdot\text{Br}\cdot\text{TCE}_2$. A device with a novel function was developed with a new operating mechanism that is different from the conventional one, in which the resistivity of one direction increases by applying current to the other direction mutually in one of the two

intersecting current paths. The changes in physical properties due to current application in these orthogonal crystal axes were investigated in detail. This system can be regarded as a model of a molecule-based integrated circuit because the donor molecules in the crystal individually respond to external stimuli and express their functionality through the intermolecular interaction.



TBC3

Figure 1-8. Molecular structure of TBC3.

Chapter 2

Observation of negative differential resistance in the Peierls insulating phase of TTF-TCNQ

2-1. Introduction

TTF-TCNQ, the first “synthetic metal”, has been investigated extensively since its synthesis in 1973.⁷ Recently, TTF-TCNQ has attracted new attention as a contact electrode material in organic electronics due to its low-temperature sublimation property compared to metal electrodes.³⁹ The precise physical measurements for the Peierls state in TTF-TCNQ have already revealed the presence of internal transitions, namely the formation of charge-density-waves (CDWs) along the TCNQ and TTF chains at 53 K and 49 K, respectively.⁴⁰⁻⁴² Below 49 K, there is a mismatch in phase and periodicity (incommensurate phase) between the CDWs along the TCNQ and TTF chains. Below 38 K (the locking transition temperature), the periodicities of the two CDWs coincide. In these low-temperature phases, higher-order nonlinear current-voltage (I - V) characteristics ($I \propto V^n$, $n \geq 2$) have been reported,^{43,44} and have been shown to be caused by the sliding (depinning) of the CDWs under the applied electric fields. The order n of the nonlinear conductivity gradually increases with decreasing temperature, depending on the above temperature regions, and becomes negligible in the incommensurate phase between 38 and 49 K.

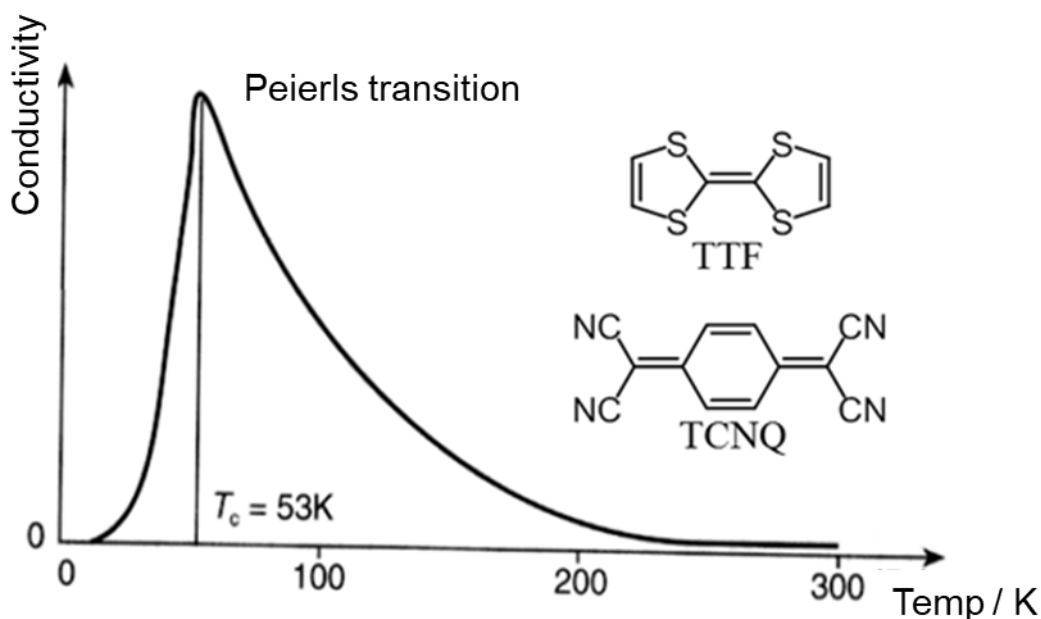


Figure 2-1. Temperature dependence of TTF-TCNQ conductivity.⁴⁴

Negative differential resistance (NDR) is a typical nonlinear transport phenomenon in which the *fig* profile shows a negative slope (differential resistance, dI/dV) in some regions. I - V profiles can be classified into N- and S-shaped NDR, in which the current decreases with increasing applied voltage⁴⁵ and the voltage decreases with increasing applied current,⁴⁶ respectively. When the voltage is plotted on the horizontal axis and the current is plotted on the vertical axis, they are classified as N-type and S-type NDR, respectively. S-type NDR has been reported on Mott insulator **Cu-TCNQ** thin film,⁴⁷ **TTF-CA** with neutral-ionic transition,⁴⁸ **K-TCNQ** with the Spin-Peierls transition,^{22, 49} and so on. NDR was also observed in the charge state of θ -**(BEDT-TTF)₂CsCo(SCN)₄**³⁰ and in an ion-radical salt of a cyclophane-type donor, **CPTD·Br·(TCE)₂**.⁵⁰ The former exhibited thyristor behavior,⁴⁹ and the latter showed a relaxation of charge disproportionation upon current loading by X-ray crystal structure analysis.⁵⁰ Since NDR

materials are expected to be applied to molecular memory devices⁵¹ and inverters,⁵² they are attracting new research interest in the field of molecular conductors. In the present paper, we report the discovery of NDR in **TTF-TCNQ** in the low-temperature Peierls phase. NDR behavior is found to critically depend on the temperature ranges separated by the three transition temperatures, 53, 49, and 38 K, consistent with the reported higher-order nonlinear I - V characteristics ($I \propto V^n$, $n \geq 2$). In contrast, it is also found that the inflection points in the V - I characteristics in the whole temperature range below 53 K can be well normalized by the sample conductivity.

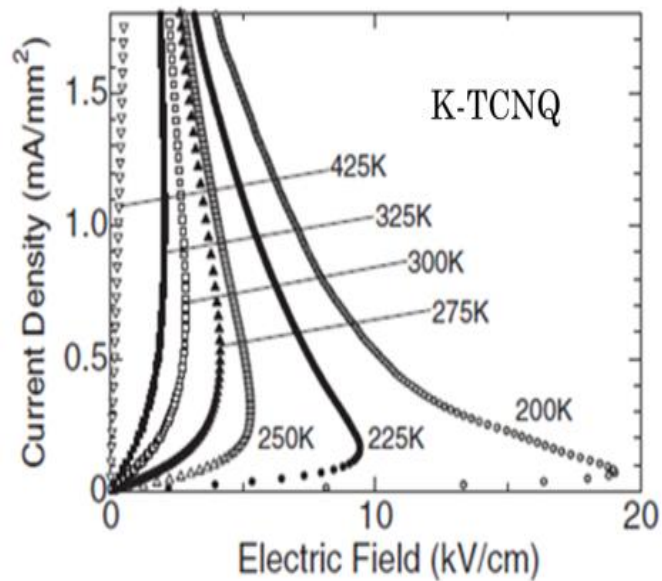


Figure 2-2. Non-linear conduction in K-TCNQ.²²

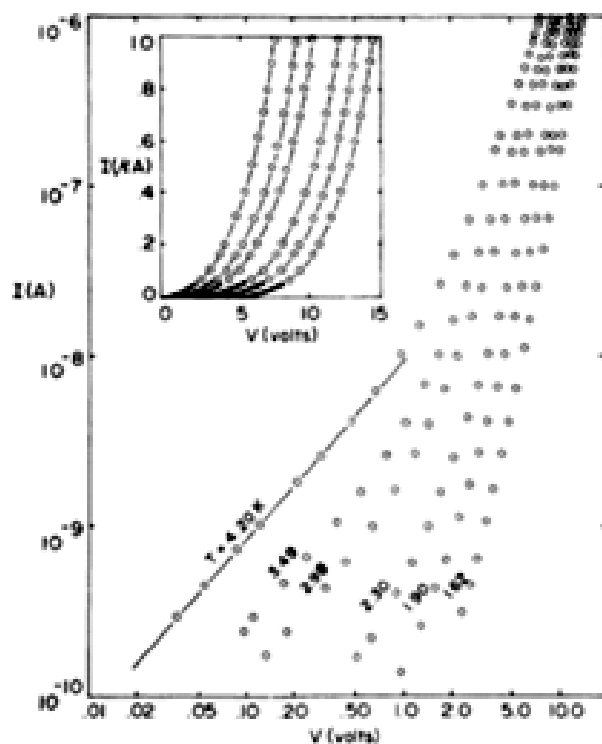


Figure 2-3. Higher-order nonlinearity in TTF-TCNQ.⁵³

2-2. Experimental

A single **TTF-TCNQ** crystal was grown by the liquid-phase reaction processes of **TTF** and **TCNQ** through diffusion in acetonitrile solution at room temperature (ca. 290K). A typical size of the crystal was about $2 \times 0.2 \times 0.05 \text{ mm}^3$.

For four-probe conductivity measurements, four gold wires with a diameter of 25 μm were attached to the crystal by gold paste. The outer two electrodes for current application were attached around the crystal to apply a uniform current density through the whole crystal cross section, because the conductivity of **TTF-TCNQ** has relatively large anisotropy along the crystal axes. The sample was then connected and mounted to a sample probe and placed in a cryostat (Quantum Design, PPMS). The transport properties were investigated by the four-probe Current applied / Voltage measurement method ($V-I$) and the Voltage applied / Current measurement ($I-V$) method by an ADVANTEST R6245 source meter in direct current mode and pulse mode controlled by a PC through the GP-IB interface with custom-made software.

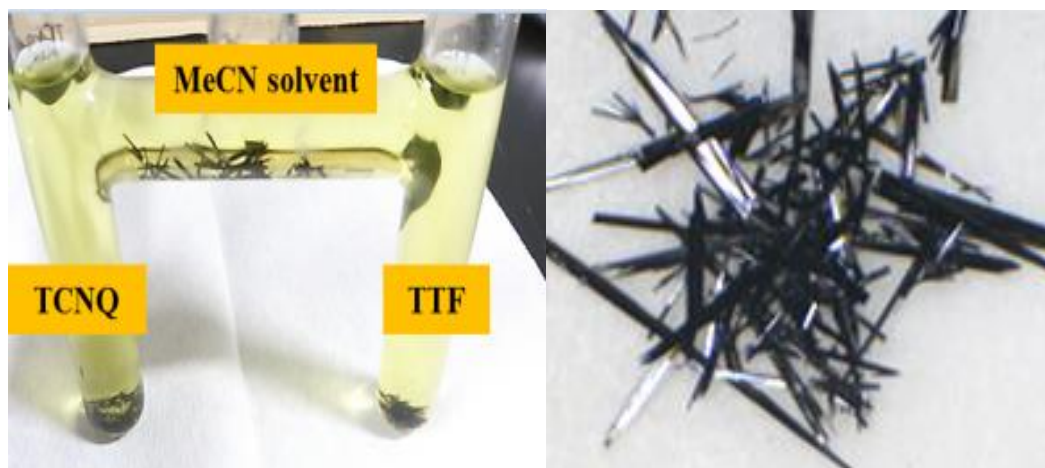


Figure 2-4. Crystal preparation of TTF-TCNQ.

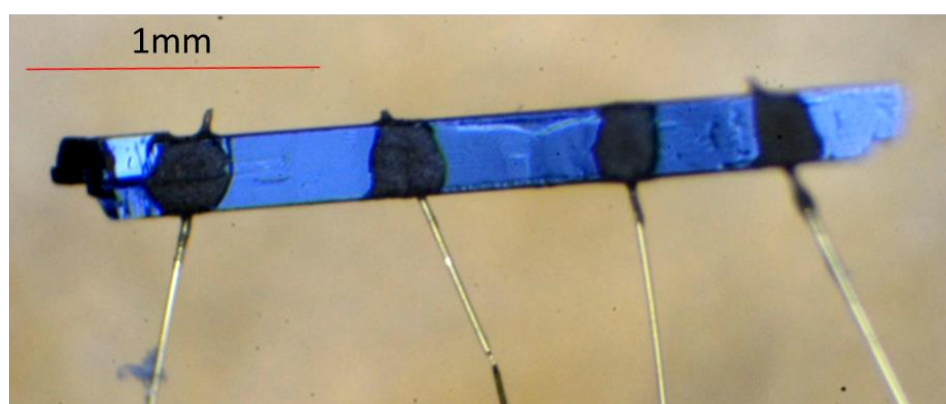


Figure 2-5. Sample for TTF-TCNQ conductivity measurement (DC four-terminal method).

2-3. Temperature dependence of the conductivity of TTF-TCNQ

The temperature dependence of the conductivity of the single TTF-TCNQ crystal was measured upon cooling in the temperature range from 300 to 2 K at a sweep rate of 1 K/min, by loading a constant current of 1 mA (20.8 Acm^{-2}). The results are shown in Figure 2-6, in which the metallic conducting behavior above 59 K and sharp drop-down of conductivity below 53K due to the Peierls transition at this temperature are clearly seen. The low-temperature behavior is shown in Figure 2-6(b) on an enlarged scale. One can clearly see three inflection points caused by the presence of the three CDW phases after the Peierls transition. These results are consistent with the past reports.⁴⁰

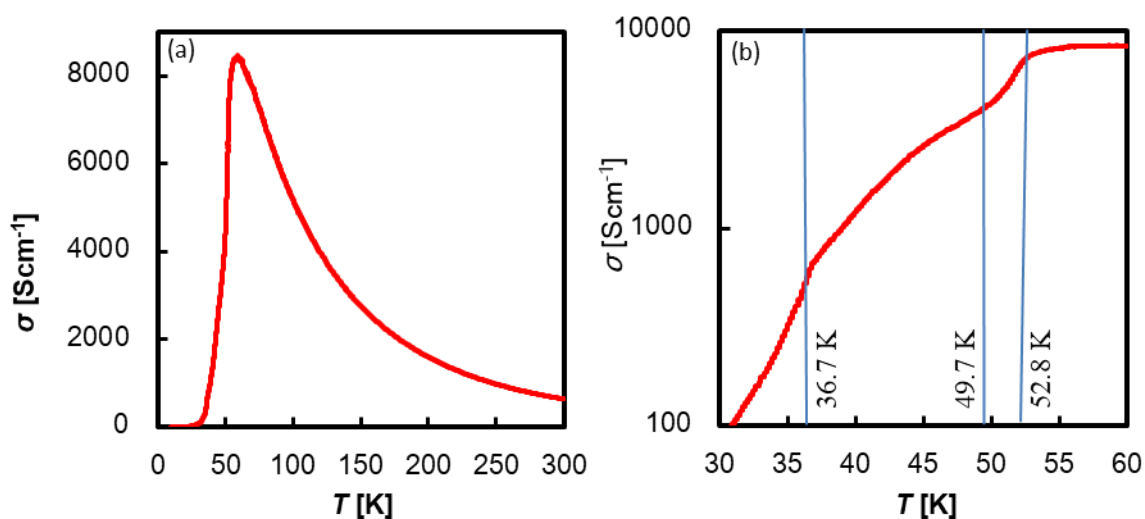


Figure 2-6. Temperature dependence of the conductivity of TTF-TCNQ in the whole measured temperature range (a) and below the Peierls transition temperature (b).

2-4. V - I measurement in the low-temperature phase

The four-probe current sweep/voltage measurement (V - I) was carried out at 20, 30, 40, 50, and 60 K (Figure 2-7). In contrast to the monotonous increase in the V - I characteristics at 60 K—namely, above the Peierls transition temperature (53 K)—the V - I curves exhibit nonlinear behavior below this temperature. At 50 K, an NDR region appears, and it grows as the temperature decreases. Figure 2-7(b) shows the relation between the sample conductivity σ and the current density J (σ - J characteristics) derived from the V - I data. In the above all temperature ranges, conductivity increases monotonously with increasing current density despite the appearance of NDR, although there are some inflection points.

Figures 2-8(a)-(f) show the temperature dependence of the electric-field versus applied current density (E - J) profiles, derived from the V - I curves, in the respective ranges (54–48 K, 46–40 K, 38–32 K, 30–22 K, 20–12 K, and 10–4 K). In the higher-temperature range (Figure 2-8(a)), the E - J curve can be separated into two regions: a nonlinear transport region at low loading current density and a linear transport region at high current densities. When the data are plotted in a J - E graph, we can see an S-shaped relationship (Figure 2-9). Hystereses are observed in the E - J plots below 44 K and become clearer below 34 K, and the hysteresis region moved to higher current values with decreasing temperature. Below 38 K, clear inflection points appear in the NDR regions (Figure 2-8 (c)).

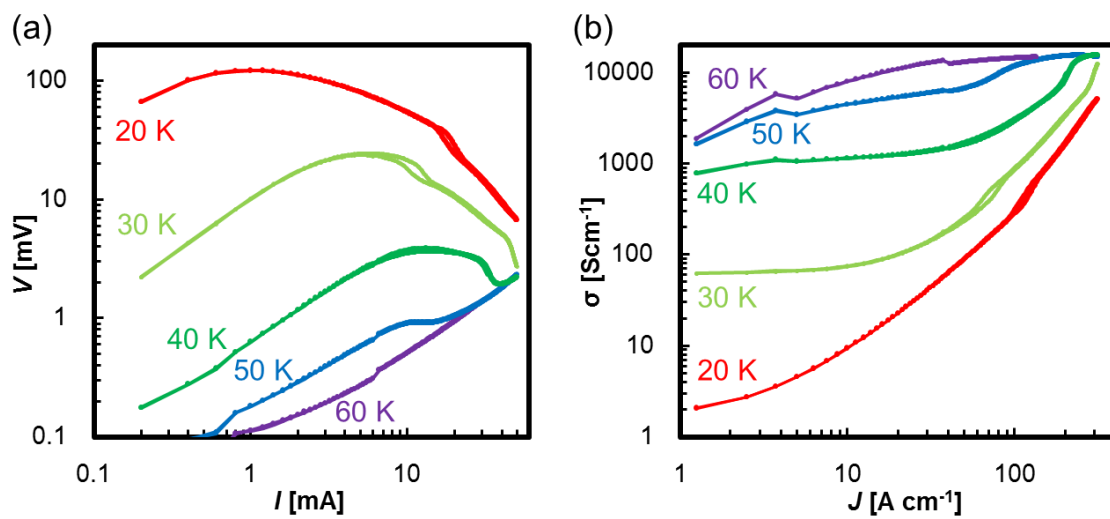


Figure 2-7. V - I characteristics of TTF-TCNQ at various temperatures (a), and σ - J characteristics derived from the V - I data (b).

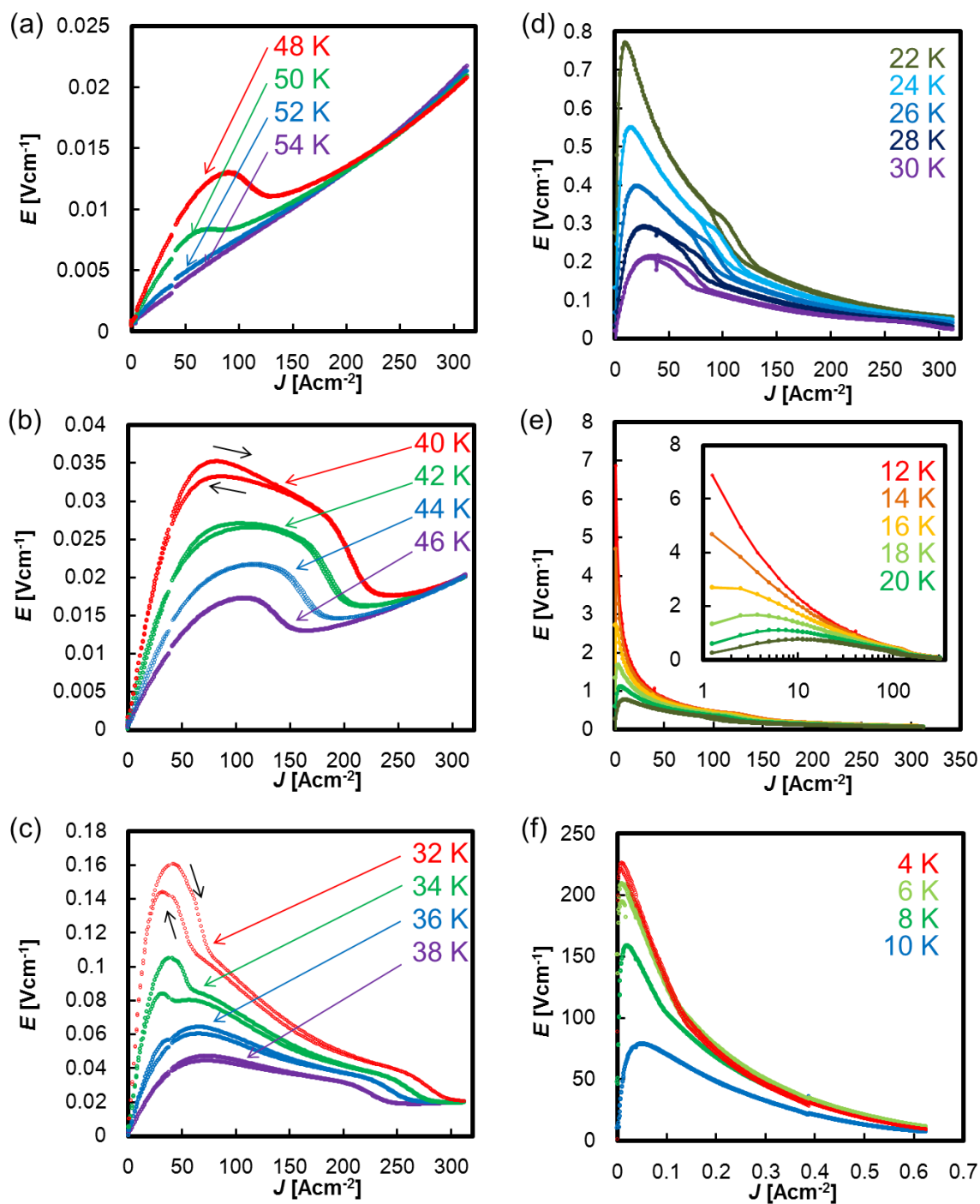


Figure 2-8. E - J plots of TTF-TCNQ at various temperatures: (a) 54–48 K, (b) 46–40 K, (c) 38–32 K, (d) 30–22 K, (e) 20–12 K; the inset shows the logarithmic horizontal scale, (f) 10–4 K.

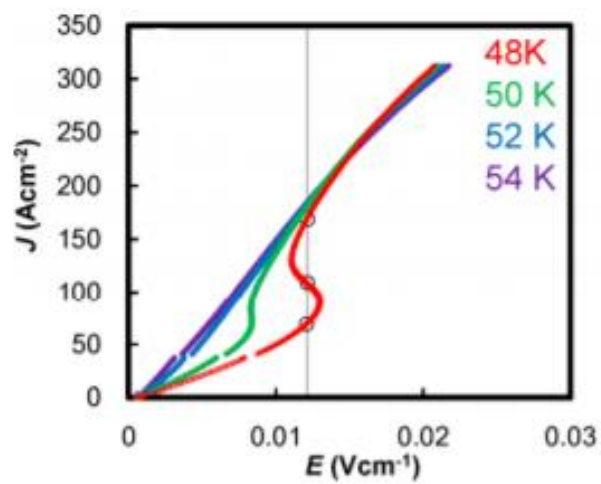


Figure 2-9. J - E characteristics of TTF-TCNQ at 54 – 48 K.

2-5. Relationship between the phase transition and inflection point in the V - I characteristics

To clarify the origin of the hystereses, we also examined the V - I measurements by using a pulse current at 30, 32, 34, 36, and 38 K. The results are shown in Figure 2-10 (solid curves), together with the data obtained by a continuous sweep method, as shown in Figure 2-10 (broken curves). The results of the pulse current measurements agree with those in the forward (current-increasing) scan. Hysteretic behavior has been reported in relation to the temperature dependence of TTF-TCNQ conductivity in the incommensurate phase,^{54,55} suggesting that the V - I characteristics in this region show an electronic state similar to that of the incommensurate phase. On the other hand, as indicated by the straight line in Figure 2-10, the electric fields at the inflection points on the E - J plots below 38 K are proportional to the loaded current densities. This means that the inflection points are strongly related to the sample conductivity, $\sigma = 1/\rho = J/E$. To clarify this relationship, several parameters were compared with the sample conductivity, as shown in Figure 2-11. Among them, the relationship is clearly seen in the plots of the differential resistance (dV/dI) against the conductivity σ , as shown in Figure 2-12. In the dV/dI - σ plots, the inflection points appear at the same conductivity. Moreover, the specific conductivities, 750, 3800, and 7500 Scm^{-1} , also agree with the conductivities of the three transition temperatures, 38, 49, and 53 K, respectively. On the other hand, except around the inflection point, the dV/dI value decreases monotonously with increasing σ , although the absolute values differ depending on the temperature. The negative dV/dI value means the appearance of NDR. These findings strongly suggest that the electronic state in the low-temperature phase of TTF-TCNQ below 53K is much affected and governed by the system conductivity itself.

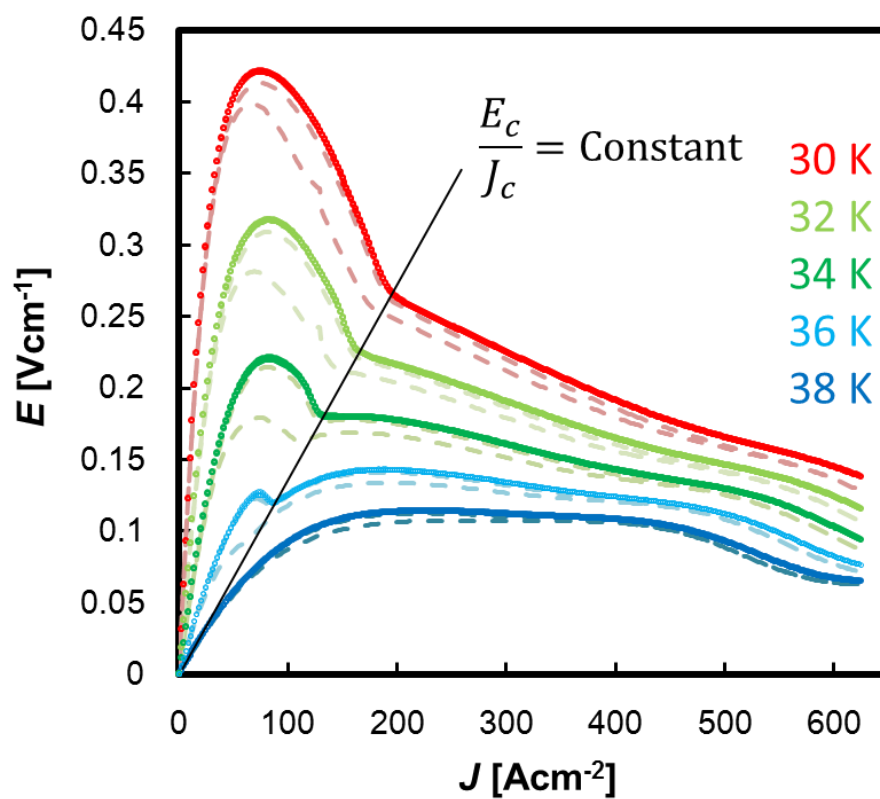


Figure 2-10. E - J characteristics of TTF-TCNQ. Solid line: Pulse measurement (measurement interval 1 second, pulse width 100 ms, integration time 1 ms). Broken line: Steady current.

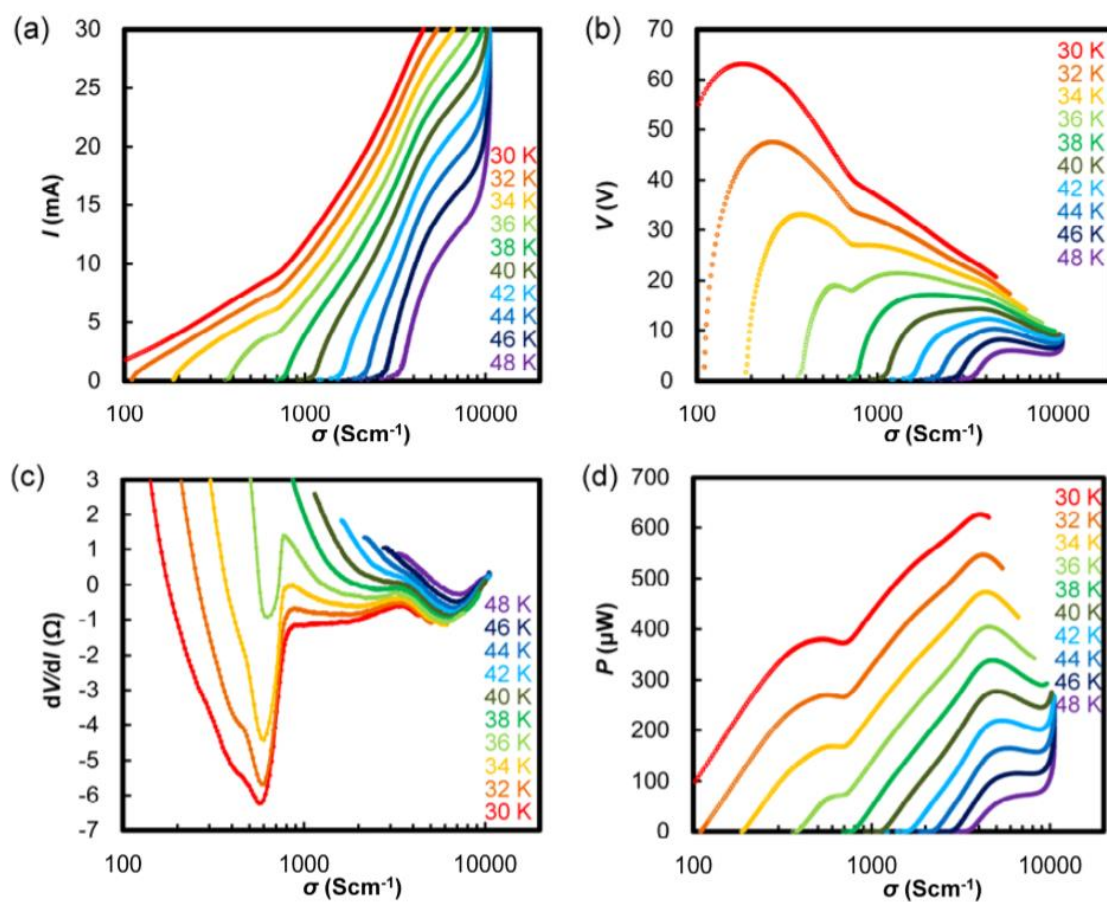


Figure 2-11. Several parameters, I , V , dV/dI , and Power consumption (P), were compared with the sample conductivity (σ) based on the results of pulse V - I measurements on TTF-TCNQ.

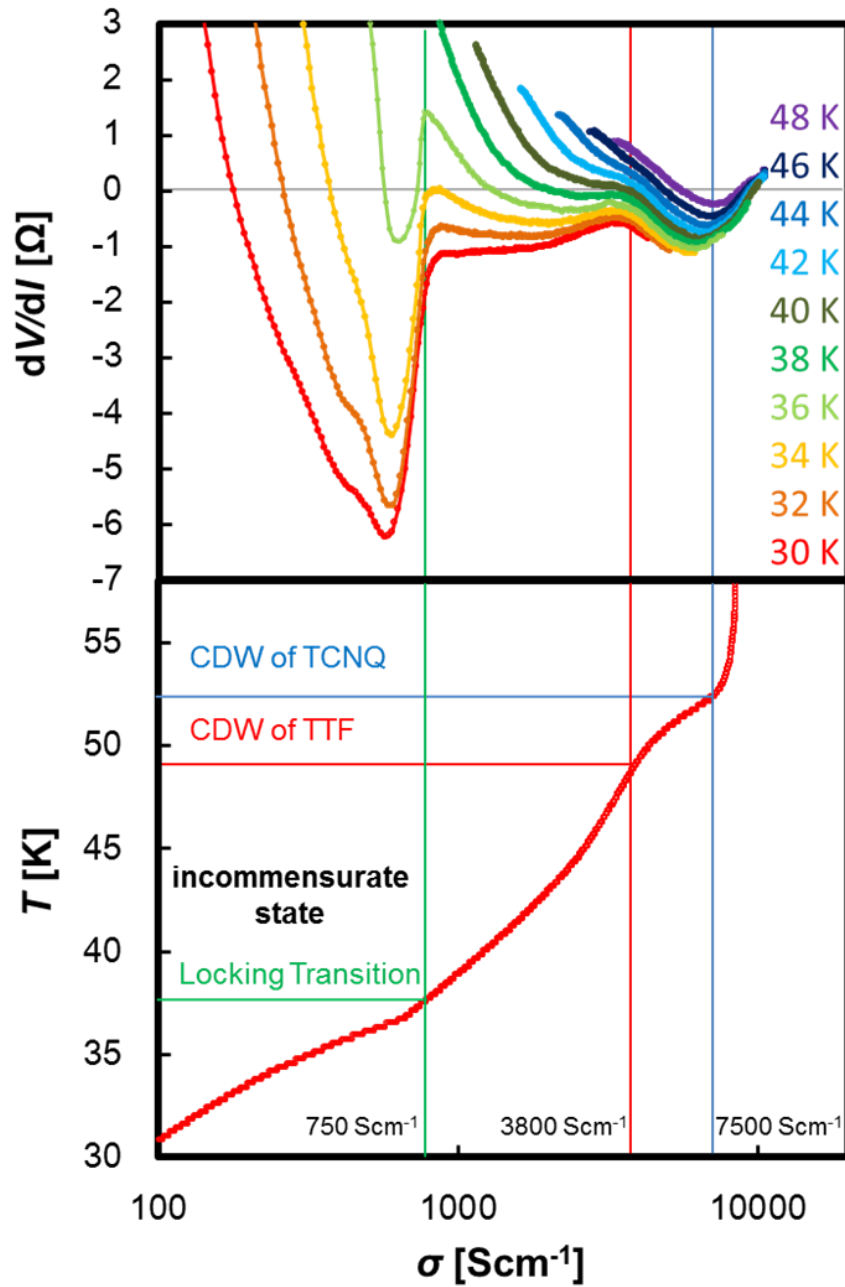


Figure 2-12. Comparison of the plot of differential resistance and conductivity and the plot of temperature dependence of conductivity in the V-I measurement of TTF-TCNQ.

The effect of the applied current density is also observed in the temperature dependence of the conductivity of **TTF-TCNQ**, as shown in Figure 2-13. The larger the applied current density, the larger the conductivity. However, the sample conductivity is not simply proportional to the applied current density at these temperatures. The conductivities at 0.1 and 1 mA are nearly the same above 40 K, but they bifurcate at 38 K, which is the locking temperature of the CDWs along the **TTF** and **TCNQ** chains. The conductivities at 1 and 5 mA bifurcate at 53K, which corresponds to the formation of CDW along the **TCNQ** chain. In cases where the applied currents are larger than 5 mA, the conductivity increases across the whole temperature range up to 60 K in the metallic phase. These results suggest that the number of charge transport carriers carried with the transport mechanism for each temperature region is limited, and that the excess number of charge carrier causes the excitation of the upper conducting mechanism in a stepwise fashion.

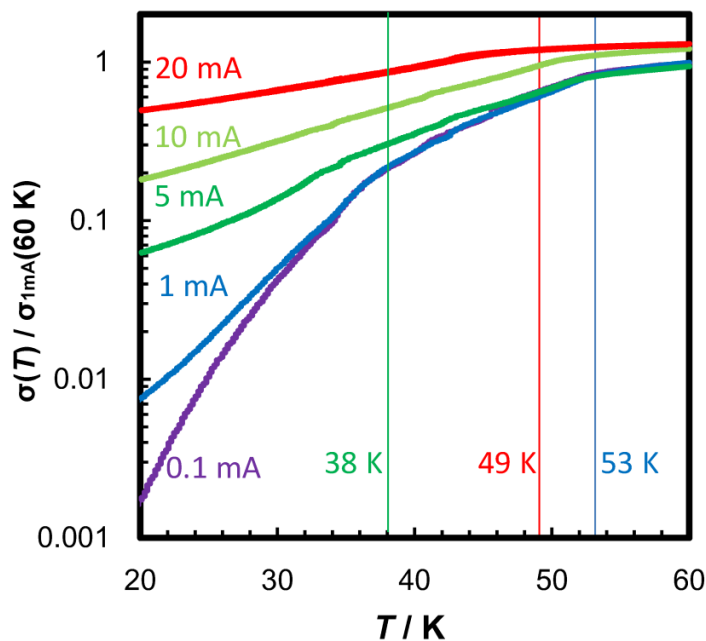


Figure 2-13. Temperature dependence of the conductivity at different current values.

2-6. Transport measurement methods

Whereas NDR behavior is classified as N- or S-type, as described in the Introduction, the NDR observed in bulk crystals of organic conductors is always the latter. In the case of S-type NDR, with an increase in the current, the sample resistance decreases greatly at a rate faster than the increase in the current. In most cases reported so far, the I - V characteristics are measured in a situation in which a load resistor is inserted in series to limit the largest current, and the voltage drop at the load resistor is subtracted to plot the I - V for the sample. However, in this case, neither the voltage nor the current applied to the sample can be controlled precisely. Since up to three current values can be taken with the same voltage in the S-type NDR (as shown in Figure 2-9), voltage oscillation between the states may take place in some cases. In fact, some investigations were carried out to stabilize the oscillation of an S-type NDR system by controlling the time constant, which depends on the additional resistors and capacitors.^{22,56,57} On the other hand, when a voltage is applied to a sample showing S-type NDR without a load resistor, the current monotonically increases as the voltage increases, and a rapid increase of the current should only be observed⁵⁸⁻⁶⁰ without a negative slope. This should be the reason why NDR has not been observed in **TTF-TCNQ** so far. Since the sample resistance in the S-type NDR system decreases monotonously with increasing current density, as shown in Figure 2-9, the current-applied/voltage measurement method (V - I) is preferable for investigating the transport behavior in this system. In addition, when the sample has a semiconducting nature, the interface with the metal electrode may have nonlinear conductivity due to the formation of a Schottky barrier in some cases. For these reasons, a DC four-terminal method was applied, in which four electrodes were attached to the sample and the voltage on the sample was measured with the different pairs of electrodes from the current

application. Actually, reproducible results were stably and repeatedly obtained with respect to the behavior of NDR when the current sweep was performed by the direct current four-terminal method.

On the other hand, higher-order I - V ($I \propto V^n$, $n \geq 2$) and NDR behavior are often considered to be the effects of the Joule heat, because the resistance of the sample decreases through thermal excitation. Generally, conductors with an insulating ground state exhibit thermally activated conductivity, and thus it is possible to show nonlinear I - V characteristics through the Joule heat. However, in this study, when the thermal effect of the Joule heat from the thermal flow through four gold wires ($25 \mu\text{m}\phi$ and 3 mm long at maximum) with the thermal conductivity of gold ($420 \text{ W}\cdot\text{m}^{-1}\cdot\text{K}^{-1}$) was taken into account, the temperature difference of the sample from the system temperature was estimated to be ca. 2 K at maximum with a maximum consumed power of $600 \mu\text{W}$, as shown in Figure 2-11(d). In this case, the conductivity of the sample at 30K corresponds to that at 49 K under loading current, and this value cannot be explained from the thermal effect of the Joule heat (2K in maximum). Therefore, the effect of the Joule heat would not be the main reason for the NDR of the temperature dependence of the E - J characteristics in this study.

In addition, to minimize the effect of Joule heat further, measurements were also carried out instantaneously by applying pulse current in addition to the usual continuous current sweep method. The fact that the V - I characteristics obtained by the continuous sweep method and the pulse method well agreed with each other also suggests the small effect of the Joule heat. Although a hysteresis loop, which is observed in the increasing and decreasing current processes in a part of the conductivity range below 44 K in continuous sweep measurements, was not observed in the pulse measurements, this would

be due to structural change in the incommensurate phase having a relatively slow time response.

2-7. Origin of NDR and temperature dependence in TTF-TCNQ

In general, S-type NDR is caused by some excitation mechanism from an insulating ground state to a higher-conductivity excited state by current application. At this excitation, when the rate of increase in conductivity is greater than the rate of change of the current, the voltage drop has a negative slope relative to the current and can be observed as NDR. Regarding the organic conductors exhibiting NDR so far reported, they often have CDW states, such as charge disproportionation and charge ordering, and the melting of the high-resistive CDW state to a higher-conductivity state is caused by the applied current, although the mechanisms underlying this phenomenon have not been clarified in some cases.

In the case of **TTF-TCNQ**, while it shows metallic conducting behavior due to the uniform π -stacking structure in the high-temperature phase, it turned out to be insulating in the low-temperature phase below 53 K by seven orders of magnitude, down to 4.2 K, accompanied by dimerization in the π -stacking column based on the Peierls transition. Therefore, inversely, the melting of the dimerized structure in the low-temperature phase to the uniform structure by the application of current could be a cause of NDR, although there is no direct evidence of structural change during the appearance of NDR in this stage. However, although NDR has not been reported in **TTF-TCNQ**, higher-order I - V characteristics ($I \propto V^n$, $n \geq 2$) have been reported in detail and the underlying mechanism has been discussed⁵⁸⁻⁶⁰: the threshold voltage dependence on the three Peierls insulator phases is explained in terms of the depinning of the CDW. Although the expression is different due to the difference in the measurement method (I - V and V - I), the origin of the reported higher-order I - V and that of the NDR in this study should be the same. Therefore, we will not discuss this point further.

Our new finding, that the conducting behavior depends on the conductivity of the system itself, as shown in Figure 2-12, is quite interesting. It was found that the inflection points in the E - J curves for different temperatures were well sorted in terms of the conductivity of the sample. Usually, the conductivity of the material is considered to be the result of the electronic structure of the sample and the function of the environmental variables, such as temperature and pressure. Therefore, the relationship seems opposite in the current case. In the case of **TTF-TCNQ**, each phase under 53K shows S-type NDR. As described above, S-type NDR is explained as a phenomenon in which the sample conductivity increases as the current increases. Since the conductivity σ is expressed as the product of the carrier density n , elemental charge e , and mobility μ , and since e and μ are supposed to be constant in the same crystal phase, the conductivity of the sample will depend mainly on n . In the case of an NDR system, n is not only excited thermally, but also induced by externally applied current. However, the carrier density n should have some upper limit for each carrier transport mechanism. In **TTF-TCNQ**, although the band gap is formed and insulated through the Peierls transition below 53 K, the insulating electronic structure is caused by the correlations among the system's electrons themselves. Electric current is nothing but moving electrons (or holes) in the sample itself. If a certain value of current was made to always flow in the sample and the carrier density n exceeds that of the n naturally generated by thermal excitation above the transition temperature for the higher conductive phase, the electronic state can be regarded as the same as that in the higher conductive phase, and finally the phase transition takes place. Therefore, the NDR and phase transition through V - I measurements could be attributed to the function of carrier density in the CDW states of **TTF-TCNQ** below the Peierls transition temperature, as drawn in Figure 2-14. This explanation will be applicable to other NDR

and higher-order I - V systems having similar strong-electron-correlation mechanisms.

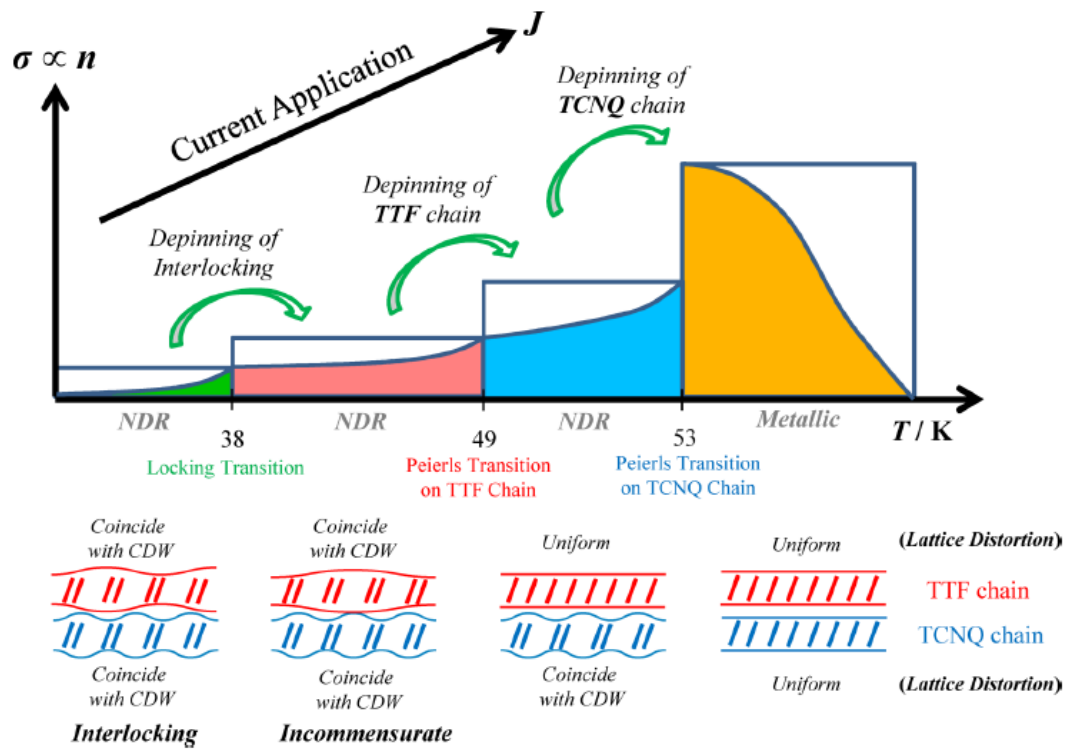


Figure 2-14. Mechanism of phase transition due to current application of TTF-TCNQ.

2-8. Conclusion

Negative differential resistance (NDR) was found and added as a new feature of **TTF-TCNQ**, the most famous and well investigated organic conductor. NDR was observed in the whole measured temperature range below 53 K, which corresponds to the Peierls transition temperature, whereas the structures in the E - J curves including NDR depend on the three phases below 53, 49, and 38 K. Although the origin of NDR would be the same as that of the reported higher-order I - V characteristics ($I \propto V^n, n \geq 2$), it was revealed that both NDR in the V - I characteristics measurements and the phase transitions in the temperature dependence measurements could be explained as functions of the charge carrier density in the sample, because the three inflection points observed in both plots had the same conductivity. This feature originated from the characteristic electronic structure of **TTF-TCNQ**. Since the Peierls phase transition depends mainly on the strong correlations among electrons in the quasi-one-dimensional electronic structure, the electronic state would be quite sensitive to the charge carrier density regardless of the origin of the carrier, i.e., whether it is thermally excited or externally induced by the current application.

Chapter 3

Acceleration of single-crystal to single-crystal phase transition by current

3-1. Introduction

In the previous chapter, it was revealed that the phase transition of **TTF-TCNQ** crystal is caused by applied current. In this system, the increase in charge carriers due to the applied current caused phase transitions as well as a change of carrier density based on the thermal excitation. It is quite interesting to determine whether this mechanism could be used to control the phase transitions in various materials. In this chapter, **TBC3·Br·TCE₂** was used to answer this question. **TBC3·Br·TCE₂** is an ion-radical salt of **TBC3**, which is a **TTF**-based cross-cyclophane-type donor molecule.^{37,61} In **TBC3**, two **TTF** skeletons are connected orthogonally by four alkyl chains. In **TBC3·Br·TCE₂**, single-crystal to single-crystal structural phase transition has been reported around 170 K due to the high degree of molecular freedom of **TBC3**. Moreover, non-linear conductivity including the negative differential resistance (NDR) was observed in the high temperature phase of this salt with respect to its disproportionated charge distribution.⁵⁰

In this study, the effects of current application on this system were investigated by means of DC conductivity, AC impedance, magnetic susceptibility, and theoretical calculation. In addition, before starting the above investigations, detailed X-ray structure analyses were carried out for both its phases, because the previous research was carried out more than 20 years ago and only the preliminary results were reported due to the insufficient quality of the data. Due to the subsequent improvements in X-ray structure analysis techniques, it was possible to obtain structural data of sufficient quality and to use this

data to discuss changes of the physical properties through the phase transition, including theoretical calculations. AC impedance measurements revealed the change in the dipole moment near the phase transition temperature due to the change in the orientation of solvent molecules incorporated in the crystal. As for the phase transition process, the activation energy could be evaluated by determining the phase transition rate from the high temperature phase to the low temperature phase at each temperature. Further, it was discovered that the phase transition rate depends on the applied current (acceleration effect of the phase transition rate by the applied current), and this effect was elucidated with a phase diagram.

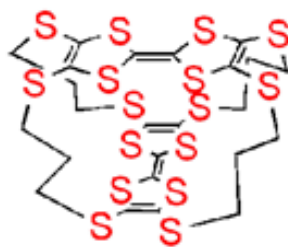


Figure 3-1. Molecular structure of **TBC3**.

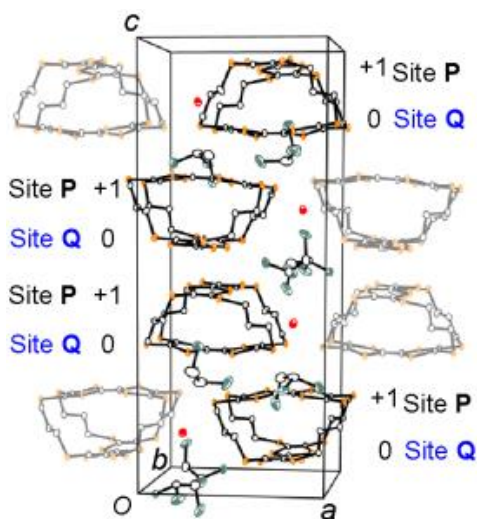


Figure 3-2. Crystal structure of **TBC3·Br·TCE₂**.

3-2. Cyclophane donor molecule **TBC3** and its ion-radical salt

Most of the molecular materials having high conductivity usually have stacking structures consisting of π -conjugated system. However, in 1992, a semiconductor salt in which neighboring **TTF**s overlapped in a cross-stacking manner was reported,⁶² and this report engendered interest in determining how the stacking arrangement of **TTF**s affects the physical properties. In order to regulate such intermolecular interactions of **TTF**s in the crystal, various molecules that connect two **TTF** skeletons, which can be regarded as the smallest unit of intermolecular interactions, have been synthesized. One of these was the cyclophane-type donor molecule **TBC3**,^{37, 61} which has a structure in which two **TTF**s are connected orthogonally, and which was reported in 1995. The cyclophane donor **TBC3** is linked by four trimethylene-dithio chains so that two **TTF** units are located orthogonal to each other. As a result, **TBC3** has a large degree of freedom in the relative orientation of **TTF**s and in the conformations of the alkyl chains. Electro-crystallization of this donor molecule in the presence of tetrabutylammonium bromide (**TBA**·**Br**) in trichloroethane (1,1,2-TCE) as a solvent affords the ion-radical salt **TBC3**·**Br**·**TCE**₂,³⁶ where the 1,1,2-TCE is incorporated as the crystal solvent. In the crystal, the donor molecules are stacked by rotating 90 degrees so that the **TTF** skeletons face each other in parallel within the stacking neighboring molecules and form a spiral-stacking structure. The conductivity of the **TBC3**·**Br**·**TCE**₂ crystal along *a(b)*- and *-c* were reported as $\sigma_{RT} = 1.0 \times 10^{-2}$ and $5.5 \times 10^{-2} \text{ S}\cdot\text{cm}^{-1}$, respectively. The Curie constant is 0.375 for one mole of **TBC3**·**Br**·**TCE**₂ unit, suggesting one cation radical is carried per one **TBC3** molecule.

Due to the high degree of freedom of the donor molecule, one of the two **TTF** skeletons of the donor molecule, which are both planar near room temperature, bends significantly below 170 K and undergoes a structural phase transition from a *Tetragonal*

to a *Monoclinic* crystal system.^{36,50} Physical properties also change upon this phase transition: the resistance along the *c*-axis decreases to *ca.* 1/10 while the magnetic susceptibility becomes 1/2, from the high temperature phase (HTP) to the low temperature phase (LTP).

In 2005, it was discovered that the conductivity of the **TBC3·Br·TCE₂** crystal increased drastically by application of a large current, and the mechanism of this nonlinear response in the conductivity was studied by analyzing the X-ray crystal structure of the salt during the current application.⁵⁰ Figure 3-3(a) shows the *I-V* characteristics of the ion-radical salt at 170 K in the *c*-axis direction. In order to measure the resistance of the sample in a wide dynamic range, the load resistor R_L (1 M Ω) was inserted in the circuit in series. As the voltage was increased, the current increased sharply at 330-340 V, after which the plot approached a linear *I-V* dependent region where R_L was dominant. In addition, the sample showed hysteretic behavior in both the voltage-increasing process and voltage-decreasing process. The low resistance state was maintained until the voltage dropped below 340 V and returned to the initial resistance value at about 180 V. When converting *I-V* dependence to sample conductivity (σ) vs. current density (J), by subtracting the contribution of R_L , σ increases monotonically in the range of 10^4 as J increases (Fig. 3-3b). Therefore, the current-induced low resistance state of **TBC3·Br·TCE₂** was investigated by X-ray crystal structure analysis. By applying a constant high voltage (480 V) to a circuit with a load resistor (1 M Ω) connected in series, the resulting current density (0.57 A·cm⁻²), which was sufficient to cause resistance conversion, was kept constant throughout the measurement. In the HTP crystal of **TBC3·Br·TCE₂**, two TTF units in the donor molecule in the crystal are disproportionate to the cationic state and the neutral state, respectively, based on the bond lengths. These

bond lengths change in the current-induced low-resistance state: the difference in the bond lengths between the two sides of TTFs became negligible in the current-induced low-resistance state. Thus, the nonlinear conductivity of this crystal could be interpreted as the relaxation of the disproportionated structure. When the structures of the two facing donor units are equivalent, the charge will be delocalized to the two facing donor units. Due to this structural change, the activation energy of electron transfer between the neighboring molecules in the current-applied state becomes much smaller than that in the original state. Due to the combination of structural equalization and charge delocalization, the low resistance state is maintained even after the applied current decreases and causes the hysteretic behavior.

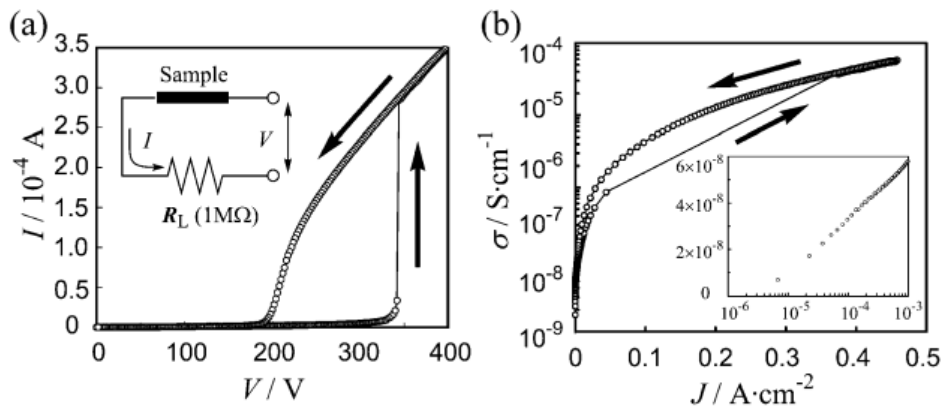


Figure 3-3. (a) I - V characteristics of $\text{TBC3}\cdot\text{Br}\cdot\text{TCE}_2$ along the c -axis at 170 K. (b) The I - V characteristic of the entire circuit was transformed into the relation between the electric field E and the current density J , by deducting the contribution of the load resistor, and then converted to σ - J dependence.⁵⁰

3-3. Crystal preparation and fabrication of measurement devices

The donor molecule **TBC3** and TBA·Br as an electrolyte were placed on both sides of an electrolysis cell, and then 1,1,2-TCE was added as the solvent. Prior to use in the electrolysis, the solvent 1,1,2-TCE was passed through an alumina column and filtered through pleated filter paper. Then two platinum electrodes were inserted in the electrolyte solution and electro-crystallization was performed under the galvanostatic condition. The current value was changed according to the growth of the crystal (from 0.1 μA to 2.0 μA). Interestingly, the crystal morphology differed depending on the applied current value. At a low current value, the crystal grew in a thin planar shape (along the *ab*-plane), whereas it grew in a needle shape (along the *c*-axis) at a high current value (Fig. 3-5). This may have been due to the difference in the conductivity and the fact that the easier growth direction of the crystal was dependent on the current densities. When the color of the solution became light (indicating the consumption of the donor molecule) and the crystals grew sufficiently, the current application was stopped and the electrode with the crystals was removed from the solution. The crystals were washed with a small amount of 1,1,2-TCE and then removed from the electrodes. Samples for conductivity measurement were prepared by attaching gold wires with gold paste to both ends along the measurement axis as shown in Figure 3-6 (*c*-axis) and Figure 3-7 (a) (*a*, *b*-axis). Figure 3-7 (b) shows a sample for impedance measurement, which enables measurement in the *c*-axis by attaching gold wires with gold paste to the *ab* plane obtained by cutting the crystals. Figure 3-8 shows a sample for X-ray structural analysis, in which crystals are fixed on the glass capillary using an epoxy resin.

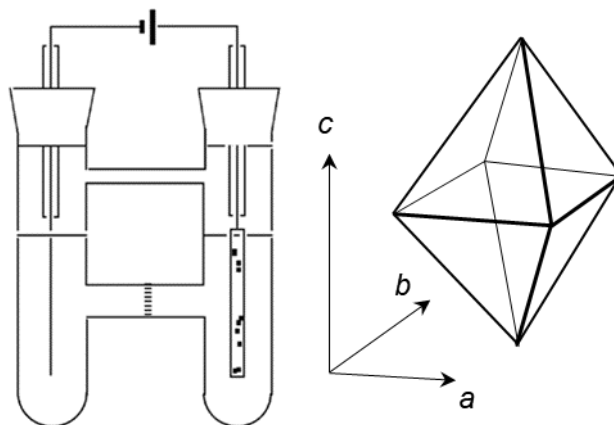


Figure 3-4. Schematic diagram of the electrolysis cell, and outline of crystals.

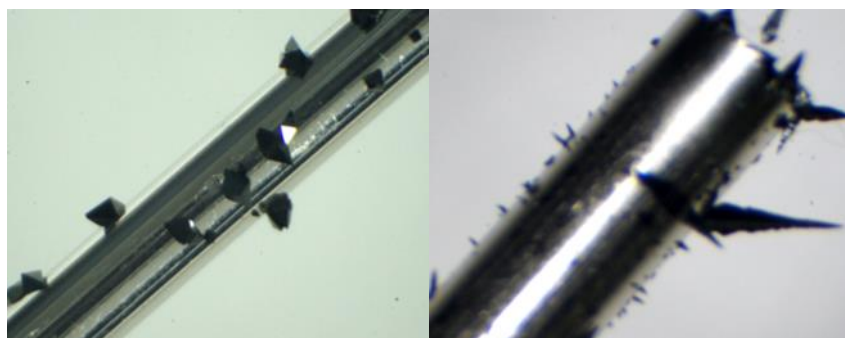


Figure 3-5. $\text{TBC3}\cdot\text{Br}\cdot\text{TCE}_2$ crystals grown on a platinum electrode (left figure: $0.2\ \mu\text{A}$; right figure: $0.5\text{-}2.0\ \mu\text{A}$).

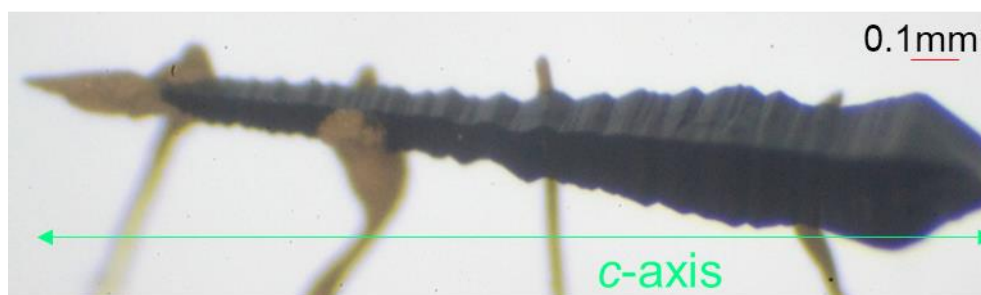


Figure 3-6. Sample for measuring the conductivity of $\text{TBC3}\cdot\text{Br}\cdot\text{TCE}_2$ in the c -axis direction (the sample dimensions are $2.0\ \text{mm} \times 0.3\ \text{mm} \times 0.3\ \text{mm}$).

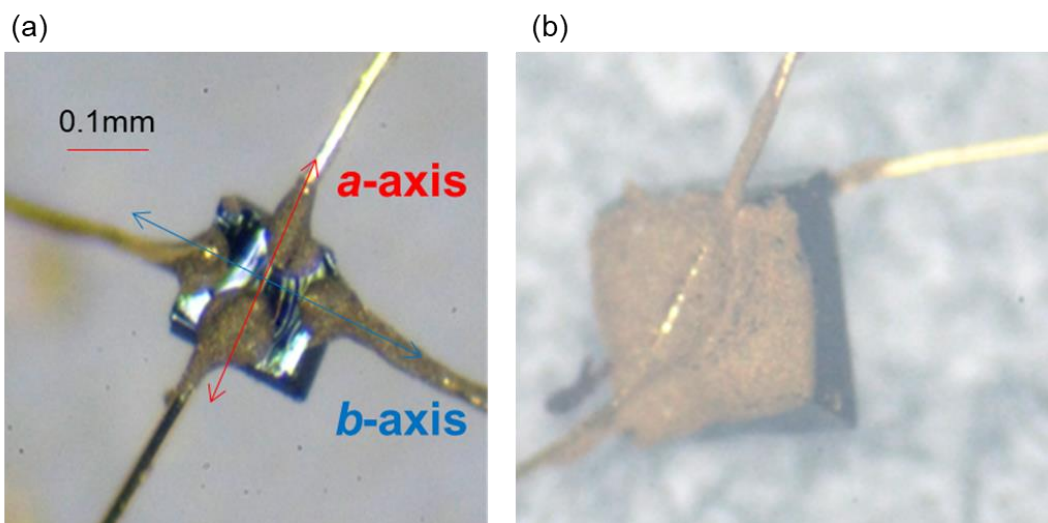


Figure 3-7. (a) Sample for conductivity measurement of $\text{TBC3}\cdot\text{Br}\cdot\text{TCE}_2$ along the a - and b -axis (the sample dimensions are 0.18 mm x 0.16 mm x 0.1 mm).
 (b) Sample for impedance measurement of $\text{TBC3}\cdot\text{Br}\cdot\text{TCE}_2$ along the c -axis (the sample dimensions are 0.2 mm x 0.2 mm x 0.1 mm).

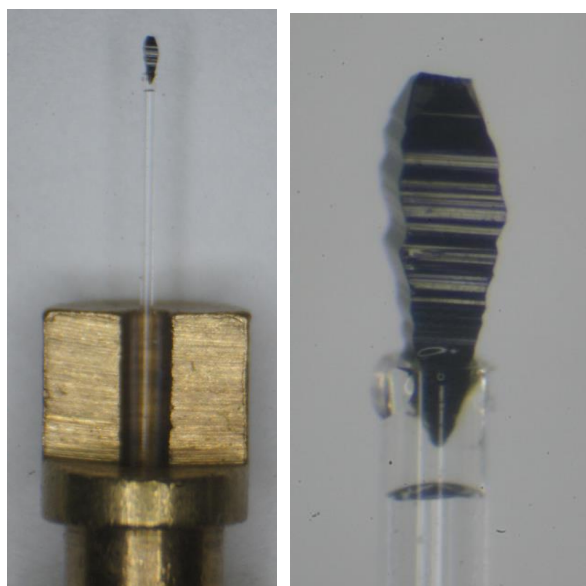


Figure 3-8. Sample for X-ray structural analysis of $\text{TBC3}\cdot\text{Br}\cdot\text{TCE}_2$ (the sample dimensions are 0.3 mm x 0.3 mm x 1.0 mm).

3-4. Equipment for physical property measurements

Temperature dependence of resistivity and voltage–current characteristics of $\text{TBC3}\cdot\text{Br}\cdot(\text{TCE})_2$

On the crystal of the ion-radical salt $\text{TBC3}\cdot\text{Br}\cdot(\text{TCE})_2$, gold wires of 25 μm diameter were attached using gold paste. Then the sample was mounted on the electrode substrate manufactured on a printed circuit board. Then, the electrode substrate was fixed on the sample puck and introduced into the Quantum Design PPMS-P650BW cryostat, and the temperature of the sample was regulated from room temperature to 2 K.

The resistance and voltage–current characteristics of the ion-radical salt were measured by using an Advantest R6245 voltage current source monitor under measurement conditions controlled by computer programs designed in-house.

In the previous report, the conductivity of the HTP crystal along $a(b)$ - and $-c$ were reported as $\sigma_{\text{RT}} = 1.0 \times 10^{-2}$ and $5.5 \times 10^{-2} \text{ S}\cdot\text{cm}^{-1}$, respectively.⁵⁰

X-Ray crystal structure analysis

Single-crystal X-ray diffraction data were collected on a Bruker APEX CCD X-ray diffractometer (Mo $k\alpha$ radiation: 0.71073 Å, 50 KV/35 mA) at 110 K and 150 K. The frames were integrated using the Bruker SAINT software package and a narrow-frame integration algorithm. Absorption corrections were applied to the raw intensity data using the SADABS program. The Bruker SHELXTL software package was used for phase determination and structure refinement.

AC impedance measurement

AC impedance was measured from 1Hz to 100kHz using ZM2372 impedance analyzer (NF Circuit co.) on the **TBC3·Br·(TCE)₂** crystal which is the same to the sample used in the DC conductivity measurements. Temperature dependence measurements were carried out using a cryostat with a vacuum-shielded probe inserted in a liquid nitrogen dewar.

Magnetic Susceptibility

Magnetic susceptibility of **TBC3·Br·(TCE)₂** crystal was measured with a MPMS-5XL SQUID magnetometer (Quantum Design) between 2K and 300 K with the 0.5 T of external magnetic field. The scan speed, which significantly affects the phase transition behavior, was controlled between 0.1K/min to 10K/min.

Electron spin resonance

Electron spin resonance (ESR) of the **TBC3·Br·(TCE)₂** crystal was measured in the X-band (9.4 GHz) using JES-FA200 spectrometer. The crystal was attached on the cross section of the tip of a 3 mm ϕ Teflon rod using Apiezon grease and inserted into a quartz glass sample tube. Angular dependent measurement of the crystal was carried out while rotating every 10 degrees using sample rotator.

3-5. Structural features of TBC3 and TBC3·Br·TCE₂

X-ray crystal structure analyses were performed on the crystal of the **TBC3** donor molecule and its ion-radical salt **TBC3·Br·TCE₂**. The structure of the high temperature phase (HTP) crystal was measured at 110 K, which was supercooled from room temperature by rapid cooling to quench the phase transition, and the low temperature phase (LTP) crystal was measured at 150 K after being cooled for a sufficiently long period of time below the phase transition temperature.

Table 3-1. Crystal data and structure refinement for **TBC3·Br·TCE₂** and the **TBC3** donor.

	HTP	LTP	Donor
Formula	C ₂₈ H ₃₀ BrCl ₆ S ₁₆	C ₂₈ H ₃₀ BrCl ₆ S ₁₆	C ₂₄ H ₂₂ S ₁₆
FW	1172.09	1172.09	813.29
Temp.(K)	110(2)	150(2)	140(2)
crystal system	Tetragonal	Monoclinic	Tetragonal
Space group	<i>P</i> 4 ₁	<i>P</i> 2 ₁	<i>P</i> 4 ₁
<i>a</i> / Å	12.3601(4)	12.2881(15)	15.1853(10)
<i>b</i> / Å	12.3601(4)	29.416(4)	15.1853(10)
<i>c</i> / Å	29.6990(14)	12.3311(14)	30.038(3)
<i>α</i> / °	90	90	90
<i>β</i> / °	90	90.200(7)	90
<i>γ</i> / °	90	90	90
<i>V</i> / Å ³	12.3601(4)	29.416(4)	6926.6(11)
<i>Z</i>	4	4	8
<i>R</i> _{all}	0.0583	0.0625	0.0436
<i>R</i> _{<i>I</i> > 2σ}	0.0555	0.0568	0.0414

Structure of the neutral crystal of TBC3 molecule: It belongs to the space group of *Tetragonal, P4₁*, and two TBC3 molecules consist the asymmetric unit. The two TBC3 molecules within the asymmetric unit have different structures, one resembling the structure of HTP in an ion-radical salt and the other resembling the structure of LTP, as described in a later section. In the crystal, the π -conjugated system of the TTF skeleton and the alkyl chain of the adjacent molecule face each other, so that the π -conjugated system is arranged orthogonally between the adjacent molecules and the asymmetric unit forms a screw axis by rotating 90 degree along the *c*-axis.

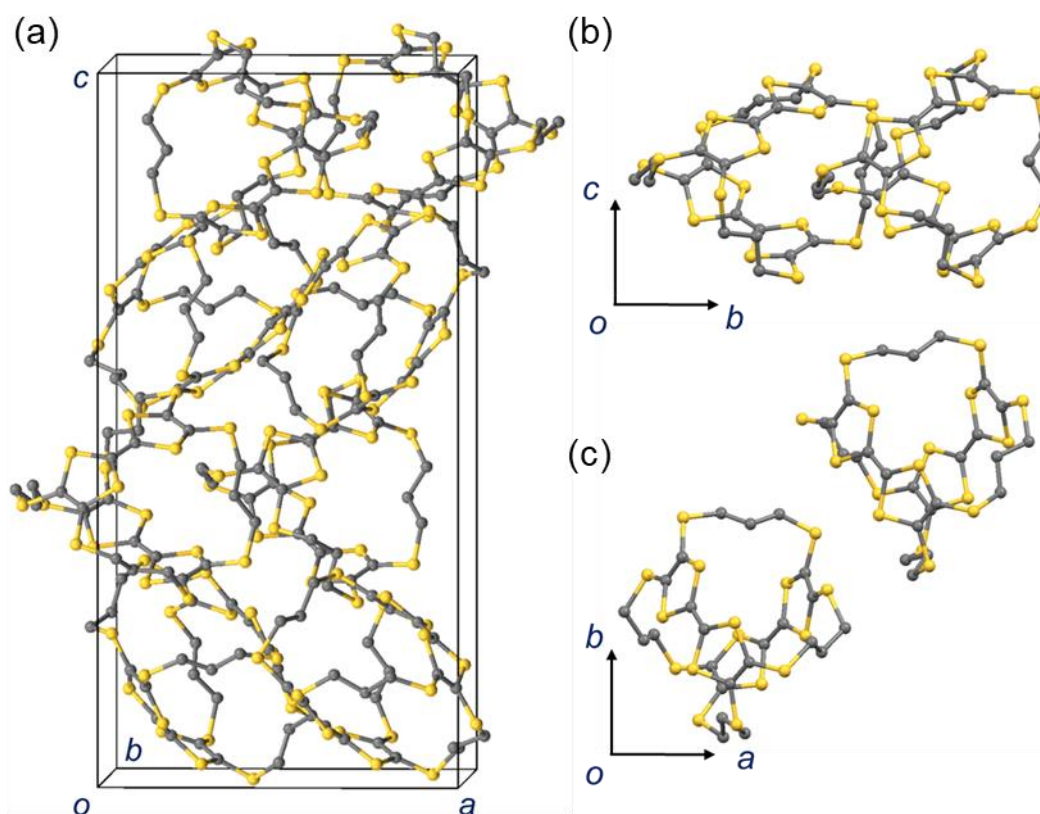


Figure 3-9. Crystal structure of the neutral TBC3 donor crystal. (a) Crystal packing in a unit cell. (b) Molecular arrangement in the *bc* plane. (c) Molecular arrangement in the *ab* plane.

Structure of the high temperature phase of TBC3·Br·TCE₂: The high temperature phase belongs to the space group of *Tetragonal, P4₁*; one donor molecule is an asymmetric unit, and it is stacked by rotating 90 degrees in the direction of overlapping π -conjugated systems (screw axis). At this time, the two TTF donor skeletons in the molecule are not equivalent: judging from the bond length, it is clear that one skeleton is close to the structure of the cation and the other is close to the structure of the neutral molecule as reported in the previous work.^{36, 50}

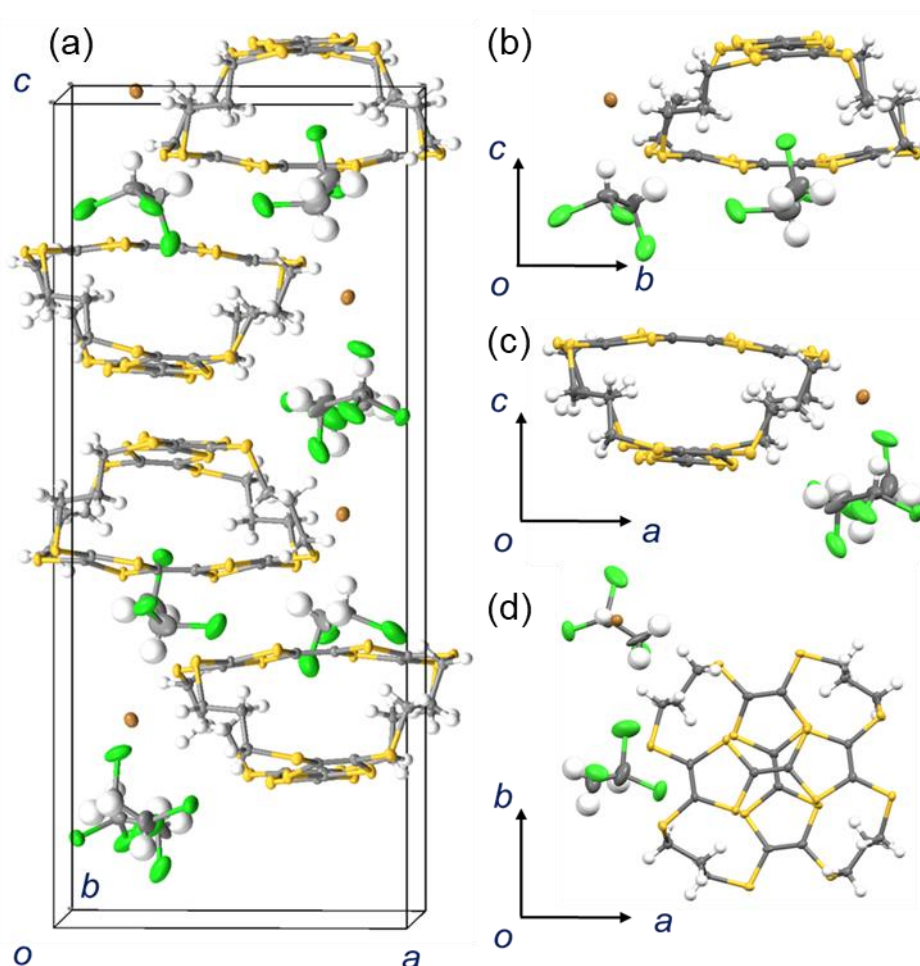


Figure 3-10. Crystal structure of TBC3·Br·TCE₂ in HTP. (a) Crystal packing in a unit cell. (b) View of the asymmetric unit from the *a*-axis. (c) View of the asymmetric unit from the *b*-axis. (d) View of the asymmetric unit from the *c*-axis.

Structure of the low temperature phase of TBC3·Br·TCE₂: The low temperature phase belongs to the space group of *Monoclinic, P2₁*, and the two donor molecules are asymmetric units. The *a*- and *b*-axis, which were equivalent in LTP, became unequivalent (since the way to assign the axes is different, they correspond to the *a*-axis and *c*-axis), and the donor skeleton is greatly bent on one side and closer to a flat surface on the other side. At this time, based on the bond length and the results of the theoretical calculation, the planar one is considered to be a cation radical, but since the planar sides are overlapped with each other in the layer stack, the formal charge of the donor skeleton in the stacking direction is 0⁺·10⁻·0⁺·10⁻. However, as will be described later, from the measurement results of magnetism and conductivity, it is considered that some charge transfer occurs between the layers. In addition, since the *a*- and *b*-axes were originally equivalent in HTP, there is a possibility that the bending direction may be either in LTP, and the components that actually bend in the direction of 90 degrees are mixed in a ratio of about 2:1 to form a Merohedral Twin treatment.

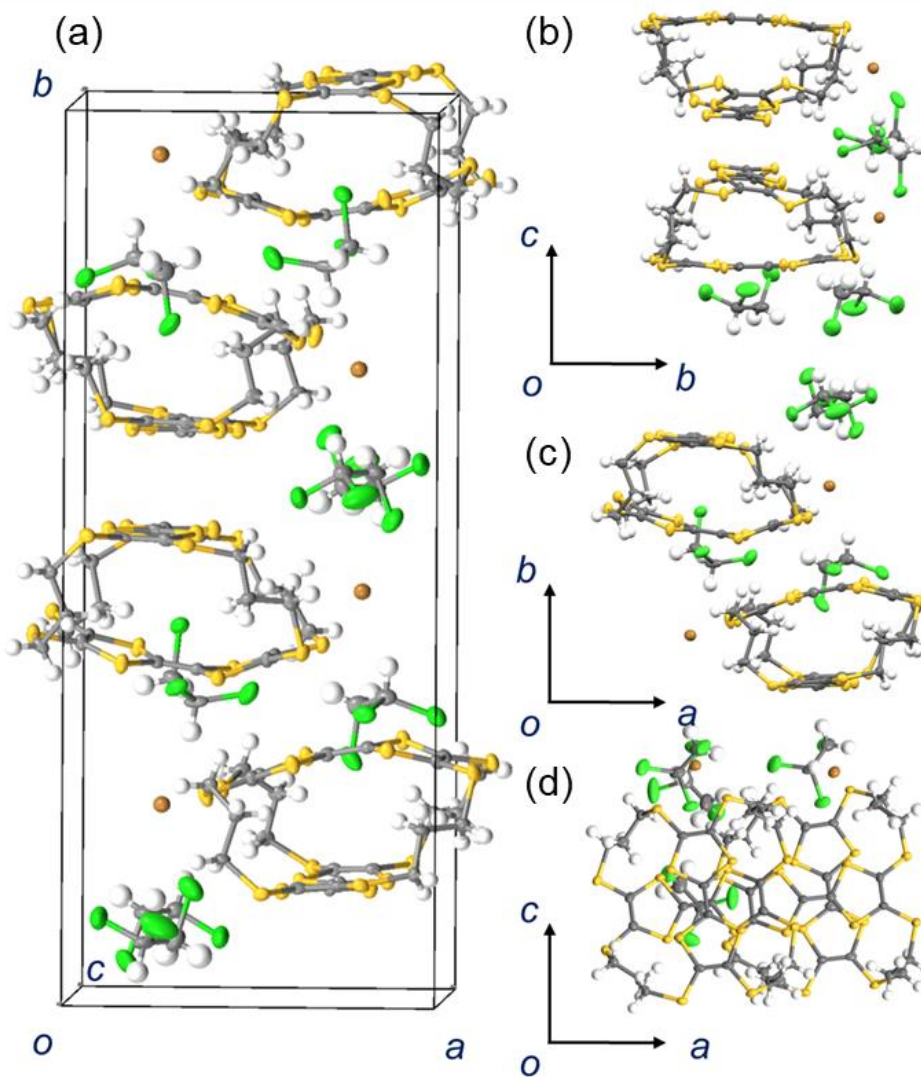


Figure 3-11. Crystal structure of $\text{TBC3}\cdot\text{Br}\cdot\text{TCE}_2$ in LTP. (a) Crystal packing in a unit cell. (b) View of the asymmetric unit from the *a*-axis. (c) View of the asymmetric unit from the *c*-axis. (d) View of the asymmetric unit from the *b*-axis.

Charge distributions in ion-radical crystals: Based on the obtained crystal structure, the bond lengths of the central C=C double bond and the C-S bonds around it were compared between the neutral **TBC3** crystal and the HTP and LTP of the ion-radical salt. In the donor molecule in the neutral donor crystal, the averaged bond lengths were 1.337 Å and 1.755 Å for the C=C bond and the C-S bond, respectively. On the other hand, in the HTP of the ion-radical salt, the bond lengths of the two TTF skeletons in one **TBC3** molecule were different; the C=C bonds were 1.383 Å and 1.357 Å, while the averages of the C-S bonds were 1.727 Å and 1.748 Å, respectively. Since the C=C bond should be extended and the C-S bond should be shrunk in cationic species in TTF analogues compared to those of the neutral species, the cationic charge is mainly localized on the TTF skeleton that has a larger change in the HTP crystal, which is called a charge disproportionation state. In LTP, the C=C bonds were 1.395 Å and 1.346 Å, and the averages of the C-S bonds were 1.722 Å and 1.794 Å, in one of the two **TBC3** molecules in the asymmetric unit, which was similar to the results for the HTP crystal. On the other hand, in another **TBC3** molecule in the LTP crystal, the C=C bonds were 1.369 Å and 1.357 Å, and the averages of the C-S bonds were 1.739 Å and 1.734 Å, suggesting that the cationic charge is distributed on both TTF skeletons in this **TBC3** molecule. However, because the standard deviation in the bond lengths is particularly large in the LTP, and comparisons of simple numerical values lack accuracy, these results should be interpreted with caution.

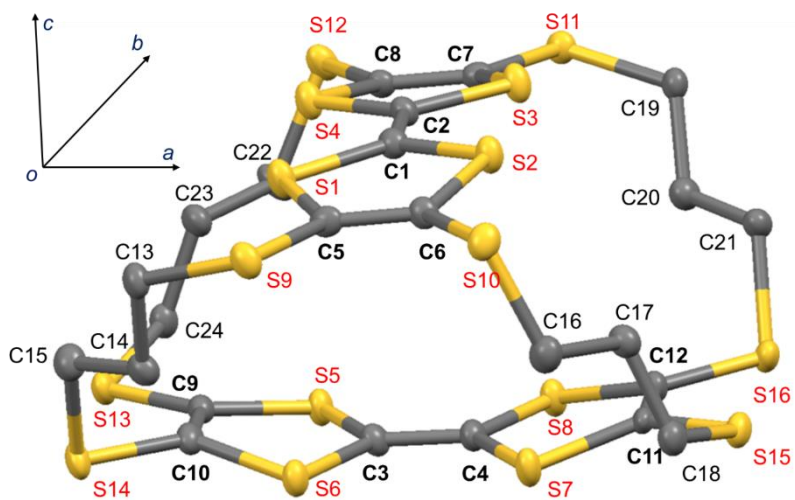


Figure 3-12. Molecular structure of the **TBC3** donor as the asymmetric unit in **TBC3·Br·TCE₂** crystal in HTP with the numbering scheme.

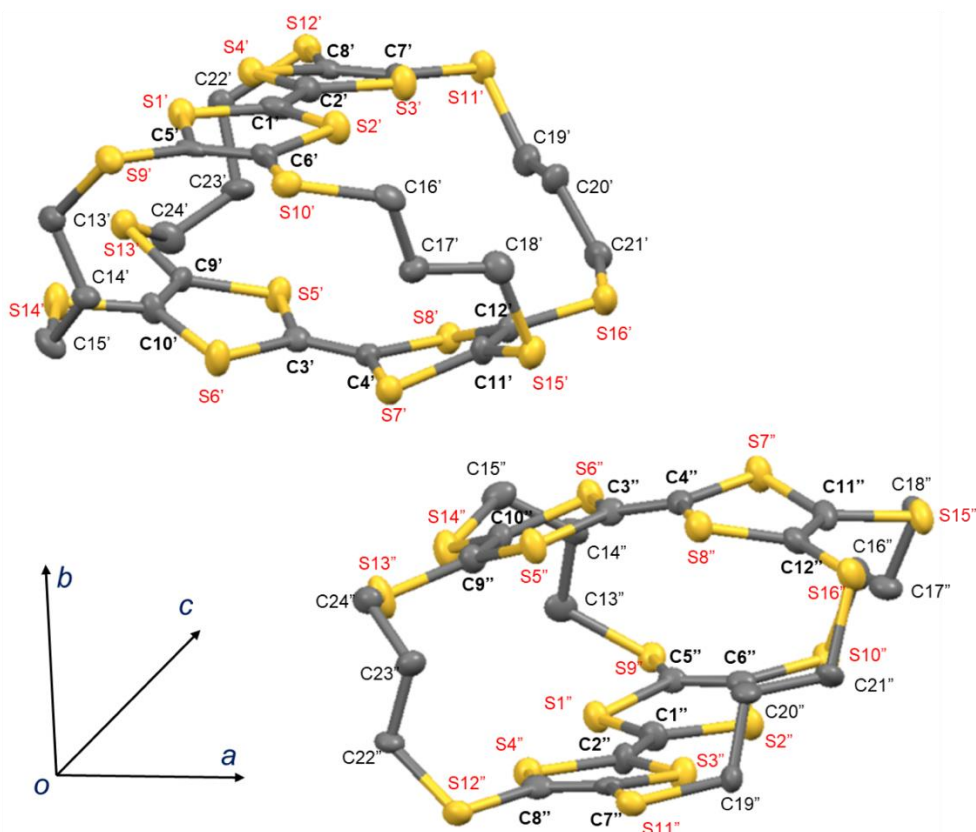


Figure 3-13. Molecular structures of **TBC3** donors as the asymmetric unit in the **TBC3·Br·TCE₂** crystal in LTP with the numbering scheme.

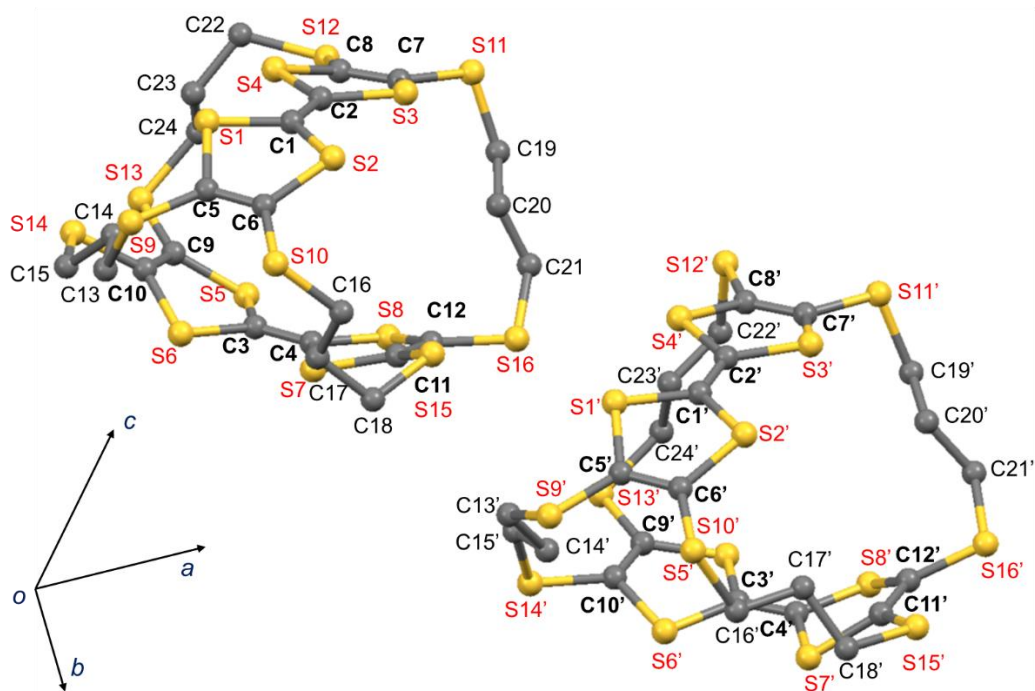


Figure 3-14. Molecular structures of **TBC3** molecules as the asymmetric unit in the neutral crystal with the numbering scheme.

Table 3-2. Bond lengths of donor molecules in the **TBC3·Br·TCE₂** crystal.

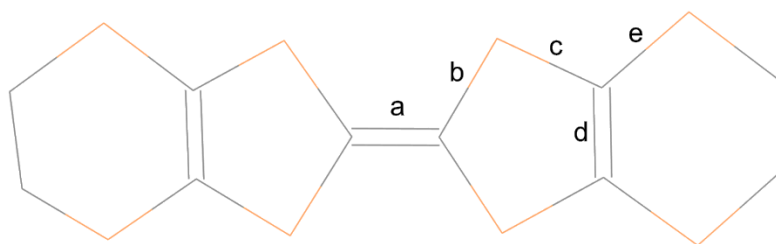
HTP		LTP			
Bond	Length / Å	Bond	Length / Å	Bond	Length / Å
C1 = C2	1.383(9)	C1' = C2'	1.395(17)	C1'' = C2''	1.369(15)
C1 - S1	1.729(6)	C1' - S1'	1.698(14)	C1'' - S1''	1.745(13)
C1 - S2	1.719(6)	C1' - S2'	1.734(14)	C1'' - S2''	1.738(12)
C2 - S3	1.732(7)	C2' - S3'	1.715(13)	C2'' - S3''	1.739(13)
C2 - S4	1.726(7)	C2' - S4'	1.741(12)	C2'' - S4''	1.734(12)
C3 = C4	1.357(9)	C3' = C4'	1.346(17)	C3'' = C4''	1.357(17)
C3 - S5	1.755(6)	C3' - S5'	1.757(12)	C3'' - S5''	1.742(12)
C3 - S6	1.743(6)	C3' - S6'	1.733(12)	C3'' - S6''	1.742(11)
C4 - S7	1.745(6)	C4' - S7'	1.756(11)	C4'' - S7''	1.737(11)
C4 - S8	1.748(6)	C4' - S8'	1.748(11)	C4'' - S8''	1.716(12)

Table 3-3. Bond lengths of donor molecules in the neutral crystal.

Bond	Length / Å	Bond	Length / Å
C1 = C2	1.330(7)	C'1 = C'2	1.337(7)
C1 - S1	1.754(5)	C'1 - S'1	1.758(5)
C1 - S2	1.761(5)	C'1 - S'2	1.758(5)
C2 - S3	1.755(5)	C'2 - S'3	1.754(5)
C2 - S4	1.757(5)	C'2 - S'4	1.757(5)
C3 = C4	1.346(7)	C'3 = C'4	1.336(7)
C3 - S5	1.754(5)	C'3 - S'5	1.741(5)
C3 - S6	1.760(5)	C'3 - S'6	1.767(5)
C4 - S7	1.747(6)	C'4 - S'7	1.752(5)
C4 - S8	1.749(5)	C'4 - S'8	1.755(5)

Therefore, the charge was evaluated with a set of several bond lengths utilizing the formula for the charge distribution of **BEDT-TTF** reported previously.⁶³ Four equations (3-2) can be established for each TTF skeleton, δ was calculated from the average value, and the charge density ρ was calculated using equation (3-2). Note that the twist angles at the ends of TTF units connected by alkyl chains in **TBC3** are different from that of **BEDT-TTF**, which is the target of this formula, and it would not be possible to obtain an accurate value for the **TBC3** system directly by using this formula. Therefore, the charge is normalized under the assumption that one donor molecule has one cationic charge. As a result, it was found that the charge densities differed between the two skeletons: the TTF skeleton containing C1-C2 in HTP (HT-TTF-a) had a charge density of $\rho = 0.73$, and the other TTF skeleton containing C3-C4 (HT-TTF-b) had a charge density of $\rho = 0.27$. The charge density of the TTF skeleton containing C1'-C2' in LTP (LT-TTF-a) was $\rho = 0.75$, and the charge density of the other TTF skeleton containing C3"-C4" (LT-TTF-b) was $\rho = 0.25$, similar to the results in HTP. However, in the other **TBC3** molecule, the

TTF skeleton containing C1"-C2" (LT-TTF-a') had an average charge density of $\rho = 0.46$, while the other TTF skeleton containing C3"-C4" (LT-TTF-b') had a charge distribution of $\rho = 0.54$. Thus the charge distribution differed between the two **TBC3** molecules in the LTP crystal.



$$\delta = (b+c) - (a+d) \quad (3-1)$$

$$\rho = 6.347 - 7.463 \delta \quad (3-2)$$

$$\delta = (b+c+e) - (a+d) \quad (3-3)$$

$$\rho = 2.584 - 0.1244 \delta \quad (3-4)$$

Figure 3-15. BEDT-TTF charge estimation formula and schematic diagram.⁶³

It is considered that the **TBC3** molecule is also affected by the twist angle with the alkyl chain, so the contribution of the bond length of “e” in Fig. 3-15 should also be discussed. Equations (3-3) and (3-4), which are extensions of equations (3-1) and (3-2), are obtained from the bond lengths of **BEDT-TTF** with different charges,⁶⁴⁻⁶⁶ and the charges in this system are estimated. As a result, the charges on TTF were estimated to be 0.83 (HT-TTF-a) and 0.17 (HT-TTF-b) in HTP and 0.98 (LT-TTF-a) and 0.02 (LT-TTF-b) in one molecule in LTP, while they were estimated to be 0.43 (LT-TTF-a') and 0.57 (LT-TTF-b') in the other molecule, which is consistent with the result by the previous formula without the contribution of the bond “e”.

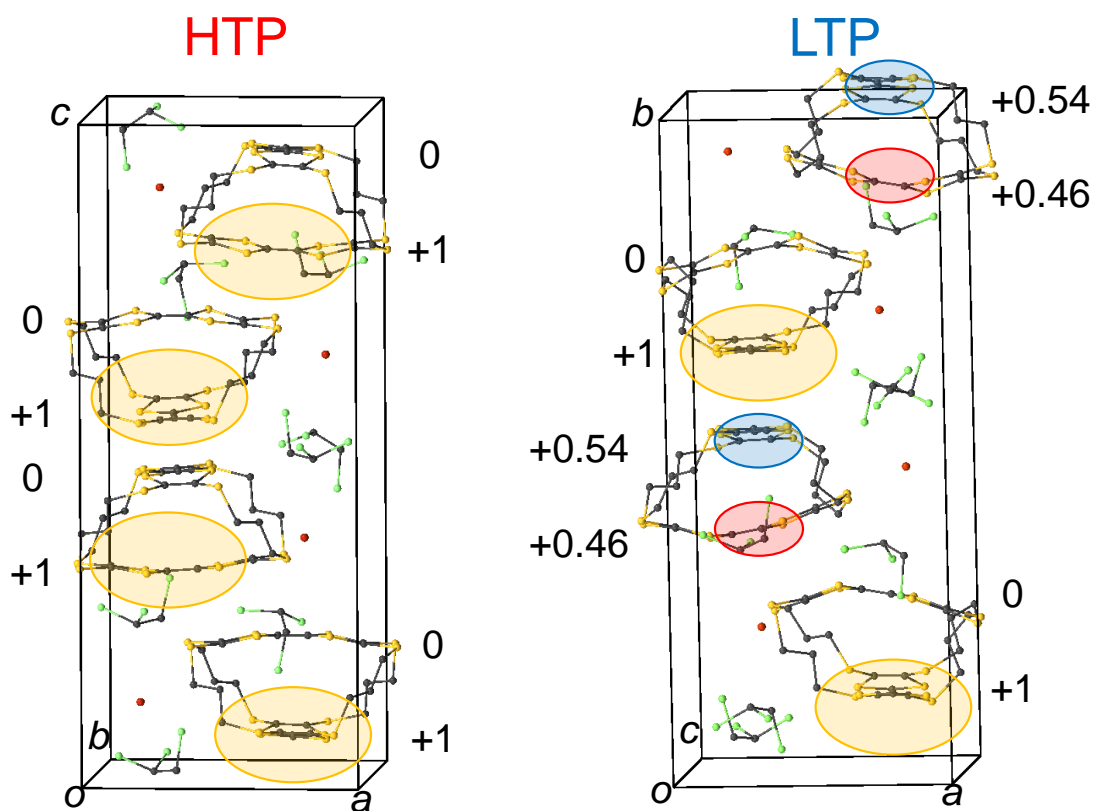


Figure 3-16. Charge distributions of $\text{TBC3} \cdot \text{Br} \cdot \text{TCE}_2$ in HTP (left) and LTP (right) evaluated from the bond lengths of the donor skeletons.

Molecular conformations in the crystal: The alkyl chain conformation of each donor molecule is summarized. In HTP, four alkyl chains showed similar conformations. In LTP, the alkyl chains connected to the bent side of the TTF skeleton showed different conformations, while the two types of donor molecules contained in one asymmetric unit showed similar conformations. In a neutral donor molecule, the two asymmetric donor molecules showed different conformations: one showed a conformation similar to the HTP of the ion-radical salt, whereas the other had a conformation similar to the LTP. From this result, it is considered that the conformational change of the alkyl chain due to the phase transition is a change between the stable conformations even in the neutral donor molecule.

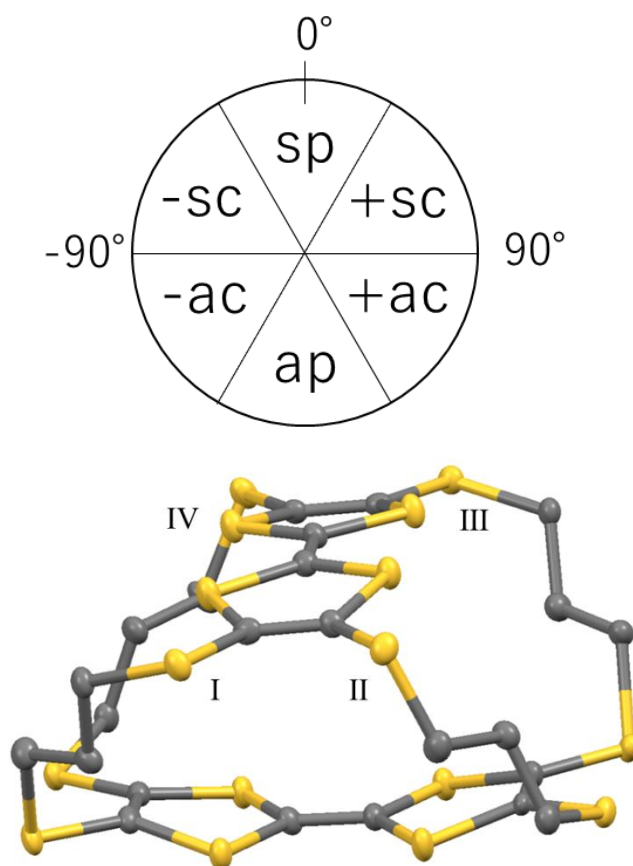


Figure 3-17. Schematic diagram of the alkyl chain conformation in the **TBC3** donor molecule.

Table 3-4. Alkyl chain conformations in the **TBC3** donor molecule in HTP of **TBC3·Br·TCE₂**.

	HTP	Atom1	Atom2	Atom3	Atom4	Torsion	Conformation
I		C5	S9	C13	C14	71.1(5)	+sc
		S9	C13	C14	C15	-158.5(5)	ap
		C13	C14	C15	S14	175.9(5)	ap
		C14	C15	S14	C10	-68.1(6)	-sc
II		C6	S10	C16	C17	66.0(6)	+sc
		S10	C16	C17	C18	-178.4(5)	ap
		C16	C17	C18	S15	162.7(5)	ap
		C17	C18	S15	C11	-70.2(6)	-sc
III		C7	S11	C19	C20	71.2(5)	+sc
		S11	C19	C20	C21	-159.5(5)	ap
		C19	C20	C21	S16	178.2(5)	ap
		C20	C21	S16	C12	-69.3(5)	-sc
IV		C8	S12	C22	C23	66.8(6)	+sc
		S12	C22	C23	C24	-178.9(5)	ap
		C22	C23	C24	S13	159.2(5)	ap
		C23	C24	S13	C9	-68.5(5)	-sc

Table 3-5. Alkyl chain conformations in the **TBC3** donor molecule in LTP of **TBC3·Br·TCE₂**.

LTP1	Atom1	Atom2	Atom3	Atom4	Torsion	Conformation	LTP2	Atom1	Atom2	Atom3	Atom4	Torsion	Conformation
I	C5'	S9'	C13'	C14'	67.4(9)	+sc	I	C5''	S11''	C13''	C14''	67.8(9)	+sc
	S9'	C13'	C14'	C15'	-167.5(8)	ap		S9''	C13''	C14''	C15''	-160.5(8)	ap
	C13'	C14'	C15'	S14'	59(1)	+sc		C13''	C14''	C15''	S14''	64(1)	+sc
	C14'	C15'	S14'	C10'	70(1)	+sc		C14''	C15''	S14''	C10''	74(1)	+sc
II	C6'	S10'	C16'	C17'	-74.2(9)	-sc	II	C6''	S12''	C16''	C17''	70(1)	+sc
	S10'	C16'	C17'	C18'	165.7(8)	ap		S10''	C16''	C17''	C18''	175.8(9)	ap
	C16'	C17'	C18'	S15'	178.7(8)	ap		C16''	C17''	C18''	S15''	160.8(9)	ap
	C17'	C18'	S15'	C11'	64(1)	+sc		C17''	C18''	S15''	C11''	-70(1)	-sc
III	C7'	S11'	C19'	C20'	-69(1)	-sc	III	C7''	S9''	C19''	C20''	72.1(9)	+sc
	S11'	C19'	C20'	C21'	-175.0(9)	ap		S11''	C19''	C20''	C21''	-160.5(8)	ap
	C19'	C20'	C21'	S16'	-158.9(9)	ap		C19''	C20''	C21''	S16''	-176.5(8)	ap
	C20'	C21'	S16'	C12'	71(1)	+sc		C20''	C21''	S16''	C12''	-67(1)	-sc
IV	C8'	S12'	C22'	C23'	-69.8(9)	-sc	IV	C8''	S12''	C22''	C23''	-67.9(9)	-sc
	S12'	C22'	C23'	C24'	159.7(9)	ap		S12''	C22''	C23''	C24''	165.8(8)	ap
	C22'	C23'	C24'	S13'	-63(1)	-sc		C22''	C23''	C24''	S13''	-59(1)	-sc
	C23'	C24'	S13'	C9'	-80(1)	-sc		C9''	S13''	C24''	C23''	-75(1)	-sc

Table 3-6. Alkyl chain conformations in the **TBC3** donor molecules in the neutral crystal.

Donor1	Atom1	Atom2	Atom3	Atom4	Torsion	Conformation	Donor2	Atom1	Atom2	Atom3	Atom4	Torsion	Conformation
I	C5	S9	C13	C14	-46.8(5)	-sc	I	C5'	S9'	C13'	C14'	62.1(5)	+sc
	S9	C13	C14	C15	-156.7(4)	ap		S9'	C13'	C14'	C15'	-166.9(4)	ap
	C13	C14	C15	S14	-177.2(4)	ap		C13'	C14'	C15'	S14'	-160.5(4)	ap
	C14	C15	S14	C10	76.1(4)	+sc		C14'	C15'	S14'	C10'	-63.2(5)	-sc
II	C6	S10	C16	C17	-75.8(4)	-sc	II	C6'	S10'	C16'	C17'	64.2(5)	+sc
	S10	C16	C17	C18	-178.8(4)	ap		S10'	C16'	C17'	C18'	156.9(4)	ap
	C16	C17	C18	S15	-69.9(6)	-sc		C16'	C17'	C18'	S15'	163.4(4)	ap
	C17	C18	S15	C11	-87.5(5)	-sc		C17'	C18'	S15'	C11'	-72.9(4)	-sc
III	C7	S11	C19	C20	-41(1)	-sc	III	C7'	S11'	C19'	C20'	-61.3(5)	-sc
	S11	C19	C20	C21	-173.5(8)	ap		S11'	C19'	C20'	C21'	-160.9(4)	ap
	C19	C20	C21	S16	-164.9(7)	ap		C19'	C20'	C21'	S16'	-168.7(4)	ap
	C20	C21	S16	C12	51.8(7)	+sc		C20'	C21'	S16'	C12'	67.4(4)	+sc
IV	C8	S12	C22	C23	-83.4(4)	-sc	IV	C8'	S12'	C22'	C23'	58.7(4)	+sc
	S12	C22	C23	C24	-67.2(5)	-sc		S12'	C22'	C23'	C24'	170.6(3)	ap
	C22	C23	C24	S13	-177.7(4)	ap		C22'	C23'	C24'	S13'	-179.0(3)	ap
	C23	C24	S13	C9	-71.4(4)	-sc		C9'	S13'	C24'	C23'	-74.1(4)	-sc

Table 3-7. Summary of the alkyl chain conformations in the **TBC3** donor molecule.

	HTP	LTP1	LTP2	Donor1	Donor2
I	sc·ap·ap·sc	sc·ap·sc·sc	sc·ap·sc·sc	sc·ap·ap·sc	sc·ap·ap·sc
II	sc·ap·ap·sc	sc·ap·ap·sc	sc·ap·ap·sc	sc·ap·sc·sc	sc·ap·ap·sc
III	sc·ap·ap·sc	sc·ap·ap·sc	sc·ap·ap·sc	sc·ap·ap·sc	sc·ap·ap·sc
IV	sc·ap·ap·sc	sc·ap·sc·sc	sc·ap·sc·sc	sc·ap·sc·sc	sc·ap·ap·sc

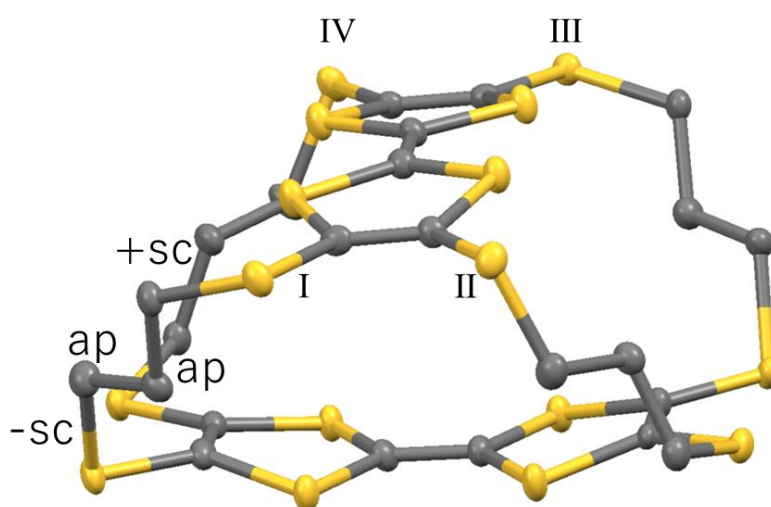


Figure 3-18. Schematic diagram of the alkyl chain conformation in the **TBC3** donor molecule in HTP of **TBC3·Br·TCE₂**.

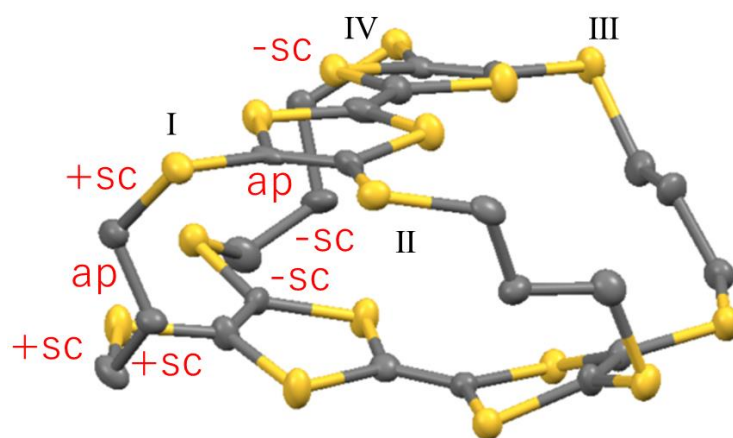


Figure 3-19. Schematic diagram of the alkyl chain conformation in the **TBC3** donor molecule in LTP of **TBC3·Br·TCE₂**.

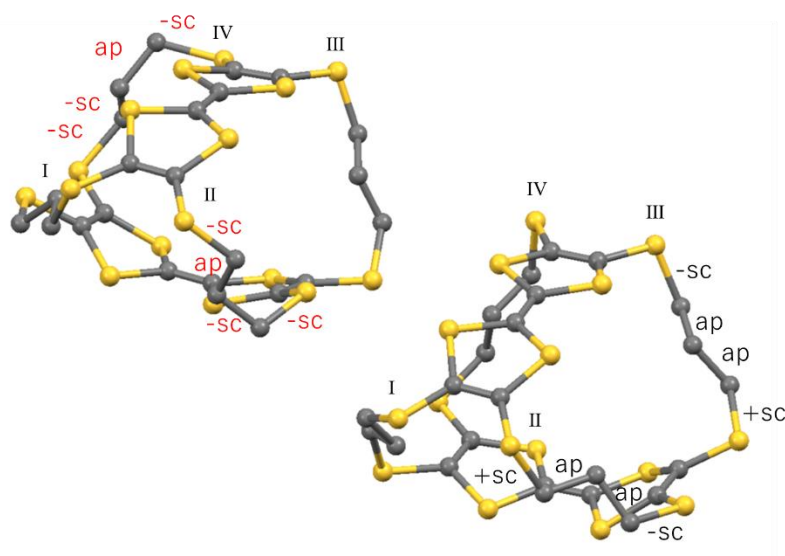


Figure 3-20. Schematic diagram of the alkyl chain conformation in the **TBC3** donor molecules in the neutral crystal.

Molecular arrangements in the crystal

The arrangements of donor molecules in the crystals are shown in Figs. 3-21 and 3-22. In the neutral donor crystal, the TTF skeleton is not aligned horizontal to the crystal axis, and adjacent TTF skeletons are vertically oriented to each other (Fig. 3-9). The closest S-S distance is 3.513 Å, as shown in Table 3-8. In the HTP of ion-radical salt, TTF units are arranged horizontally with respect to the crystal axis and are equivalent. Adjacent TTF skeletons are also arranged horizontally. The closest S-S distance was 3.445 Å between adjacent donors, whereas it was 3.490 Å along the stacking direction. In the LTP of ion-radical salt, the proportion of the distorted TTF skeleton in the direction of arrangement is not equivalent. The closest S-S distance was 3.398 Å between the adjacent donors, whereas it was 3.421 Å on the other side and 3.471 Å along the stacking direction.

Table 3-8. Selected short contact distances among donor molecules.

Neutral			HTP			LTP		
Atom1	Atom2	Length(Å)	Atom1	Atom2	Length(Å)	Atom1	Atom2	Length(Å)
C14	S15'	3.466	S13	S16	3.445	S9''	S12''	3.398
S9'	C24'	3.479	S13	S15	3.463	S12'	S9'	3.421
S16	S4'	3.513	S14	S15	3.474	S10'	C8''	3.454
S11	S7'	3.575	S9	S12	3.476	S4'	S2''	3.471
			S2	C9	3.479	C5'	S11''	3.479
			C5	S6	3.479	S3'	S1''	3.48
			S2	S5	3.49	S9''	S11''	3.505
			C6	S5	3.497	S10''	S11''	3.512
			S9	S11	3.498	S11'	S10'	3.515
			S10	S11	3.503	S12'	S10'	3.521
			S1	S6	3.506	S14'	S15'	3.566
			S11	S8	3.592			

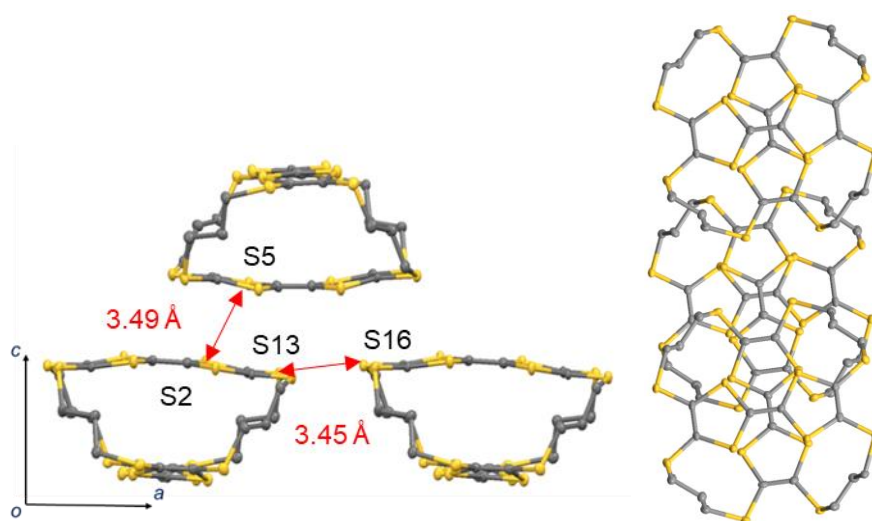


Figure 3-21. Donor molecule in the crystal structure of $\text{TBC3}\cdot\text{Br}\cdot\text{TCE}_2$ (HTP).

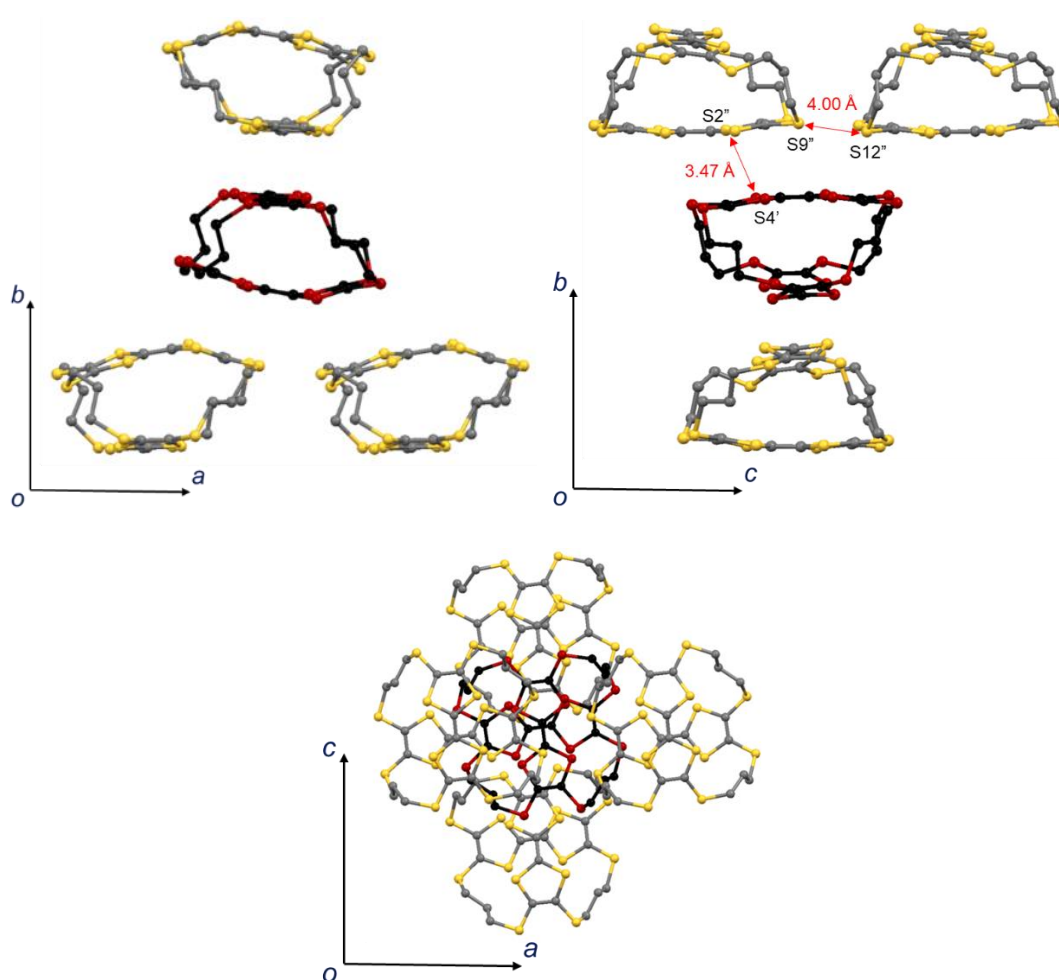


Figure 3-22. Donor molecule in the crystal structure of $\text{TBC3}\cdot\text{Br}\cdot\text{TCE}_2$ (LTP).

3-6. Theoretical calculations

Since the X-ray crystal structure analysis was of sufficient quality, theoretical calculations could be performed at the molecular level using the obtained crystal structure. Using B3LYP/6-31G* in Gaussian16, the molecular orbital, its energy, and the relative heat of formation were calculated. For donor molecules in ion-radical salts, calculations were performed for the HTP and two types of structures, LTP-A and LTP-B, in the LTP. Regarding the crystals of neutral donor molecules, there are two types of structures with different alkyl chain conformations, Neutral H-type, which resembles the HTP, and Neutral L-type, which resembles the LTP. Since the accuracy of the position of the hydrogen atom is low in the X-ray crystal structure analysis, only the hydrogen atoms were optimized, and the coordinates of the other atoms obtained from the X-ray crystal structure analysis were used directly. For those structures, the energies of the neutral state and the cation radical state were obtained and compared with each other. The energy of each molecule is shown in Fig. 3-23. The HTP structure of the ion-radical salt is the most stable in both the neutral and cation radical states. It can also be seen that the instability of the LTP-type structures compared to the HTP-type structures is reduced in the cation radical state as compared with the neutral state. It can be said that the LTP-type structure has a large stabilizing effect in the cation radical state.

Table 3-9. The energy of the structure in each donor molecule.

	Neutral State / eV	Cation Radical State / eV
HTP	0	0
LTP_A	1.3897	0.8463
LTP_B	1.1629	0.5872
Neutral (H-type)	0.5360	0.4877
Neutral (L-type)	1.2304	1.1058

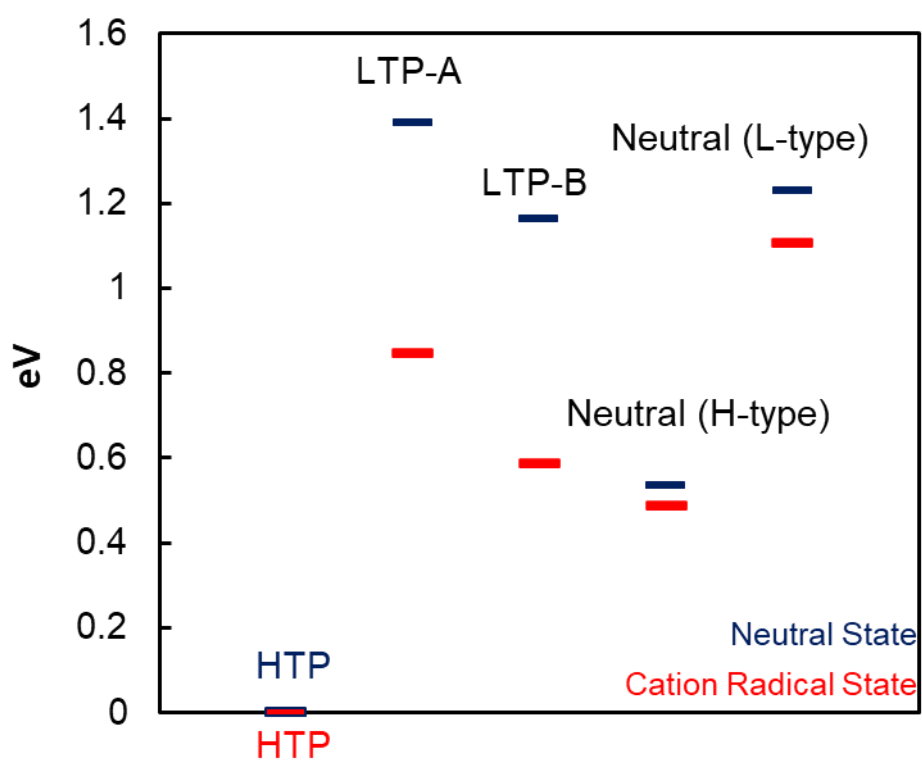


Figure 3-23. The energy of the structure in each donor molecule, based on the structure of the donor molecule in HTP.

The distributions of MO coefficients of donor molecules in HTP and LTP of $\text{TBC3}\cdot\text{Br}\cdot\text{TCE}_2$ are calculated in B3LYP/6-31G(d) level using Gaussian16 program package and shown in Fig. 3-24. In HTP, HOMO (highest occupied orbital) and HOMO-1 (next HOMO) are distributed in different TTF skeletons and interact between adjacent facing molecules. In LTP, molecular structure of TBC3 deformed and the TTF skeleton is greatly bent on one side and closer to a flat surface on the other side. In this phase, HOMO distributes on the flat side whereas HOMO-1 distributes on the bent side. Judging from the MO distribution, the positive charge mainly distributes on the planar one in the cation-radical state. Therefore, HOMO and HOMO, and HOMO-1 and HOMO-1 interact between adjacent facing molecules in the LTP.

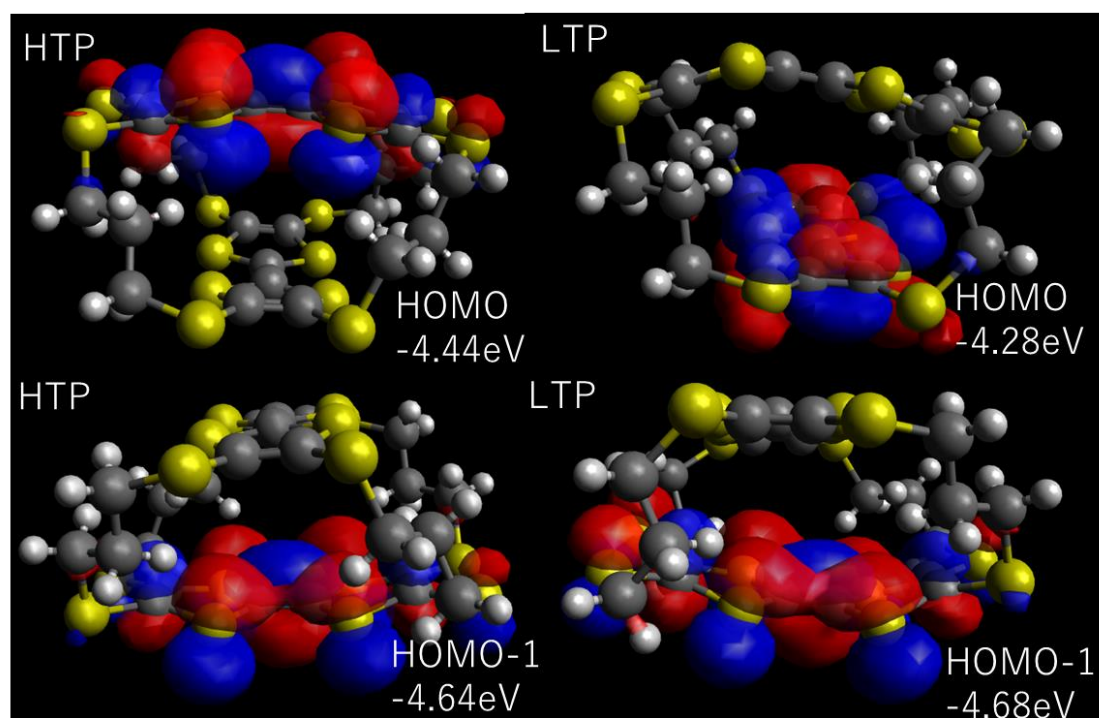


Figure 3-24. The distributions of MO coefficients of donor molecules in HTP and LTP of $\text{TBC3}\cdot\text{Br}\cdot\text{TCE}_2$ are calculated in B3LYP/6-31G(d) level using Gaussian16 program package.

Furthermore, Table 3-10 shows the results of theoretical calculation of the Charge on each C and S atom in the TTF skeleton of the donor molecule in the **TBC3·Br·TCE₂** crystal. As a result, the charges on TTF were estimated to be 0.67 (LT-TTF-a) and 0.33 (LT-TTF-b) in one molecule in LTP, while they were estimated to be 0.54 (LT-TTF-a') and 0.46 (LT-TTF-b') in the other molecule. Comparing with the charge distribution estimated from the formula using the bond length of BEDT-TTF in Fig. 3-15, the results that the difference in charge distribution is large for one donor molecule and small for the other are consistent.

Table 3-10. Values of the Charge on each C and S atom in the TTF skeleton of the donor molecule in the LTP of TBC3·Br·TCE₂ crystal.

LT-TTF-a	charge	LT-TTF-b	charge	LT-TTF-a'	charge	LT-TTF-b'	charge
C1'	-0.323	C3'	-0.317	C1''	-0.325	C3''	-0.331
C2'	-0.326	C4'	-0.332	C2''	-0.331	C4''	-0.318
C5'	-0.315	C9'	-0.297	C5''	-0.261	C9''	-0.287
C6'	-0.263	C10'	-0.283	C6''	-0.301	C10''	-0.289
C7'	-0.299	C11'	-0.324	C7''	-0.268	C11''	-0.249
C8'	-0.264	C12'	-0.243	C8''	-0.310	C12''	-0.319
S1'	0.391	S5'	0.305	S1''	0.353	S5''	0.332
S2'	0.358	S6'	0.313	S2''	0.347	S6''	0.328
S3'	0.374	S7'	0.300	S3''	0.338	S7''	0.305
S4'	0.375	S8'	0.291	S4''	0.363	S8''	0.335
S9'	0.236	S13'	0.216	S9''	0.246	S13''	0.250
S10'	0.284	S14'	0.246	S10''	0.209	S14''	0.248
S11'	0.217	S15'	0.198	S11''	0.274	S15''	0.272
S12'	0.259	S16'	0.267	S12''	0.240	S16''	0.208
total	0.704	total	0.343	total	0.574	total	0.484
Normalization	0.673	Normalization	0.327	Normalization	0.542	Normalization	0.458

Intermolecular interactions were also evaluated from the theoretical calculations. Four structures of donor molecules in HTP were extracted along the *a*-axis, and the interactions between two of the four donor molecules were calculated using the ADF program package on the PW91/TZ2P level. The structures of LTP were calculated along the two directions in which the distorted TTF skeletons face each other (*a*-axis) and the flat surfaces are arranged (*c*-axis). The pairs of interacting orbitals are indicated in Figure 3-25. The values of the charge transfer integrals were calculated from the obtained overlap integrals and resonance integrals.

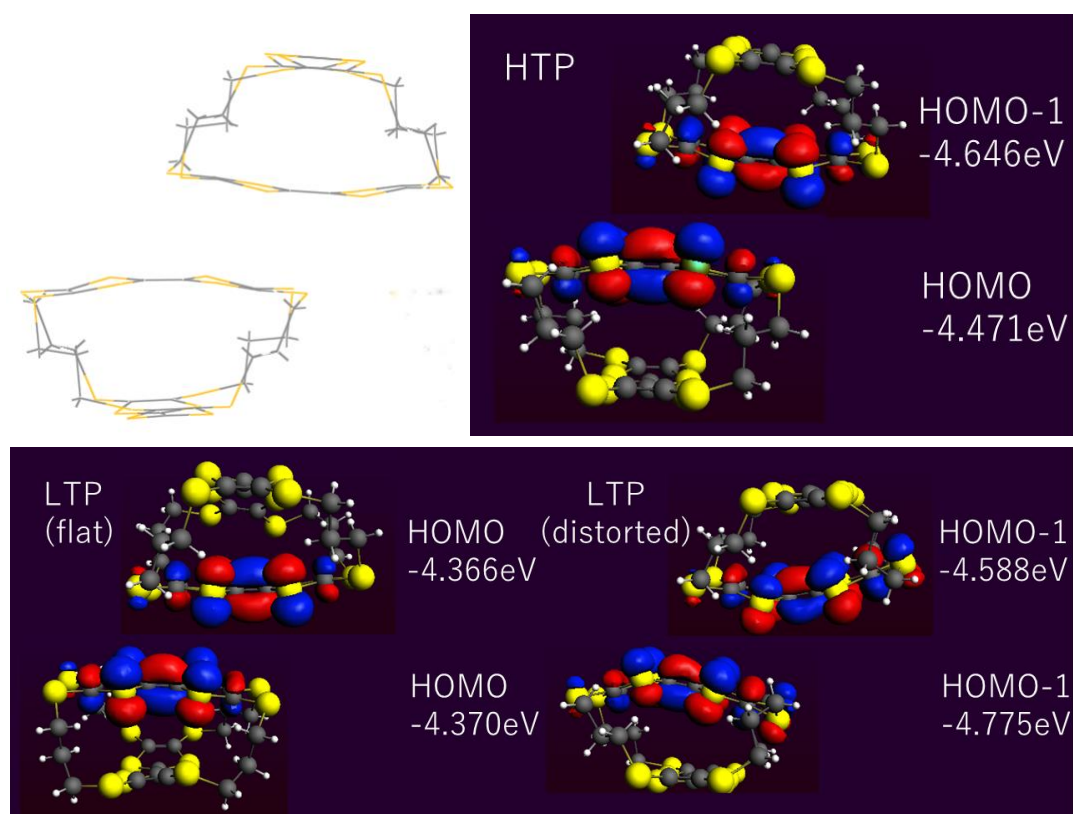


Figure 3-25. The distributions of MO coefficients on the donor molecule in the $\text{TBC3} \cdot \text{Br} \cdot \text{TCE}_2$ are calculated in PW91/TZ2P level using the ADF program package.

In addition, the changes in conductivity in the structures of the HTP and LTP were investigated based on the transfer integral (V) calculated from the resonance integral (H_{ab}), overlap integral (S_{ab}), and the energies of the corresponding orbitals, as summarized in Table 3-11. In the structure of the HTP, the closest distance between the centers of donor molecules was 8.925 Å, and the charge transfer integral was calculated to be 202 meV in that direction. In the LTP, one of the two TTF skeletons of the **TBC3** molecule is distorted, and there are intermolecular elements in which the distorted TTF skeletons face each other and molecules in which the flat TTF skeletons face each other. Between donor molecules facing the distorted side of the TTF skeleton, the closest contact distance was as large as 9.366 Å and the charge transfer integral was as low as 60.5 meV. On the other hand, between donor molecules facing flat TTF skeletons, the closest distance was as small as 8.748 Å and the charge transfer integral was as high as 210 meV. This suggests that there is a large difference in conductivity between the direction in which the distorted TTF skeleton is arranged and the direction in which the flat TTF skeleton is arranged in the LTP.

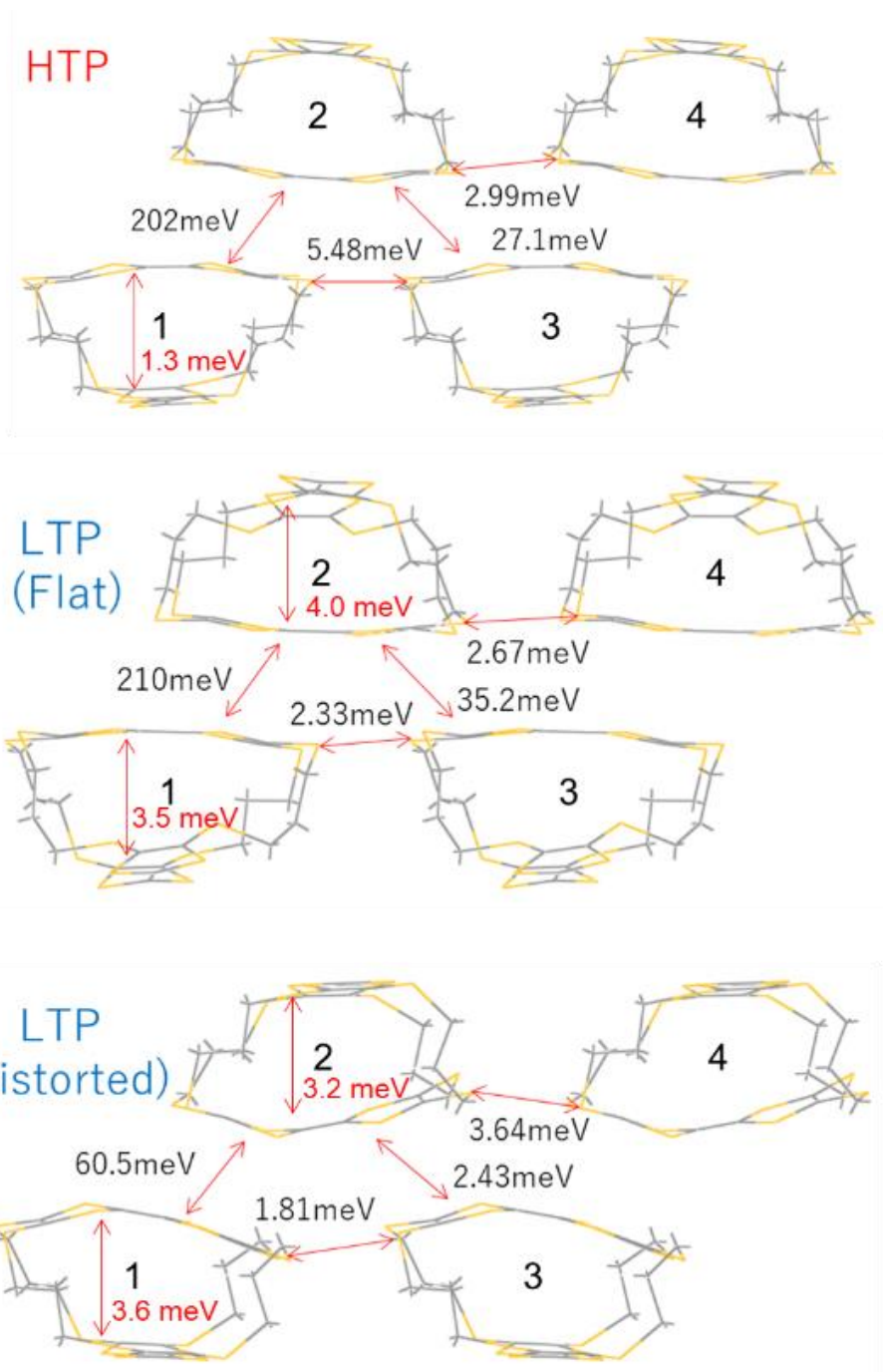


Figure 3-26. Intermolecular transfer integral of TBC3·Br·TCE₂ (ADF, PW91/TZ2P).

Table 3-11. Values of the resonance integral (H_{ab}), overlap integral (S_{ab}), and transfer integral between each molecular pair.

HT: High temperature phase. Ltf: Low temperature phase with flat surfaces facing each other.

LTd: Low temperature phase with distorted surfaces facing each other.

	H_{ab} /meV	S_{ab} /meV	$d/\text{\AA}$	V /meV	Interaction
HT 1-2	367	-37.4	8.93	202	HOMO : HOMO-1
HT 1-3	10.6	-1.13	12.3	5.48	HOMO : HOMO-1
HT 2-3	47.7	-4.64	10.5	27.1	HOMO : HOMO-1
HT 2-4	5.57	-0.57	12.4	2.99	HOMO : HOMO-1
HT 1-1	1.31	0	-	1.31	HOMO : HOMO-1*
LTf 1-2	379	-39.9	8.75	210	HOMO : HOMO
LTf 1-3	4.98	-0.60	12.3	2.33	HOMO : HOMO
LTf 2-3	64.8	-6.84	10.4	35.2	HOMO : HOMO
LTf 2-4	5.63	-0.67	12.3	2.67	HOMO : HOMO
LTf 1-1	3.45	0	-	3.45	HOMO : HOMO-1*
LTf 2-2	3.96	0	-	3.96	HOMO : HOMO-1*
LTd 1-2	110	-11.3	9.37	60.5	HOMO-1 : HOMO-1
LTd 1-3	2.48	-0.15	12.3	1.81	HOMO-1 : HOMO-1
LTd 2-3	4.76	-0.53	9.89	2.43	HOMO-1 : HOMO-1
LTd 2-4	9.22	-1.26	12.3	3.64	HOMO-1 : HOMO-1
LTd 1-1	3.55	0	-	3.55	HOMO : HOMO-1*
LTd 2-2	3.24	0	-	3.24	HOMO : HOMO-1*

*: intramolecular interaction between two TTF skeleton within the **TBC3** molecule.

3-7. Non-linear V - I characteristics of HTP and LTP crystals

As a non-linear V - I characteristics along the c -axis have been reported in previous studies, the same feature was observed in this study as well. The result is shown in Fig. 3-27: there was a negative differential resistance at 270 K in the HTP crystal along the c -axis.

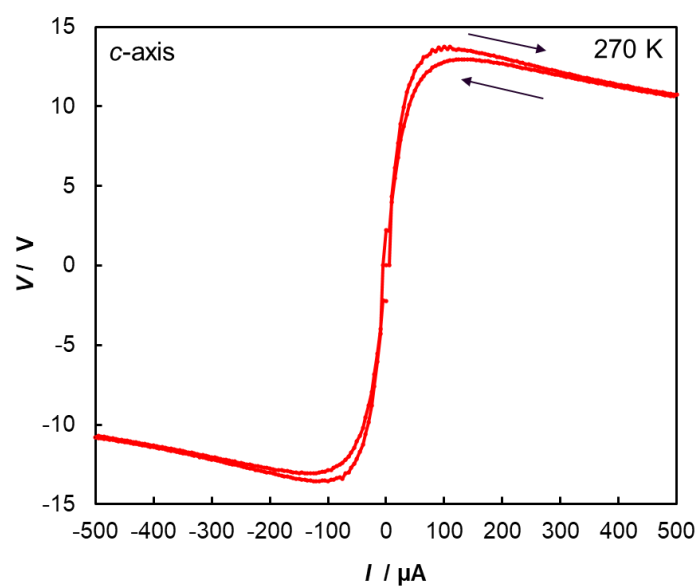


Figure 3-27. V - I characteristics of $\text{TBC3}\cdot\text{Br}\cdot\text{TCE}_2$ along the c -axis at 270 K .

Previously reported studies have interpreted the nonlinear conductivity of this system as the result of relaxation of the charge disproportionation in the crystal. It has been confirmed from the X-ray crystal analysis that the disproportionated charge within one donor molecule becomes delocalized between the paired donor skeletons in the **TBC3** molecule due to the influence of the current application in the low-resistance state. Due to this structural change, the activation energy of electron transfer in the **TBC3** molecule becomes much smaller than that in the original state, so that the resistance is greatly reduced. Due to the combination of structural equalization and charge delocalization, the low resistance state is maintained even after the applied current is reduced, and hysteretic behavior appears.

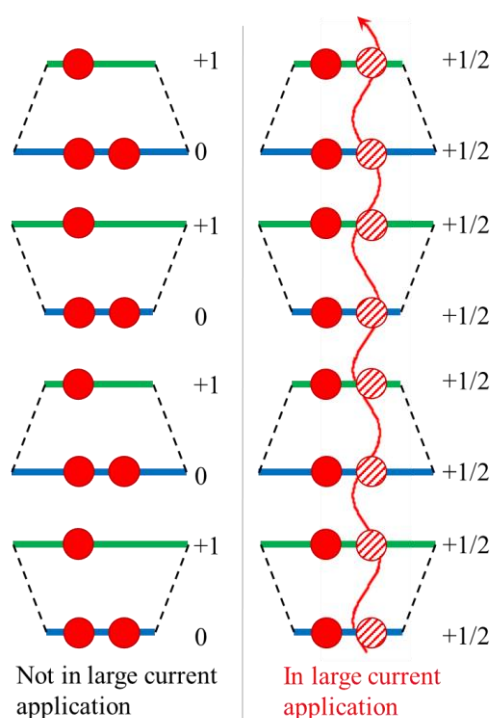


Figure 3-28. Schematic drawing of the charge-disproportionated state and current-induced charge-delocalized state of the crystal of **TBC3·Br·TCE2**.

Negative differential resistance due to current application was also observed along the *a*- and *b*-axis. Figures 3-29 shows the results of current-application / voltage-detection measurement at 200 K (HTP). It was found that the conductivity increases with increasing current, and non-linear conductivity including NDR was also observed along the *a*- and *b*-axes as well as along the *c*-axis. The results were also attributable to the relaxation of the disproportionation of the charge distribution in the conducting path by the application of the current, as shown in Fig. 3-30 resemble to the proposed mechanism in the previous work.

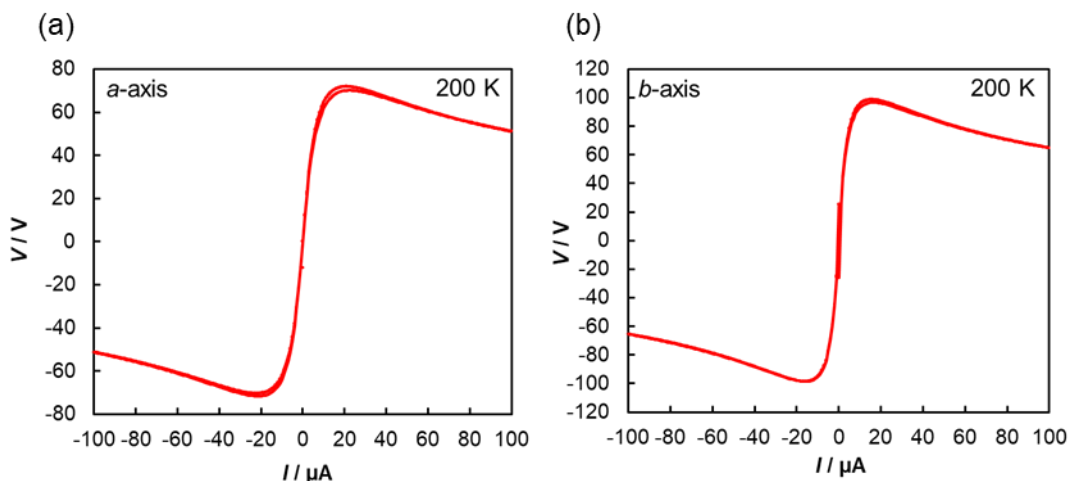


Figure 3-29. V - I characteristics of $\text{TBC3}\cdot\text{Br}\cdot\text{TCE}_2$ along the *a*-axis (a) and the *b*-axis (b) at 200 K.

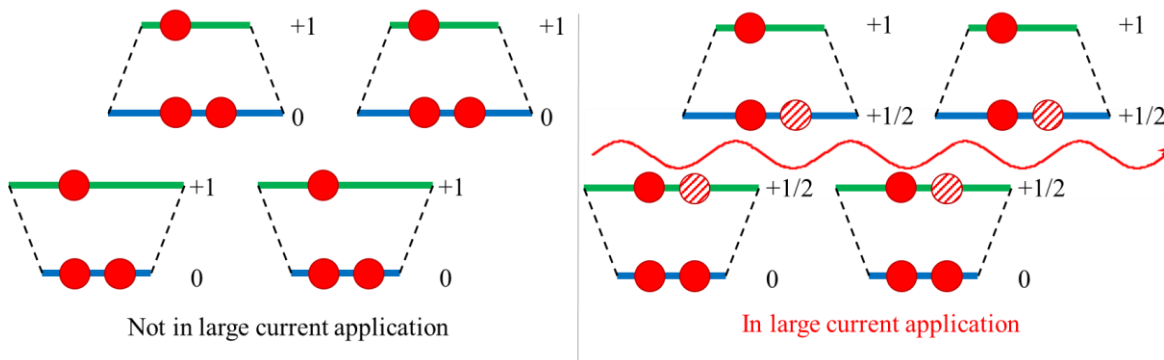


Figure 3-30. Schematic drawing of the charge-disproportionated state and current-induced charge-delocalized state of the crystal of $\text{TBC3}\cdot\text{Br}\cdot\text{TCE}_2$.

3-8. Relationship between the structural phase transition and physical properties

3-8-1. Temperature dependence of the resistance

Figure 3-31 shows the measurement results of the temperature dependence of resistivity with a constant-voltage applied / current-measurement condition, using the four-terminal method along the c -axis. The temperature was lowered from 300 K by 1 K/min, and the temperature was lowered to 120 K after holding the temperature for a sufficient time until the phase transition to LTP occurred at 155 K. Then, the temperature was raised at 1 K/min.

As a result, the resistance along the a - and b -axis decreased in LTP as shown in Fig. 3-32. When the temperature was slowly lowered at a speed of 0.1 K/min, the phase gradually changed to LTP at around 160 K, and when the temperature was raised, the phase transition occurred rapidly at around 175 K to HTP. A large hysteresis was observed, and the resistance in LTP was about 1/10 of that in HTP, which was similar to the previously reported results along the c -axis.

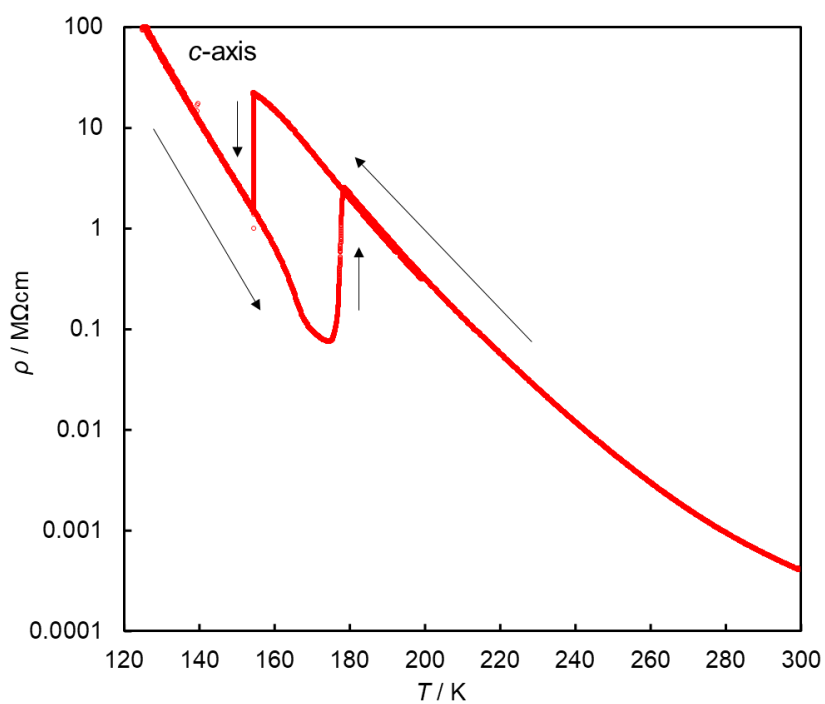


Figure 3-31. Temperature dependence of the resistivity of $\text{TBC3}\cdot\text{Br}\cdot\text{TCE}_2$ ($V = 1\text{V}$, c -axis).

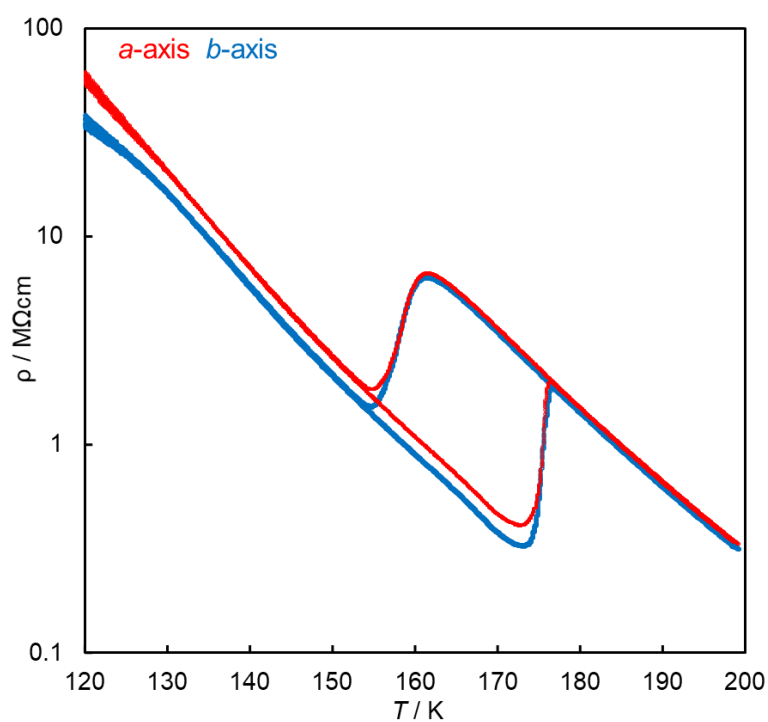


Figure 3-32. Temperature dependence of the resistivity of $\text{TBC3}\cdot\text{Br}\cdot\text{TCE}_2$ ($V = 1\text{V}$, a -axis(red) and b -axis(blue)).

From the temperature dependence of the conductivity, the activation energies for both the *a*- and *b*-axes were obtained (Table 3-12). In HTP, the activation energies for the *a*- and *b*-axis were the same, i.e., 0.239 eV, reflecting the equivalence of the axes, whereas the activation energies changed to 0.178 eV and 0.176 eV, respectively, in LTP. The activation energies for the *a*-axis and *b*'-axis (the *c*-axis for LTP and *b*-axis for HTP) in LTP differ depending on the crystal structural difference. These values were slightly different for the other sample; the activation energies for the *a*-axis and *b*'-axis were 0.21 eV and 0.18 eV, respectively. This activation energy in the thermal activation-type conductivity is the energy required to transform a molecule into an unstable structure upon electron transfer between molecules (reorientation energy, λ), and the dynamics of molecular deformation when a molecule in a crystal receives a charge differs depending on the direction of molecular distortion in LTP. In LTP, it is considered that the activation energy is different and unequal depending on how the molecules with different distortion directions are mixed.

The reorientation energy (λ) for the **TBC3** molecule has been calculated to be 0.27 eV. According to the Marcus theory, the activation energy for the intermolecular charge transfer is one-fourth of λ . But the activation energy typically distributes between λ and $\lambda/4$ in the real system. Since the TTF units in **TBC3** are connected by an alkyl chain, it is considered that molecular deformation due to electron transfer does not readily occur as it does for the usual individual molecules, and the activation energy becomes close to λ .

Table 3-12. Activation energy of **TBC3·Br·TCE₂**.

	Phase	Temperature	Activation energy
<i>a</i> -axis	HTP	200-165 K	0.239 eV
	LTP	160-130 K	0.178 eV
<i>b</i> -axis	HTP	200-165 K	0.239 eV
	LTP	160-130 K	0.176 eV
<i>c</i> -axis	HTP	200-165 K	0.287 eV
	LTP	160-130 K	0.256 eV

3-8-2. Temperature dependence of the magnetic susceptibility

The temperature dependence of the magnetic susceptibility of **TBC3·Br·TCE₂** was measured by a SQUID magnetometer using 2.04 mg of polycrystalline sample. After rapid cooling from 290 K to 2 K to quench the phase transition, the measurement was carried out from 2 K to 290 K. The result is shown in Fig. 3-33. The solid black circles show the results for the supercooled state of HTP without any phase transition. The discontinuous changes seen around 50 K are measurement problems and are not essential. In the plot containing red circles, the measurement is performed in 0.1 K increments between 200 K and 100 K, which includes the phase transition temperature. Similar to the results for the conductivity measurements, when the temperature is lowered, it slowly changes to LTP around 160 K, and when the temperature is raised from LTP, the magnetic susceptibility gradually increases around 165 K and suddenly changes to HTP around 175 K. In HTP, the Curie constant is 0.375 for one mole of **TBC3·Br·TCE₂** unit, suggesting one cation radical is carried per one **TBC3** molecule. The value in LTP is 0.21, which is about half of that in HTP.

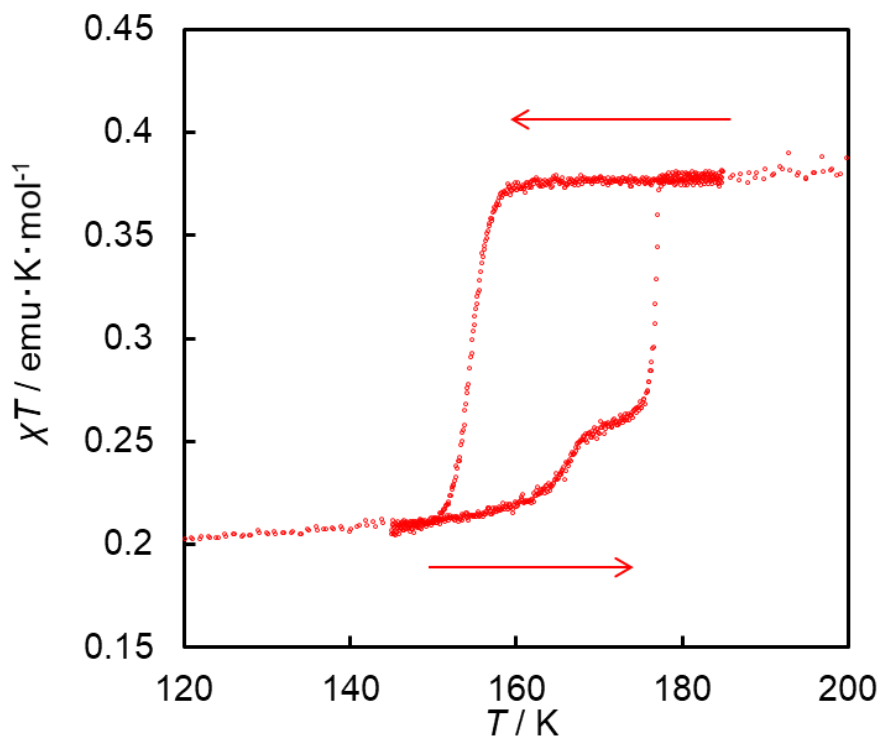
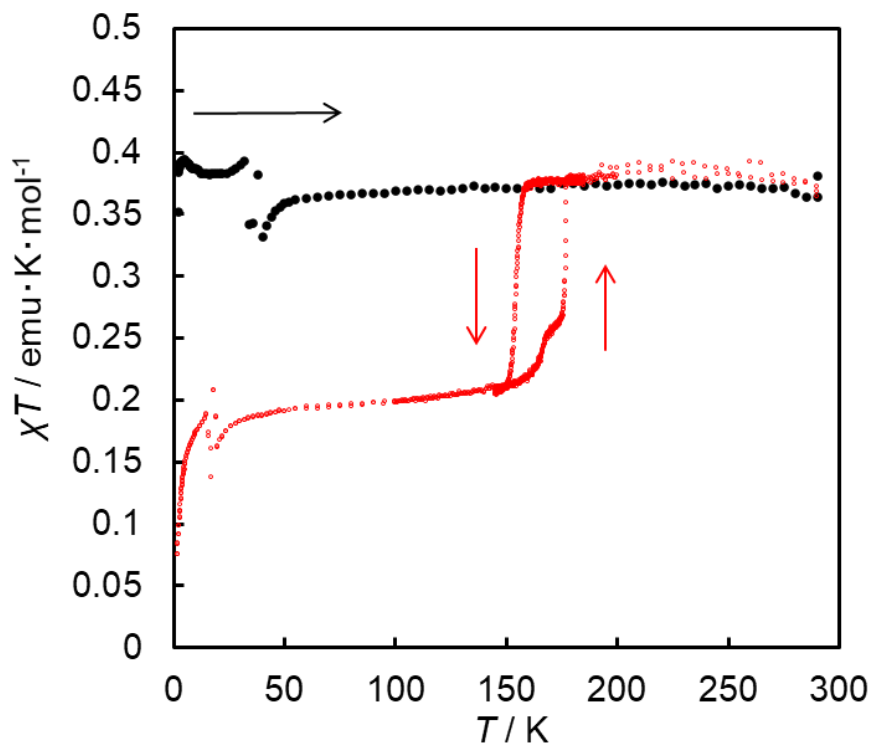


Figure 3-33. Temperature dependence of the magnetic susceptibility of $\text{TBC3} \cdot \text{Br} \cdot \text{TCE}_2$.

3-8-3. Relationship between the changes in structures and physical properties upon the phase transition.

In the **TBC3·Br·TCE₂** crystal, the resistance decreases to *ca.* 1/10 and the activation energy is reduced while the magnetic susceptibility becomes 1/2, upon phase transition from HTP to LTP. In the previous research, it was explained that the two equivalent axes in HTP become unequivalent, so that the axial interaction on the side where the TTF unit bends becomes stronger, and the independently detected cation radicals form the conduction band in LTP. This leads to an increase of the electrical conductivity and the spin-pairing to make them undetectable by magnetic measurements and a simultaneous increase in the conductivity. In this work, the charge distribution in the **TBC3·Br·TCE₂** crystal was evaluated in detail for both the HTP and LTP, and the results require different explanations. In the HTP, cation radicals are isolated on one side of the donor molecule, showing distinguished spin moment in magnetic measurement. By analogy with the discussions on the ion-radical salt of BEDT-TTF, which can be regarded as a half molecule of **TBC3**, the on-site Coulomb repulsive energy is estimated to be *ca.* 0.5 eV, and this value is higher than the transfer integral between the neighboring molecules in the HTP crystal (202 meV), and thus the HTP crystal can be regarded as a Mott insulator. This conclusion is consistent with the disproportionated crystal structure and also with the previous discussions.

On the other hand, in LTP, the structure of one of the TTF skeletons in the **TBC3** molecule becomes bent, while the other TTF skeleton has a flat structure, with the flat sides of the two skeletons facing each other and the bent sides of the two skeletons facing each other. Since the cationic charge makes the TTF skeleton flat and thereby increases the delocalization of the charge within the π -conjugating system, this structure seems to

represent a pairing between the cationic site and cationic site and between the neutral site and neutral site. However, the pairing between cationic sites leads to the spin-pairing, and all magnetic moments will be quenched in LTP with this explanation. This situation contradicts the observed result—namely, that the LTP still shows half of the magnetic moment observed in the HTP. In the newly obtained result, one of two **TBC3** molecules in the asymmetric unit of the LTP crystal has 0.46:0.54 charges on both TTF sides, whereas the other molecule has almost the same distribution as in the HTP crystal. However, the magnetic susceptibility that is still observed in LTP can not be simply explained by these values. Rather, it must be explained in terms of the structural disorder. Although the crystal structure is determined precisely, the standard deviation in LTP is relatively large. This would be due to the structural disorder of the cationic state and the neutral state. The 0.46:0.54 charges are considered to represent the average of the two kinds of structures. In this case, both the charge on the 0.46 side and that on the 0.54 side have the chance to show magnetic susceptibility. In the two facing sites, one side has a +0.46 charge whereas the other side has a +1.54 charge. On the 1.54 side, 0.54 of the magnetic moment will disappear through the spin-coupling, and the residual 0.46 will have a chance to show the magnetic moment. The other side showing 0.46 of the magnetic moment remains. Therefore, almost half of the spin moments survive in LTP.

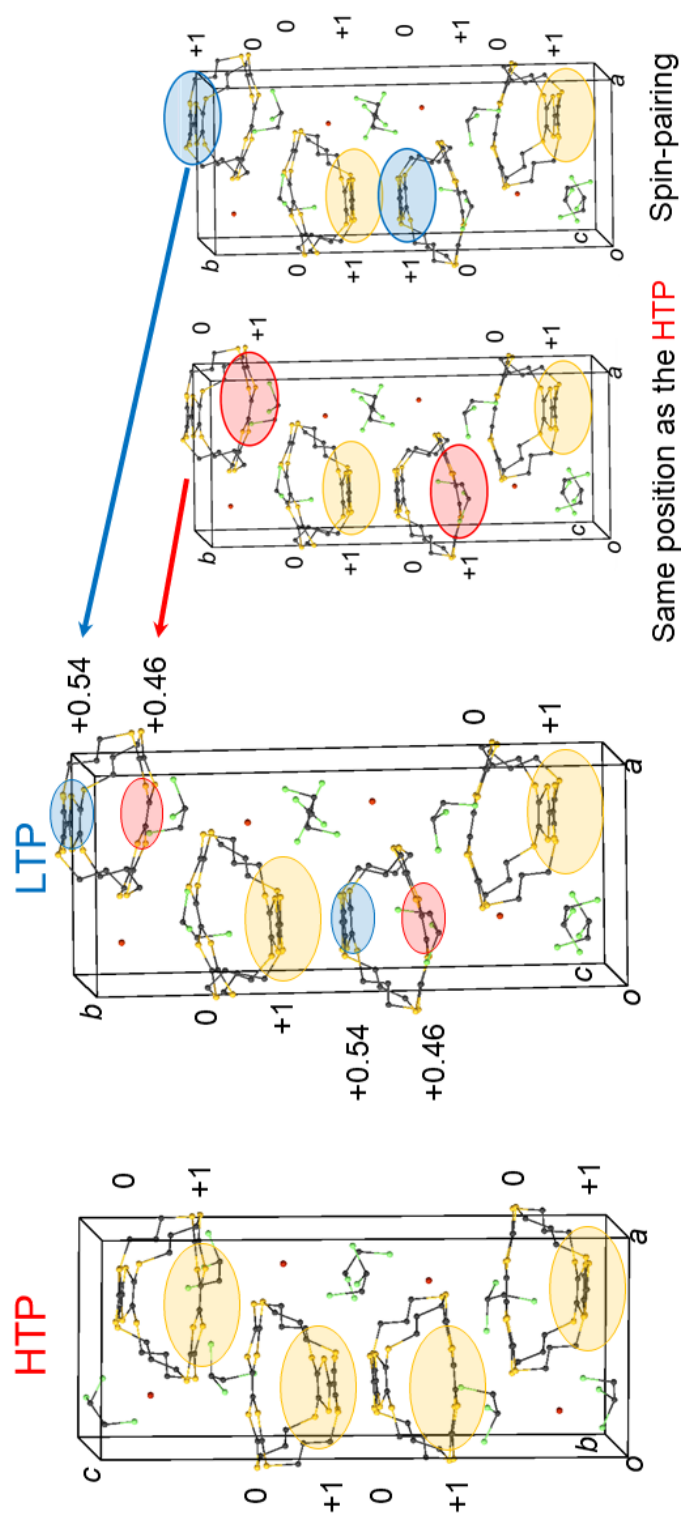


Figure 3-35. Relationship between the charge distribution and physical properties of HTP and LTP of $\text{TBC3}\cdot\text{Br}\cdot\text{TCE}_2$ crystal.

3-8-4. Impedance measurement

On a sample with two electrodes along c -axis (Figure 3-8), impedance measurement was carried out by changing the temperature. The measurement was performed while slowly increasing the temperature from a LTP of 150 K, and DC measurement was also performed in the same manner.

Figure 3-35(a) shows the results of the temperature dependence of impedance at each frequency and the comparison with the DC measurement (red line). Results similar to those for the DC measurements are obtained at low frequencies, but the results differ significantly at high frequencies. It can be seen that the temperature dependence in LTP changes before the phase transition from LTP to HTP and the impedance changes significantly. This is considered to be the same as the result in which the temperature dependence of the magnetic susceptibility also changed in two steps.

Figure 3-35 (b) is a plot of the temperature dependence of the phase at each frequency. The change in behavior that was seen before the sudden change due to the phase transition near 175 K was remarkable at 10 kHz, and the change in behavior differed depending on the frequency.

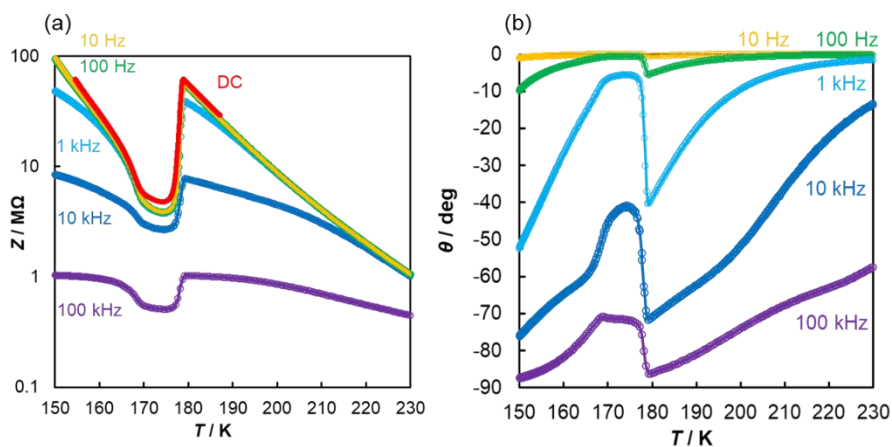


Figure 3-35. Temperature dependence of the impedance (a) and the phase angle (b) of **TBC3·Br·TCE₂**.

Figure 3-36 (b) shows the results of the frequency dependence of the phase at each temperature. The lower the temperature, the larger the phase change, but when comparing the LTP at 170 K and the HTP at 190 K, it can be seen that the frequency dependence changes due to the phase transition. Figure 3-36 (a) shows the results of the frequency dependence of impedance at each temperature. Similarly, the frequency dependence changes due to the phase transition.

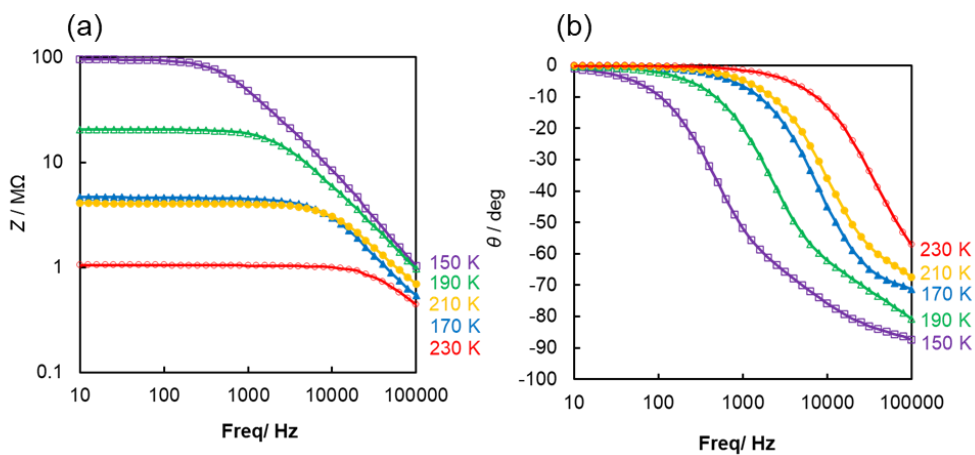


Figure 3-36. Frequency dependence of the impedance (a) and the phase angle (b) of TBC3·Br·TCE₂.

A Nyquist plot was prepared by converting from the impedance and phase measurement results. Figure 3-37 (a) shows the results of fitting using an equivalent circuit in which the resistance component existing in the measurement circuit, such as the contact resistance, is R_1 , the resistance component in a single crystal is R_2 , and the capacitor component is C_2 . However, the Nyquist plot based on the measurement results has a crumbled semicircle, and fitting was not possible with this equivalent circuit. Therefore, the results of fitting by an extended equivalent circuit, containing R_3 and C_3 in addition, were used as shown in Fig. 3-37 (b). The temperature dependence of the parameters obtained from the results of this fitting is shown in Fig. 3-38.

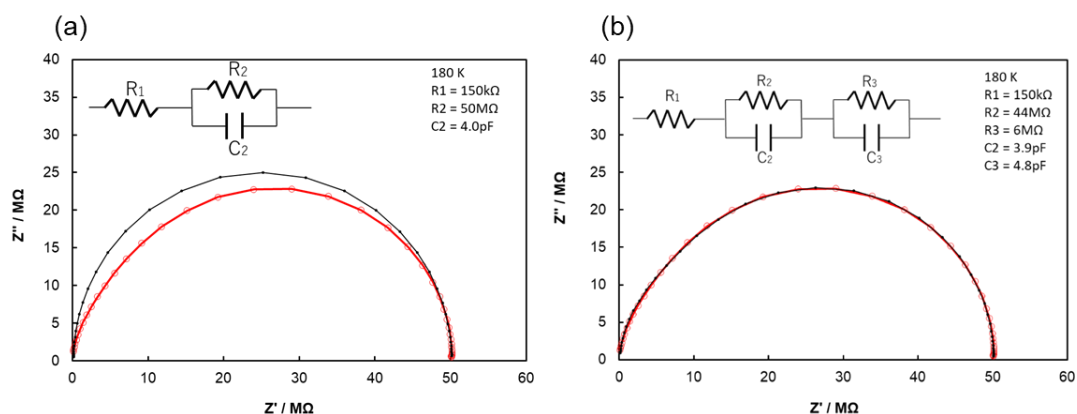


Figure 3-37. Nyquist plot and equivalent circuit 1 (a) and 2 (b).

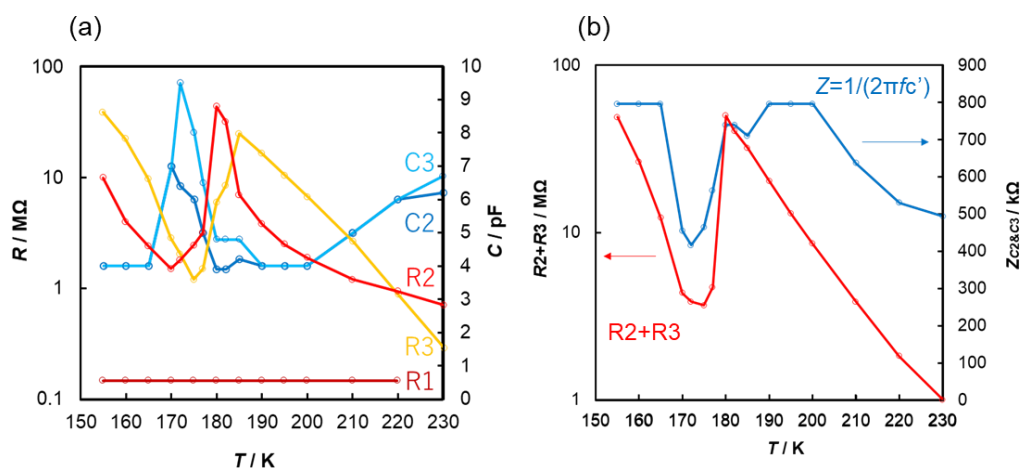


Figure 3-38. Temperature dependence of each parameter obtained by the Nyquist plot (a) and calculated parameters (b).

$$Z = 1 / (2\pi f c')$$

$$C' = 1 / (1/C2 + 1/C3)$$

Z was calculated and plotted with the frequency f as 100 kHz.

At the phase transition, the AC impedance of $\text{TBC3} \cdot \text{Br} \cdot \text{TCE}_2$ basically behaves like DC conductivity. Although it behaves slightly differently depending on the measurement frequency, the behavior at 10 Hz to 10 kHz can be almost completely reproduced by assuming that a certain capacitance component (0.152 pF) is connected in parallel (Fig. 3-39). However, at 100 kHz, a remarkable decrease in impedance is shown in the phase

transition region, which is considered to be mainly due to the contribution of the crystal solvent. When the solvent arrangement is extracted from the results of X-ray crystal structure analysis (Fig. 3-40), the dipole moment of the solvent molecule remains uncanceled in the channel in HTP. On the other hand, in LTP, the dipole moments between the adjacent solvent molecules cancel each other. Therefore, in the vicinity of the phase transition temperature where the energies of the two crystal phases approach each other, a movable space for the solvent is expanded, and the impedance decreases following the applied AC electric field. On the other hand, when the phase transition to LTP is completed, the contribution of the solvent molecule for the impedance disappears and only the electrical resistance component remains. In order to examine this phenomenon in more detail, a Nyquist plot is created from the frequency dependence of the impedance at each temperature, and the temperature change of each component is extracted from the fitting to the equivalent circuit network. The contributions on the impedance from resistance (R2, R3) and capacitor (C2, C3) components are almost the same range near the phase transition as shown in Figure 3-38. Both of the capacitor components (C2 and C3) exhibit similar behaviors and rise in the phase transition region, and these increases are considered to represent the contribution of the solvent molecule described above. On the other hand, regarding the resistance component, the overall behavior of increasing at low temperature, decreasing at the phase transition point, and increasing thereafter is similar, but one is linear with respect to the log scale (Arrhenius plot) and the other is changing curvilinearly. The electrical conductivity mechanism in this crystal is basically hopping conduction, but the process is divided into hopping between two sites in the molecule and hopping between molecules. The crystal lattice constant increases with increasing temperature, but the change at this time is mainly due

to the intermolecular distance, and the interatomic distance in the molecule is not significantly affected by the temperature. That is, the two components separated by the Nyquist plot are thought to represent two types of intramolecular and intermolecular charge transfer processes within the crystal (Figure 3-41).

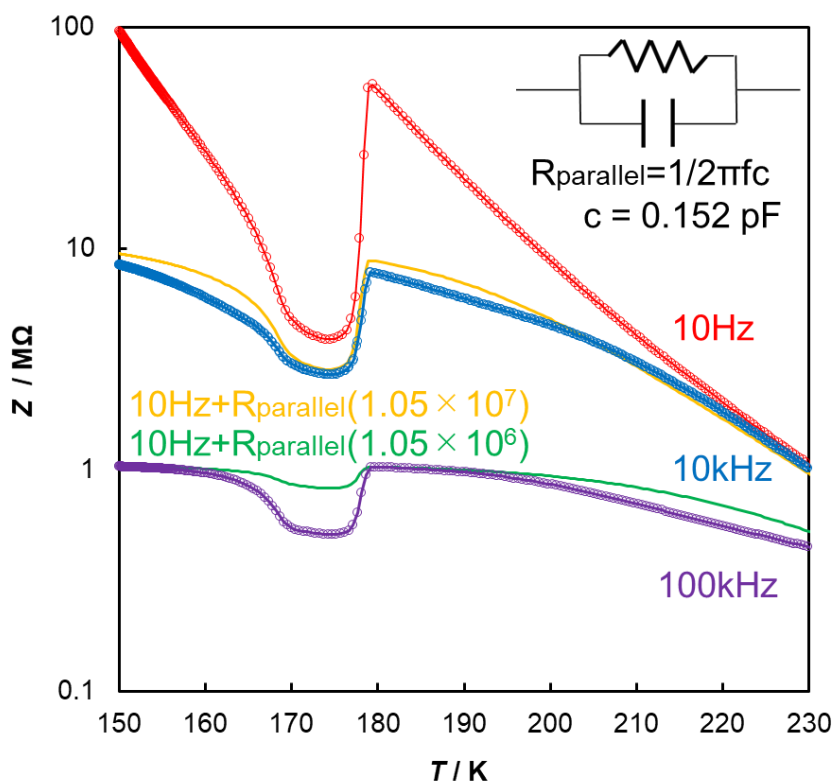


Figure 3-39. Temperature dependence of the impedance of $\text{TBC3} \cdot \text{Br} \cdot \text{TCE}_2$.

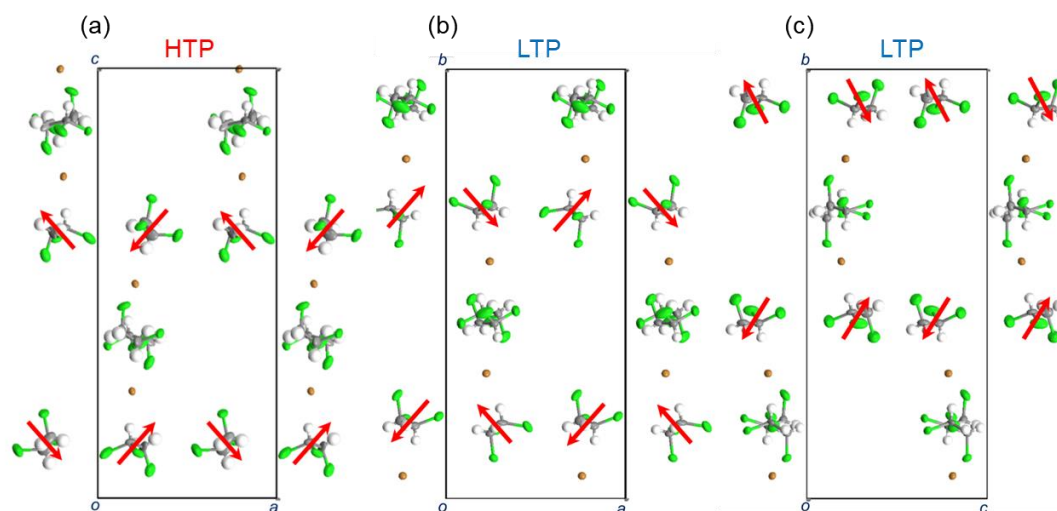


Figure 3-40. Anion and solvent molecules in the crystal structure of $\text{TBC3}\cdot\text{Br}\cdot\text{TCE}_2$ in HTP (a) and LTP viewed from c -axis (b) and a -axis (c).

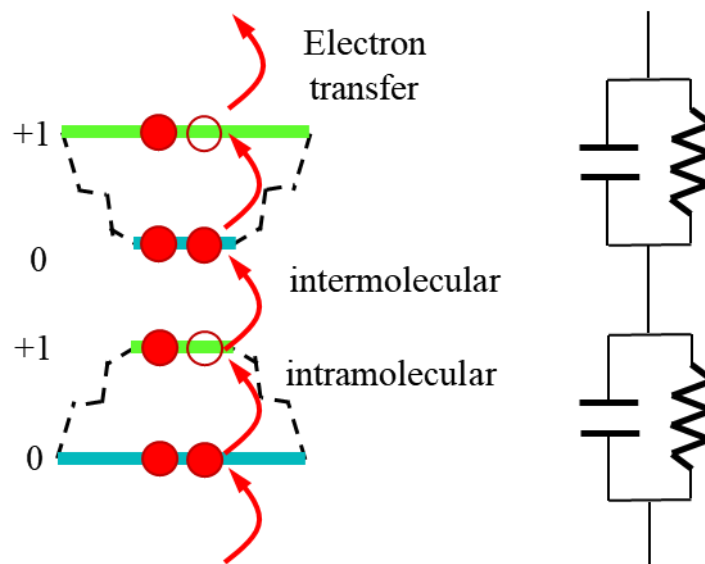


Figure 3-41. Schematic diagram of two types of intramolecular and intermolecular charge transfer processes within the crystal.

3-8-5. ESR measurement

For each of the HTP and LTP of $\text{TBC3}\cdot\text{Br}\cdot\text{TCE}_2$, the g value of the electron spin resonance spectrum was calculated by DTF method (B3LYP/6-31G(d) with prop = epr option) based on the X-ray structure. For the HTP, the angle-dependent result of the g value is well reproduced. Regarding the LTP, it is predicted that anisotropy will be observed in the ac plane (ab' plane, corresponds to the HTP), but it has not yet been measured at this time. As a matter of fact, in LTP, domains having different axis directions are mixed, so that the anisotropy is considered to be smaller than the predicted value (the value obtained by averaging).

Table 3-13. The results of theoretical calculation of the g value.

	a - axis	b - axis	c - axis
HTP	2.0124	2.0124	2.0056
LTP	2.0133	2.0099	2.0038

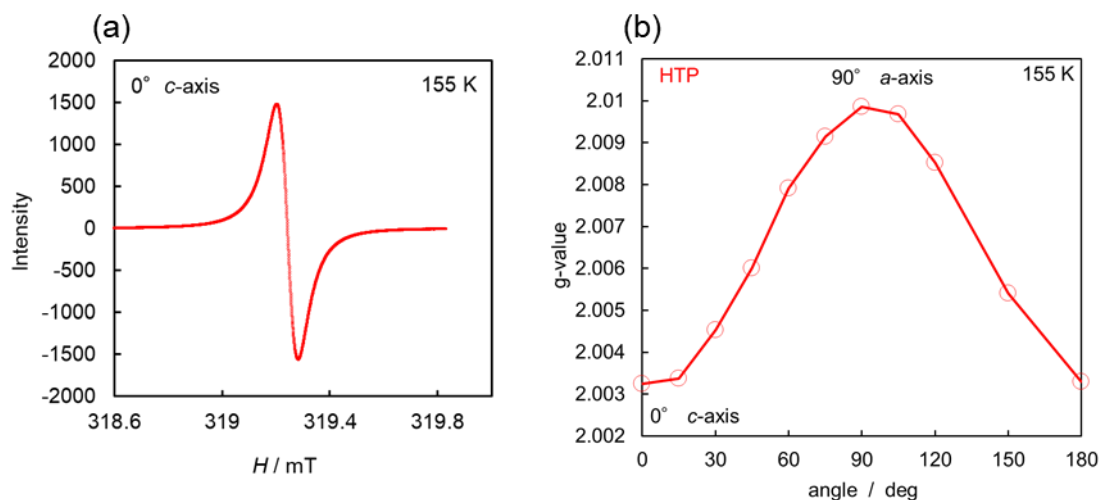


Figure 3-42. Result of ESR measurement (a) and angle dependence of the g value by ESR measurement of $\text{TBC3}\cdot\text{Br}\cdot\text{TCE}_2$ (b).

3-9. Temperature dependence of the structural phase transition rate

Regarding the temperature dependence of the resistance, the temperature was lowered from 200 K, the temperature was maintained at each temperature below the phase transition temperature, the change in resistance was measured, and the time required for the transition from HTP to LTP was determined. An Arrhenius plot was prepared from the phase transition rate constant k at each temperature (Fig. 3-45). The activation energy was 0.266 eV. Similar measurements were performed on different crystals and found to be 0.276 eV.

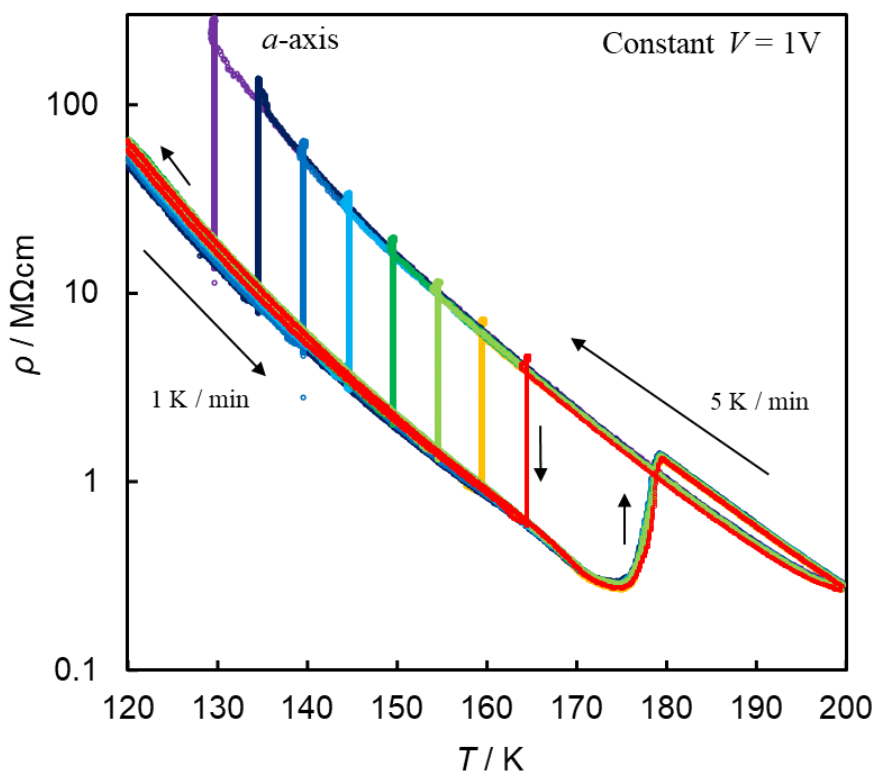


Figure 3-43. Temperature dependence of the resistivity of $\text{TBC}_3 \cdot \text{Br} \cdot \text{TCE}_2$ ($V = 1\text{V}$, a -axis). The temperature sweep stops until the phase transition from HTP to LTP.

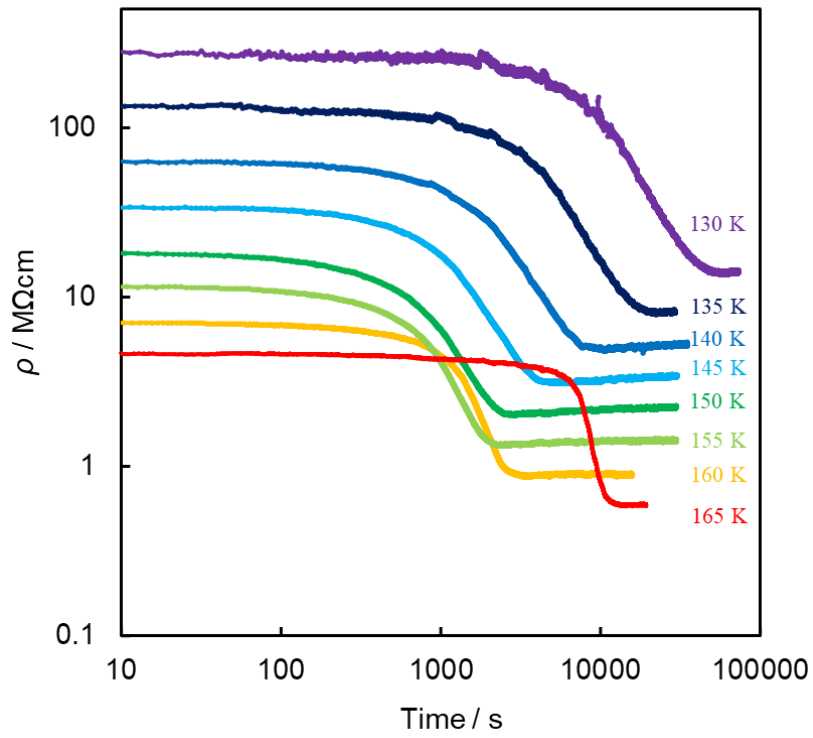


Figure 3-44. Change in resistivity with respect to the time the temperature sweep stopped ($V = 1\text{V}$, a -axis).

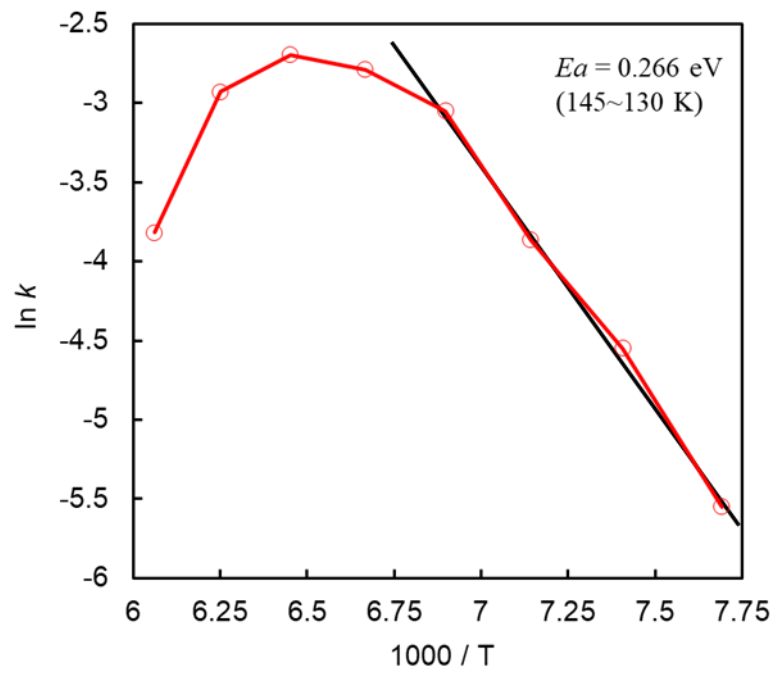


Figure 3-45. Arrhenius plot of the phase transition rate.

Based on the energy diagram in Fig. 3-46, in state I, the difference in the free energies between the two phases (ΔG) is large, and the frequency of transition from LTP to HTP is lower than that in transition from HTP to LTP, and it becomes more remarkable as the temperature decreases. Therefore, since the rate of phase transition from HTP to LTP is mainly governed by the activation energy, the lower the temperature, the slower the phase transition rate. In state II near the phase transition temperature, ΔG is small and the transition from LTP to the intermediate state occurs in the same way as the transition from HTP to the intermediate state, so the phase transition rate becomes slower as the temperature approaches the phase transition temperature.

Since the distribution of charge density in the donor molecule also changes between the HTP and LTP, charge transfer is also required for the phase transition. In fact, the activation energy of the phase transition (0.266 eV) obtained from the time-dependent experiment is close to the activation energy of the charge transfer (0.24 to 0.29 eV in HT) obtained from the temperature dependence of the conductivity.

In addition, there are two types of directions in the structural phase transitions from HTP to LTP in the equivalent orthogonal axes, and the directions should be also affected by adjacent molecules. However, this point cannot be discussed in detail at this time, because theoretical calculations, including calculations on the effects of the surrounding multiple donor molecules, have not been investigated.

On the other hand, since all the phase transitions from LTP to HTP are changes to the same structure, it might be that a rapid phase transition takes place due to the cooperative motion between the molecules.

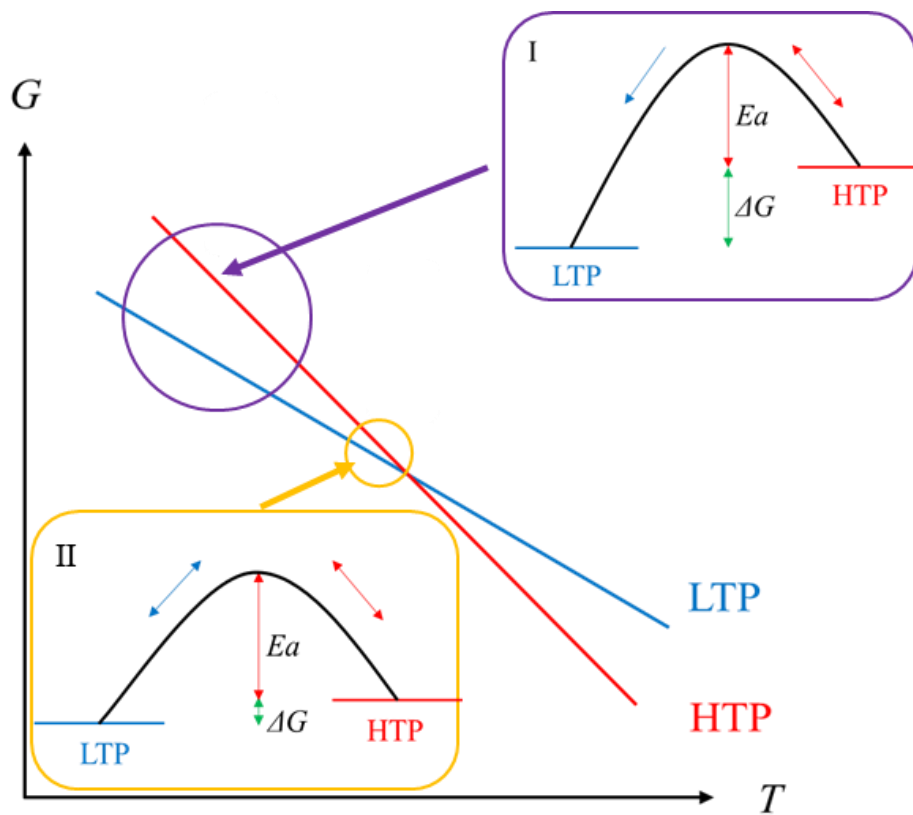


Figure 3-46. Energy diagram of $\text{TBC3} \cdot \text{Br} \cdot \text{TCE}_2$.

3-10. Current dependence of the structural phase transition rate

In addition to determining the activation energy of the phase transition in 3-8, time-course of resistance from HTP to LTP was measured at 160 K at each applied current value, as shown in Fig. 3-47. The results showed that, the larger the current value, the faster the phase transition rate and the larger the resistance change. From this, it is considered that the phase transition is enhanced by the applied electric current.

From the temperature dependence of the phase transition rate, it is known that the phase transition rate is highest between 150 K and 155 K, and at 160 K, where the current dependence is measured, the phase transition becomes slower when the temperature rises due to the exothermic effect of the current. Therefore, with the contribution of Joule heat, the phase transition rate should be slower. This, in turn, means that the current dependence of the phase transition rate would be the effect of carrier injection similar to the current dependence of phase transition in TTF-TCNQ discussed in Chapter 2.

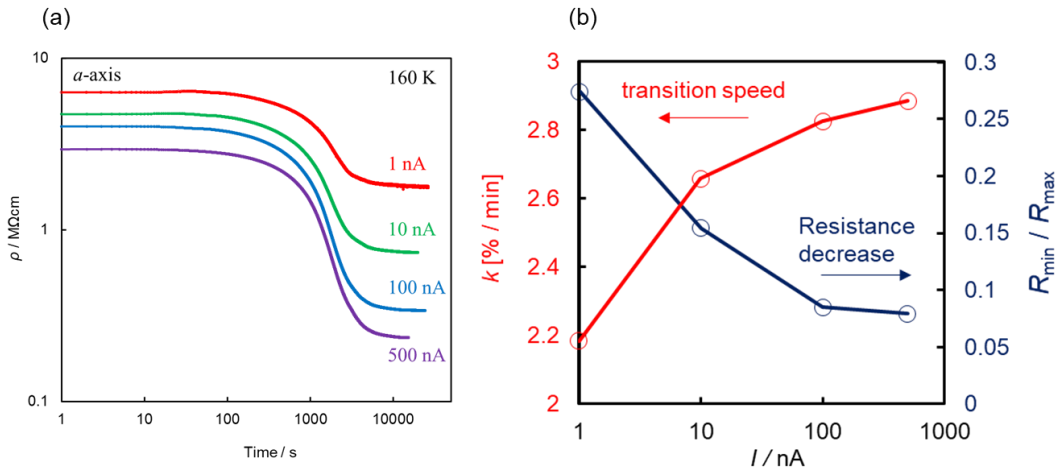


Figure 3-47. (a) Resistance change with time during each current application. (b) Current dependence of the phase transition rate.

The activation energy of the phase transition obtained from the temperature dependence of the phase transition rate was 0.266 eV, and this value is close to the activation energy for the conductivity (0.24 to 0.29 eV in HTP), which was obtained from the temperature dependence of the resistance. Since the phase transition also requires the charge transfer, there would be some correlation. As depicted in Figure 3-48, the current flow, which is regarded as the successive intermolecular charge transfer process, takes place via the intermediate state having the different charge configuration. If this intermediate charge state is stabilized, the structure will fall down to the LTP structure. Therefore, increasing current increases the frequency of mutual conversion between the charge configuration states, and accelerates the phase transition rate as a direct electronic effect. This mechanism is basically the same as the mechanism of NDR in the HTP. Since the intermolecular interaction and the resulted conductivity is not high, the thermally activation-type conducting behavior appears in this system (**TBC3·Br·TCE₂**). It could be also explained in terms of the magnetic susceptibility: the observed Curie constant of 0.375 corresponds to the one magnetic spin per one **TBC3·Br·TCE₂** unit (in the HTP) and this means that the cation-radicals on the molecules are distinguished from each other. Therefore, the charge has enough time to be stabilized in each electronic state also at the charge-transfer process as the part of current flow. In the HTP, the increase of the current causes the increase of the conductivity, accompanied with NDR, through the equalization of the charge disproportionation. In the super-cooled state from the HTP to the LTP, the increase of the current causes the acceleration of the phase-transition rate through the increase of the frequency of the mutual conversion between the electronic states. Thus, the mechanism of the above two characteristics in this system (**TBC3·Br·TCE₂**) are attributable to the same origin.

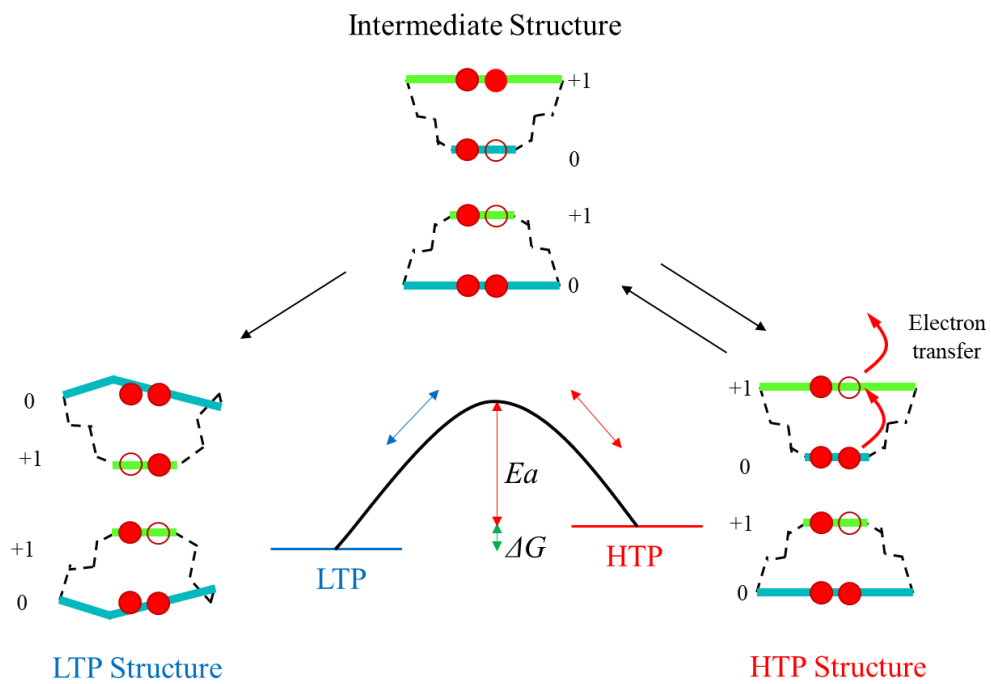


Figure 3-48. Schematic diagram of the electronic state during the phase transition from the HTP to the LTP.

3-11. Summary

The effect of applying current on the phase transition from a single crystal to a single crystal of $\text{TBC3}\cdot\text{Br}\cdot\text{TCE}_2$ was investigated. This phase transition was further investigated by crystal structure analysis, conductivity measurement, magnetic measurement, and theoretical calculation. This investigation uncovered an unintuitive phenomenon—namely, the phase transition from HTP to LTP was accelerated by the applied current. In addition, by analyzing changes in the bond lengths of donor molecules and performing theoretical calculations based on their structures, we succeeded in clarifying changes in the charge distribution and consistently explaining changes in the conductive properties and magnetism. From the temperature dependence of conductivity, it was clarified that the activation energy is unequal on the a and b axes depending on the molecular structure. Moreover, by measuring the frequency dependence of the AC impedance and extracting components that depend on the dynamics of molecular motion, the relationship with changes in the conformational patterns of solvent molecules and alkyl chains before and after the phase transition was clarified.

Chapter 4

Orthogonal path-type conductive switching of TBC3•Br•TCE₂

4-1. Introduction

In the sophisticated electronic circuits currently in practical use, electronic devices for controlling the current flow are considered standard and indispensable. For example, rectifiers and transistors^{67,68} can regulate the direction of the current and the value of the current, respectively. Both these devices are also essential for organic electronics and are still being widely developed. In contrast, organic electronics are basically modeled on silicon-based electronic devices, and their characteristic advantages are mainly limited to lightness and printability. However, there are a wide variety of molecules that could potentially be applied to circuits, and various categories of device functions should be achievable by using the novel operation mechanisms derived from the special features of different molecules. In this study, we developed a novel device function in a molecular crystal based on a special feature of its constituent molecules. In the crystal, the resistivities of two orthogonal crystal axes are related to each other, and the high resistivity and low resistivity states can be mutually exchanged by repeatedly applying current along the selected direction.

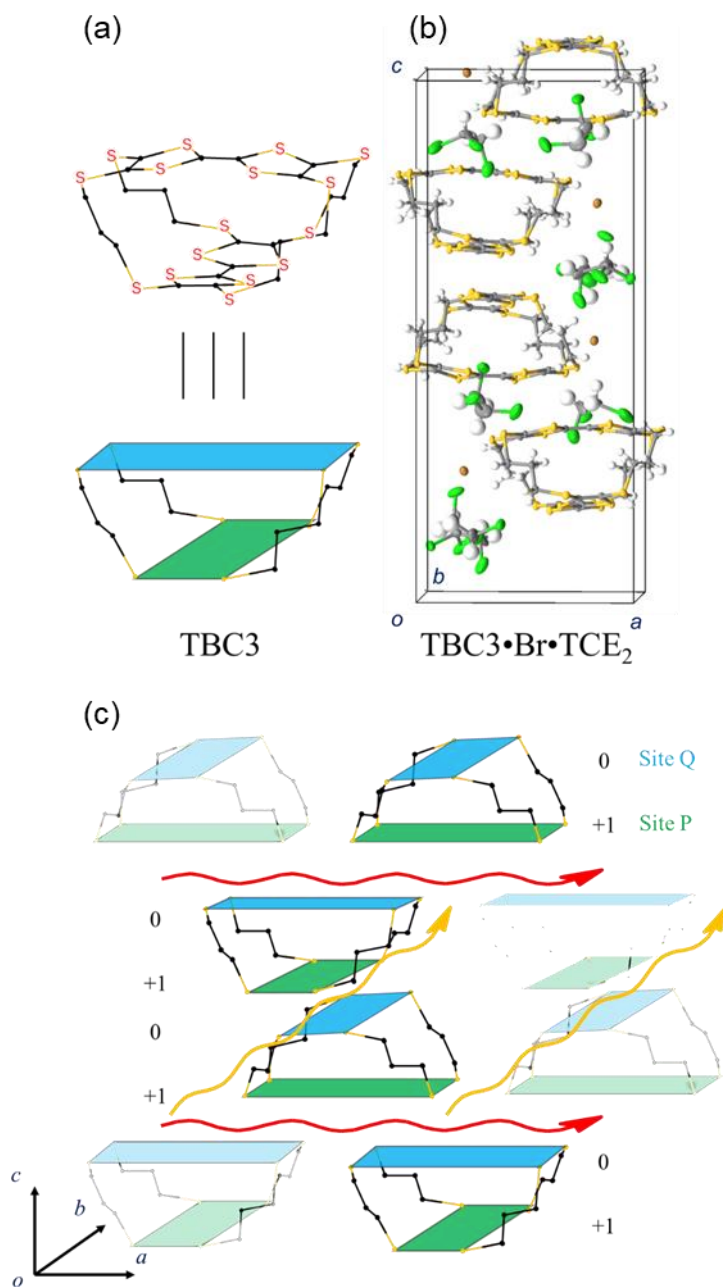


Figure 4-1. (a) Molecular structure of **TBC3**. The crystal structure (b) and its pattern diagram (c) of ion-radical salt **TBC3·Br·TCE₂** are also shown.

In Chapter 3, the donor molecule **TBC3** and its ion-radical salt, **TBC3•Br•TCE₂**, were investigated in detail and the following characteristics were found. In cyclophan donor TBC3, two tetrathiafulvalene (TTF) units are arranged orthogonally to each other by four trimethylenjithio chains, which gives a great degree of freedom in the molecular structure (Fig. 4-1a). In the **TBC3•Br•TCE₂** crystal, molecules stack together by rotating 90 degrees to form a spiral structure to face TTF units in parallel between the neighboring molecules along the *c*-axis, as shown in Fig. 4-1(b), (c). This ion-radical salt shows a single-crystal to single-crystal structural phase transition in which one of the two TTF skeletons is deformed from a planar structure at room temperature to a bent structure at 170 K or below, as a result of the large degree of freedom of the **TBC3** molecule. In this phase transition, the *Tetragonal P4₁* space group in the high temperature phase (HTP) turned out to be *Monoclinic P2₁* in the low temperature phase (LTP). Their physical properties also change upon the phase transition: in LTP, the resistance becomes 1/10 and the magnetic susceptibility becomes *ca.* 1/2 compared with those in HTP.

In this chapter, the interconversion of the molecular structure and resistivity of **TBC3•Br•TCE₂** along the non-equivalent orthogonal crystal axes by applying a large current was demonstrated, focusing on the fact that the orthogonal equivalent axes in HTP of this crystal become non-equivalent in LTP through phase transition. Since the *a* and *b* axes are equivalent in HTP, distortion upon the phase transition for LTP can take place along either axis by chance. For this reason, the LTP crystal has a mosaic pattern consisting of domains for which the directions of the distorted axes are different. The above situation is treated as a “merohedral twin” in X-ray crystal structure analysis, and the two domains are determined to exist in a *ca.* 2:1 ratio in this crystal. Moreover, the electric conductivity through the two directions in LTP is expected to have relatively large

(1-order of magnitude) anisotropy. In other words, this LTP crystal has bistability on the molecular distortion axis. We tried to control the anisotropy of the structural distortion on the molecules caused by the phase transition and to convert the structure and conductivity between the two orthogonal crystal axes.

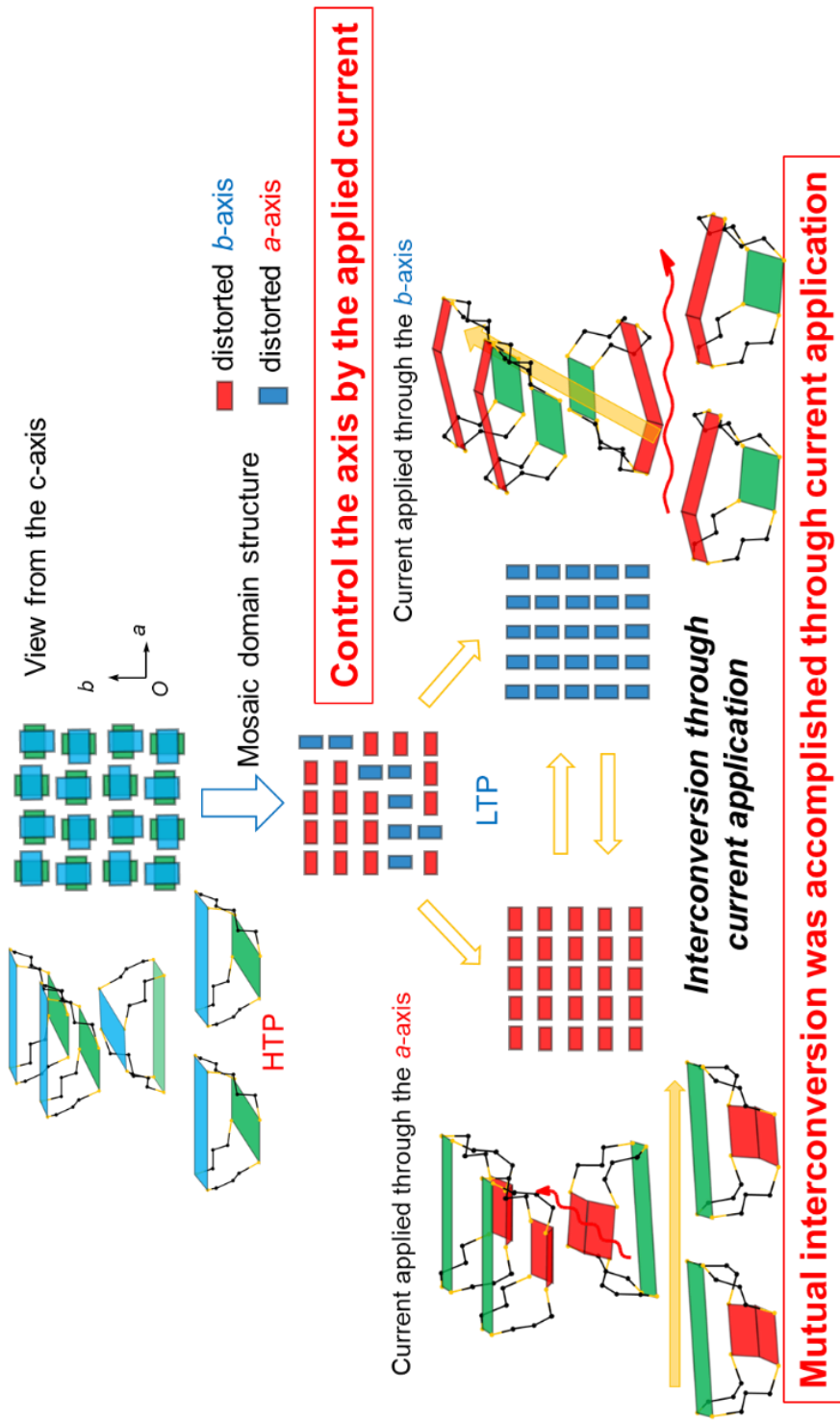


Figure 4-2. Schematic diagram of Structural and physical-property modifications induced by current application.

4-2. Crystal preparation and fabrication of measurement devices

Ion-radical salt $\text{TBC3}\cdot\text{Br}\cdot\text{TCE}_2$ was prepared by electro-crystallization of TBC3 in the presence of tetrabutylammonium bromide ($\text{TBA}\cdot\text{Br}$) in 1,1,2-trichloroethane (TCE , incorporated in the crystal as the crystal solvent) solution in a H-shaped electrolysis cell. The obtained crystal has bipyramidal shape: the equatorial plane is the a - b plane whereas the axial direction corresponds to the c -axis. Then, a thin, square-shaped crystal piece was cut out by slicing the obtained crystal parallel to the a - b plane. Gold wires were attached at the four edges of the square-shaped crystal along the measurement axes (a and b axes) using gold paste.

Measurement instruments

DC conductivity measurements including current sweep (V - I) measurements and mutual switching measurements were carried out using an R6245 2-channel source meter (Advantest Inc.). A Keithley 7001 switch system with a 7011-s multiplexer card was used to connect electrodes to the ground in the mutual switching measurements. AC-DC simultaneous measurements were carried out using an R6245 2-channel source meter and NF5640 2-phase digital lock-in amplifier (NF Electronics Inc.). The sample was placed in a cryostat (Quantum Design PPMS), with a standard sample pack for conductivity measurements.

4-3. Mutual conversion of conductivity along the orthogonal axes of TBC3•Br•TCE₂

The temperature dependence of the resistance along the *a*-axis is shown in Fig. 4-3. As the temperature decreased gradually, the resistance of the crystal increased and then sharply decreased around 160 K, as it transitioned from HTP to LTP. Then, as the temperature increased, a sudden phase transition took place from LTP to the HTP around 175 K. A clear hysteresis was observed between the cooling and heating processes, and the resistance in LTP was about one tenth of that in HTP, as reported previously.^{37,38} In this phase transition, the activation energy in HTP of 0.24 eV for both the *a* and *b* axes is dependent on the equivalent of the crystal axes (in the *Tetragonal P4*₁ space group), which turned out to be non-equivalent for the corresponding crystal axes (0.18 and 0.21 eV) in LTP (Ref: along the *c*-axis, 0.26 eV in HTP and 0.20eV in LTP). This result suggests that the structural anisotropy in LTP also affects the conductivities of the crystal along the orthogonal axes, which were equivalent in HTP.

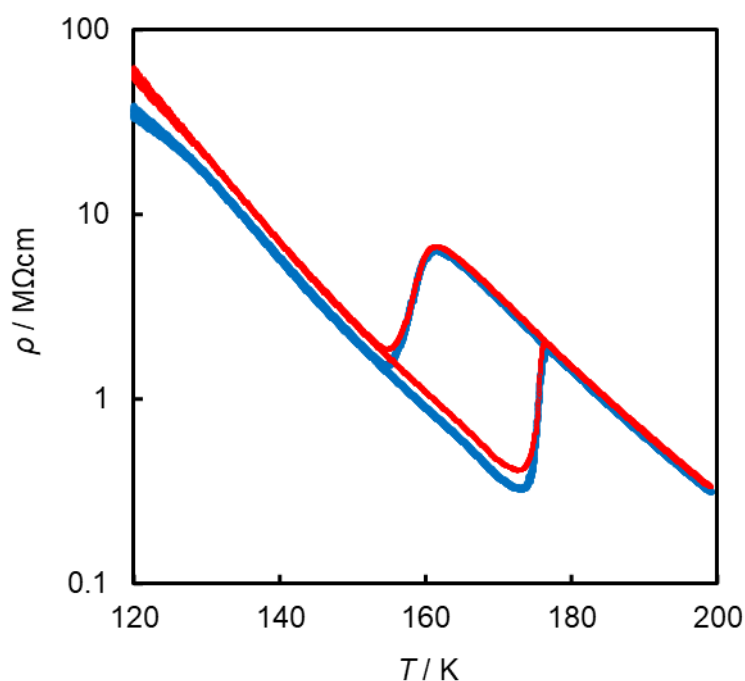


Figure 4-3. Temperature dependence of the resistivity of the **TBC3•Br•TCE₂** crystal. The red line is the *a*-axis, and the blue line is the *b*-axis. The sweep rate is 0.1 K/min.

Figure 4-4 shows the cyclic *V-I* characteristics of **TBC3•Br•TCE₂** along the *a* (and *b*) axis at 160 K (LTP). In this crystal, a negative differential resistance (NDR) was observed in which the voltage had a negative slope with respect to the current. In addition, by repeating the *V-I* cycle, a clear hysteresis loop and a gradual decrease of maximum voltage were observed. On the other hand, the value for the decrease of the maximum voltage gradually decreased as the *V-I* cycled and the maximum voltage approached a certain value (Fig. 4-4c). These results suggest that the resistance was reduced by the application of current during the current sweeping process but it was maintained to some degree even after the current application. This phenomenon could be explained in terms of the mosaic structure of the LTP crystal: The domain of higher

resistivity for the current applied direction, which is perpendicular to the lower resistivity axis, could be aligned to the lower resistivity direction by current application even in LTP (Fig. 4-4d).

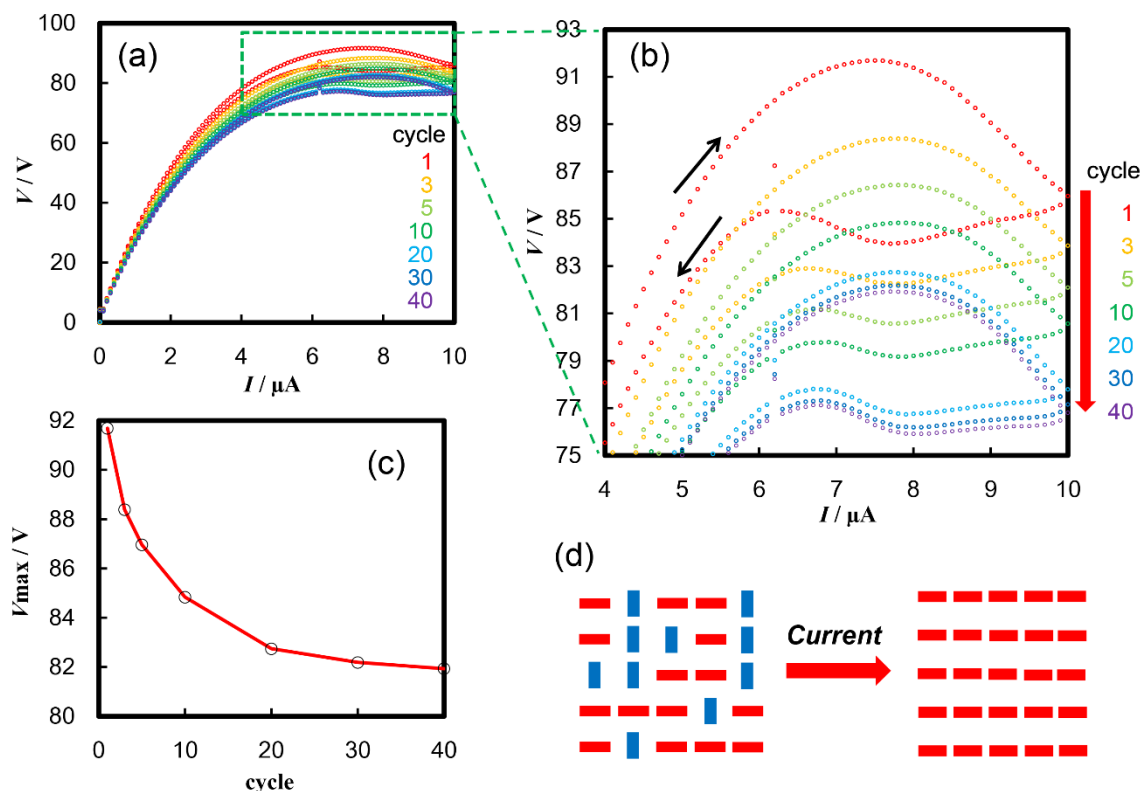
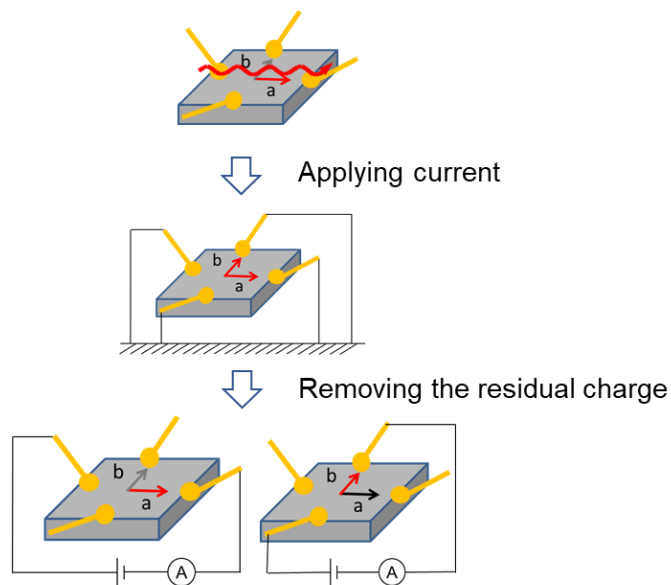


Figure 4-4. (a) Voltage-current (V - I) characteristics of $\text{TBC3}\cdot\text{Br}\cdot\text{TCE}_2$ at 160 K (LTP). (b) Expanded view of the V - I characteristics around the voltage peak. (c) The change of the peak voltage by the V - I cycle. (d) Pattern diagram modeling a plausible mechanism of the hysteretic V - I characteristics of $\text{TBC3}\cdot\text{Br}\cdot\text{TCE}_2$. The anisotropic structure of the LTP molecule is represented as a rectangle, with the long direction corresponding to the low resistance axis and the short direction corresponding to the high resistance axis.

Since the axis of molecular distortion in LTP could be aligned by applying current in one axis of the originally equivalent axes in HTP, the same phenomenon could be expected for the other axis. Therefore, the mutual resistivity switching along the orthogonal directions (in the a and b axes) was investigated as follows. As shown in Figure 4-5, a large current was applied by performing V - I measurement in one direction (a or b axis) on the crystal at 160 K (LTP). After removing the residual charge by connecting and disconnecting all terminals to the ground, the resistances of the a and b axes were alternately measured at a low constant voltage (100 mV). This operation was repeated by changing the directions for the large-current application. Figure 4-6 shows the results of resistance change caused by the current application. After applying a large current to the b -axis, the resistance along the b -axis decreased while the resistance along the a -axis increased. Next, after applying a large current to the a -axis, the resistance along the a -axis decreased while the resistance along the b -axis increased. In this way, mutual conversion of resistance was repeated in the same manner, with the resistance of the current-applied axis decreasing and that of the other axis increasing. A mutual conversion of the conductivity was realized with a resistance change of up to 14%.



The resistances of the *a* and *b* axes were alternately measured at a low constant voltage

Figure 4-5. Schematic diagram of the measurement.

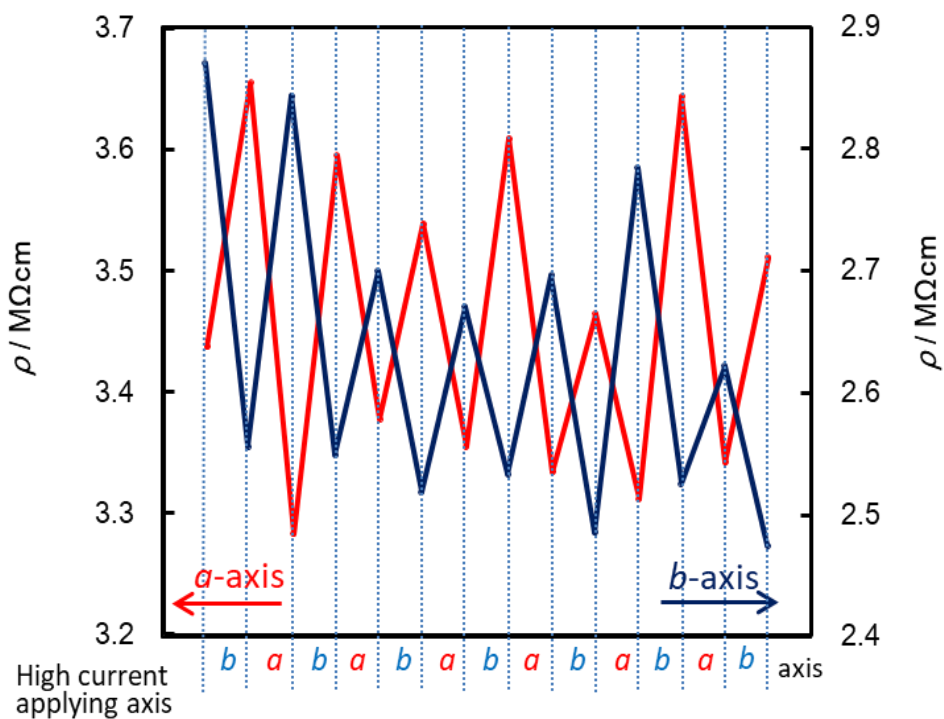


Figure 4-6. Mutual changes in the resistance of $\text{TBC3}\cdot\text{Br}\cdot(\text{TCE})_2$. The red line is the *a*-axis, and the blue line is the *b*-axis.

4-4. Simultaneous measurement of conductivity in the orthogonal axis direction of $\text{TBC3}\cdot\text{Br}\cdot\text{TCE}_2$

In the above mutual resistivity exchange experiment, the resistivity change could only be detected after the large-current application, especially for the non-current applied axis. To determine the resistivity change during the large-current application in both axes, AC conductivity was measured along one axis while direct current was applied along the other orthogonal axis. AC voltage was applied through two coupling capacitors to cut the DC current (Fig. 4-7). The resistance changes on both axes were plotted against the applied current as shown in Fig. 4-8.

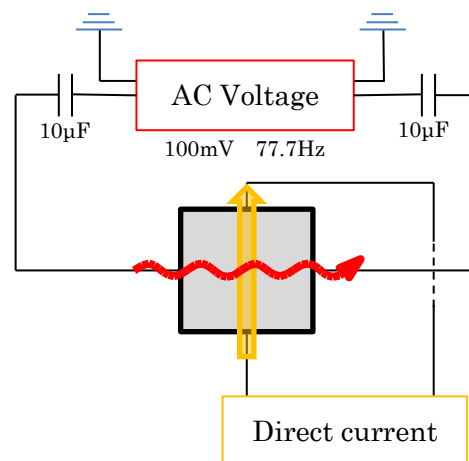


Figure. 4-7. Schematic diagram of the measurement circuit.

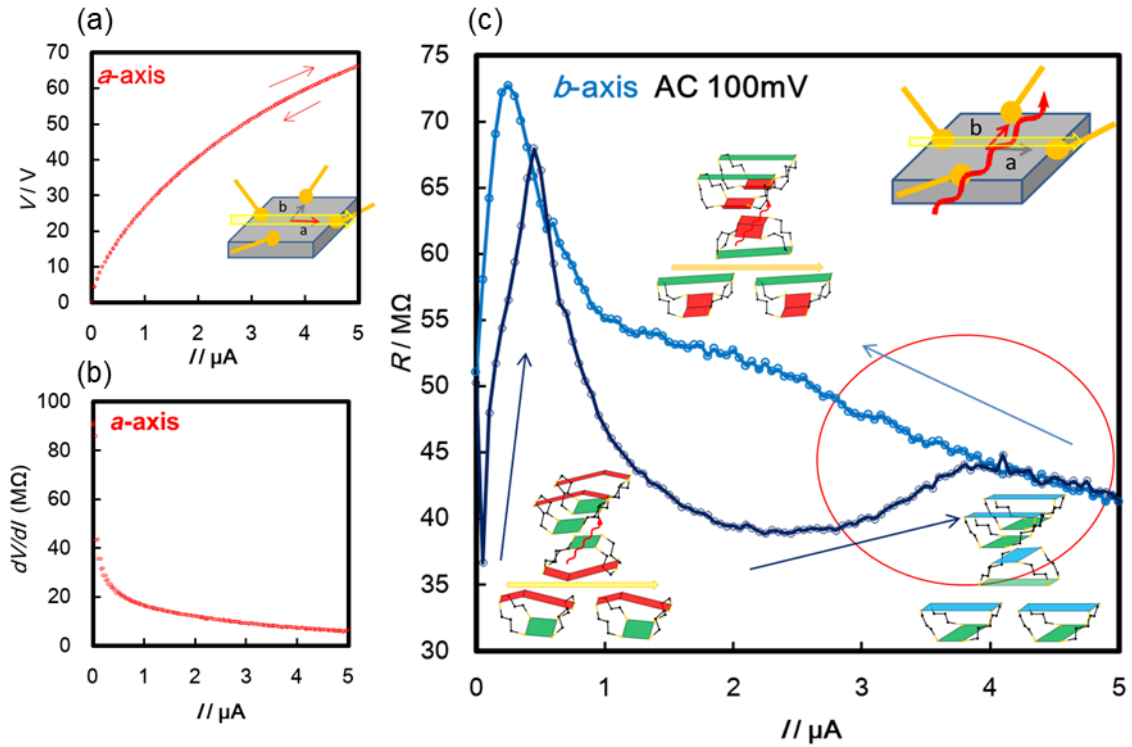


Figure 4-8. (a) Voltage(*a*-axis) - applied current(*a*-axis) plot, (b) differential resistance(*a*-axis) - applied current(*a*-axis) plot, (c) resistance(*b*-axis) - applied current(*a*-axis) plot.

Figure 4-8 shows the results for the LTP crystal at 165 K. The DC current was swept up to 5 μA along the *a*-axis, and the constant AC voltage of 100 mV was simultaneously applied along the *b*-axis. As a result, the resistance changes along the *b*-axis had a complex structure in response to the application of the current along the *a*-axis, whereas a monotonous decrease of the resistance was observed along the *a*-axis. As the current along the *a*-axis was increased, the resistance along the *b*-axis increased rapidly in the low current region up to 0.5 μA , decreased to 2 μA , increased again to ca. 4 μA , and finally decreased to a higher current region. On the other hand, the resistance increased monotonously in the current-decreasing process, except in the low current region, and the highest resistance was higher than that in the current-increasing process. The rapid change

of the resistivity along the b -axis in the low-current region would be due to the suppression of dielectric response by the DC electric field resulting from the applied direct current. Obvious hysteretic behavior was observed in the current-increasing and -decreasing processes. Similar behavior was observed in the other temperatures below 165 K, which belonged to the LTP. On the other hand, the hysteresis became very small above 180 K, which belonged to the HTP. These results could be explained in terms of the local phase transition from LTP to HTP.

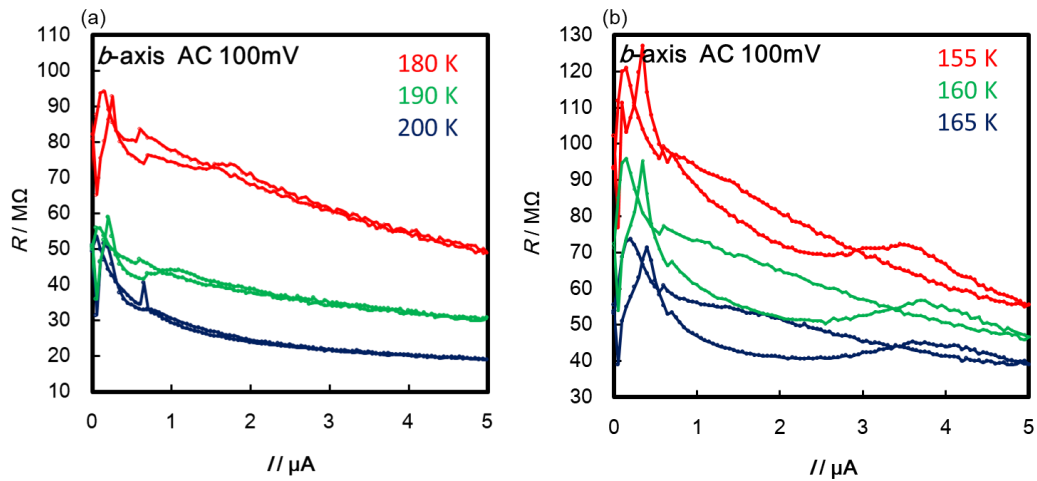


Figure 4-9. Resistance(b -axis) - applied current(a -axis) plot at 180-200 K in the HTP (a) and at 155-165 K in the LTP (b).

4-5. Mechanism of conductivity switching in $\text{TBC3}\cdot\text{Br}\cdot\text{TCE}_2$

In LTP of the $\text{TBC3}\cdot\text{Br}\cdot\text{TCE}_2$ crystal, domains having different molecular distortion axes along either the a - or the b -axis were formed. When a current was applied along the a -axis, the domain in which the molecule distorted along the a -axis had a higher resistance. Therefore, this domain would take a larger voltage through the current application, and the local temperature would be increased by the Joule heat, and the domain would thereby transition to HTP. If the molecular distortion axis of the domain becomes the b -axis as the domain returns to LTP after removing the current, the domain will no longer absorb large Joule heat in the next current-increasing cycle, because it is in the low-resistance direction. By repeating the above cycle, the entire route will gradually change to a low-resistance direction.

Furthermore, in the LTP of $\text{TBC3}\cdot\text{Br}\cdot\text{TCE}_2$ crystal, two types of domains with different crystal axis orientations are always adjacent within the ac plane (ab' plane, corresponds to the HTP). When two types of domains share a two-dimensional plane, the same type of domain is always separated by the other type of domain, and at the point where the domain boundaries intersect, the two types of domains form a bottleneck structure with each other, as shown in Figure 4-10. When considering the current path in each crystal axis direction in such a region, the resistance of this bottleneck portion is the largest in the entire path. Therefore, the resistance of the path is mainly determined at this portion, and the mutual switching of resistance also takes place effectively and efficiently.

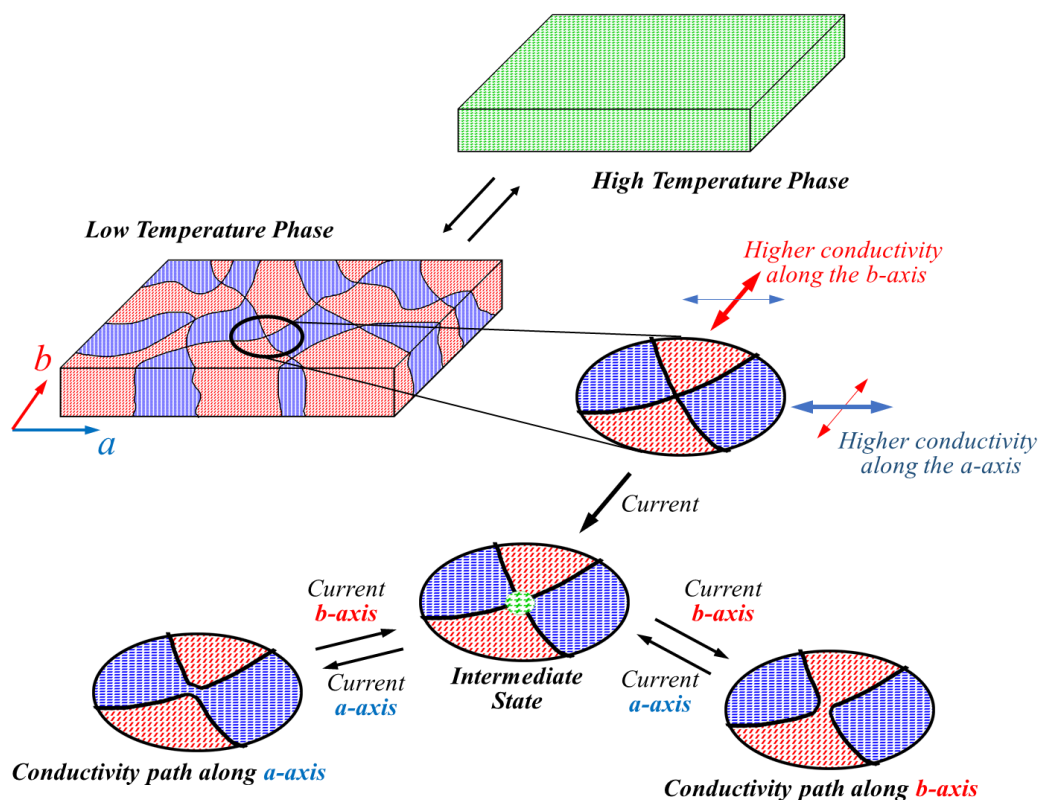


Figure 4-10. Formation of bottle-neck structure in the LTP of the $\text{TBC3}\cdot\text{Br}\cdot\text{TCE}_2$ crystal.

On the other hand, the above phenomenon would not be due merely to a simple heat effect, because the corresponding hysteretic behavior was not observed in the resistivity along the *a*-axis (current-applied axis). Rather, it would be explained in terms of the contribution of a direct electronic effect of the applied current as discussed in Chapter 3.

In the high-resistance bottleneck region between the low-resistance domains, donor moieties along the current path were almost neutral and had a bend structure, as shown in Figure 4-11. By applying current, the passing charges would change the donor structures to planar, and cause the donor structures of the perpendicular direction to bend through the structural constraint by the four trimethylene chains connecting two TTF units. These interesting properties arise from the characteristic molecular structure.

This mechanism is also supported in terms of the theoretical calculation that the conductivity along the orthogonal axes in LTP crystal has large anisotropy as described in Chapter 3. This mechanism could also be applicable for a crystal system showing phase transition with symmetry break down.

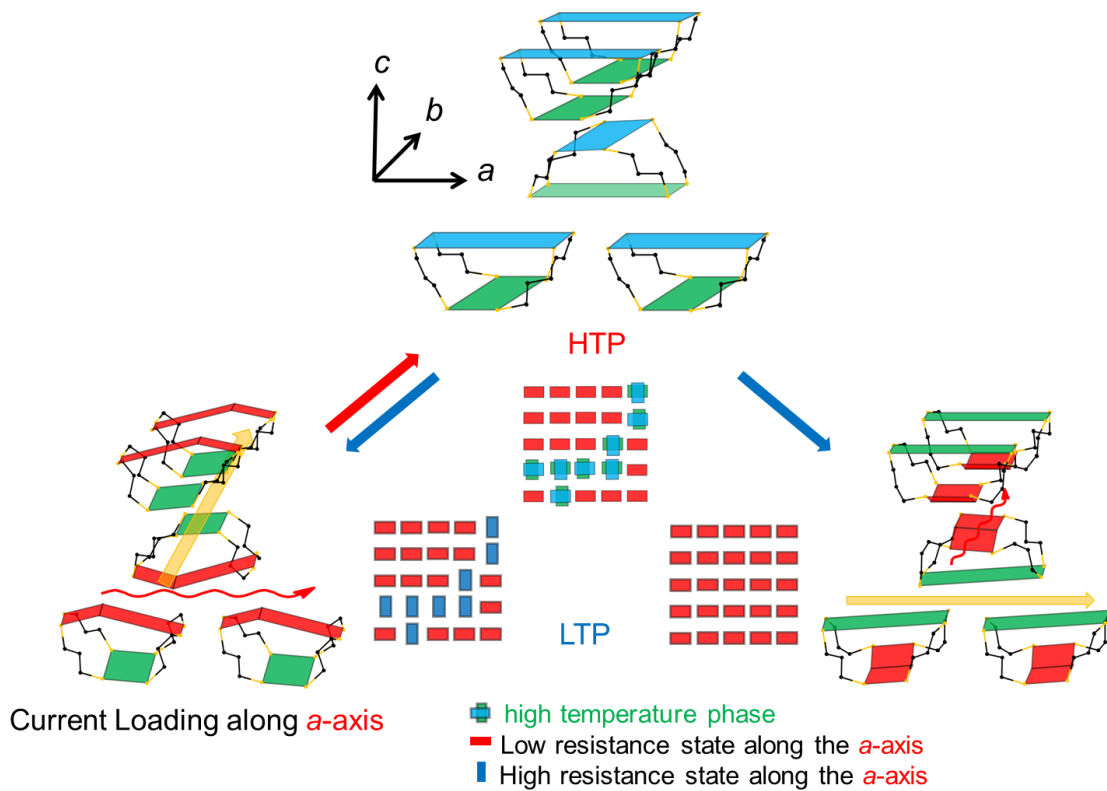


Figure 4-11. Mechanism of the mutual changes of the resistance.

Resistivity switching by constant current

To provide further evidence supporting the mechanism of mutual resistivity switching discussed in the main text, the applied current dependence of the phase transition was investigated on an LTP crystal at 160 K. When a low constant DC current (1 uA) was applied, the resistance remained largely unchanged for a long period of time, and the phase transition was not induced. When 13 uA was applied, the resistance became smaller. This could be attributed to the molecular distortion axes of the high-resistance domains changing to have lower resistance. On the other hand, when 20 uA was applied, the resistance increased monotonously. In this case, the whole crystal changed to the high-temperature phase without returning to the LTP by the too-high current value. These results suggest that there are optimum current values for the resistivity switching. However, precise control is required in order to find and set the optimum current values for resistivity switching. The values will vary depending on the individual crystal, and will be related to the balance of sufficient energy to increase the temperature of microscopic domain at the bottleneck site and the heat flow to remove extra heat to keep the temperature of the whole crystal below the transition temperature. The current sweep method (V - I measurement method), used in the main text, is good at supplying sufficient energy and appropriate cooling for mutual conversion.

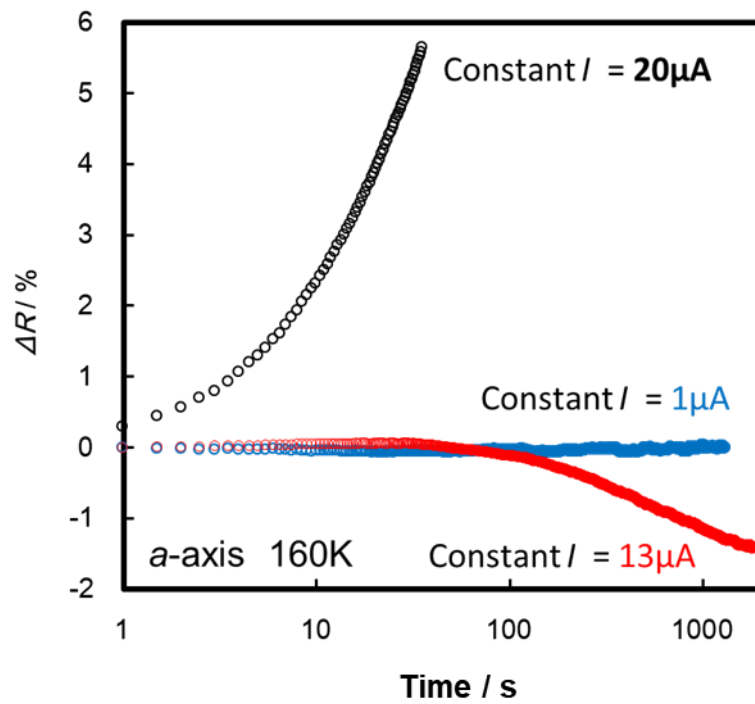


Figure 4-12. Resistivity change by constant current in the LTP (160 K).

4-6. Summary

In summary, the mutual switching of conductivity along orthogonal axes of a semiconducting organic crystal by repeated applications of loading current was investigated and demonstrated. The conductivity switching was attributable to the change of anisotropy of the crystal domains in a merohedral twin crystal as a low-symmetry low-temperature phase of a high-symmetry crystal. The AC-DC simultaneous resistance measurements along the orthogonal axes suggested that the loading current caused the microscopic phase transition to HTP having higher symmetry through the local heating by Joule heat, and then the domain structure settled to the lower resistance direction of the LTP structure.

The enhancement of the conductivity by the repeated stimulus and the resetting of the state by the stimulus from different directions resembles the function of a neural network, which is also interesting in terms of potential “deep-learning” applications. Whereas this experiment was carried out on a monolithic single crystal, the structural transformation takes place in each molecule, and the mutual switching of conductivity could be attributable to the small crystal domain. In this respect, this system could be regarded as a model of an “integrated molecular circuit.”

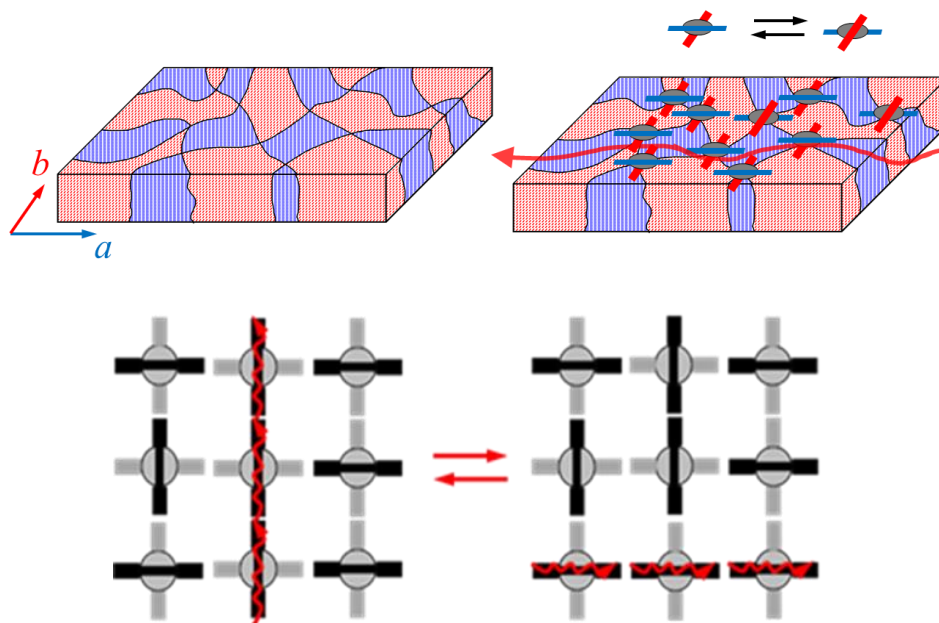


Figure 4-13. Schematic diagram of switching of an integrated circuit based on the domain structure in the LTP of the $\text{TBC3}\cdot\text{Br}\cdot\text{TCE}_2$ crystal.

Chapter 5

Conclusion

Structural phase transition of organic conductor crystals controlled by applied current were investigated during the course of this thesis. Negative differential resistance and current-induced phase transition were found and added as a new feature of **TTF-TCNQ**, the most famous and well investigated organic conductor. NDR was observed in the whole measured temperature range below 53 K, which corresponds to the Peierls transition temperature, whereas the structures in E - J curves including NDR depend on the three phases below 53, 49, and 38 K. Since the Peierls phase transition depends mainly on the strong correlations among electrons in the quasi-one-dimensional electronic structure, the electronic state would be quite sensitive for the charge carrier density regardless of the origin of the carrier, whether it is thermally excited or externally induced by the current application. The phase transition controlled by applied current, which was clarified in this study, is attracting attention as a method applicable to all organic substances having similar low-dimensional electronic structures.

The effect of applying current on the phase transition from single crystal to single crystal of **TBC3·Br·TCE₂** was investigated. This phase transition is further investigated by crystal structure analysis, conductivity measurement, magnetic measurement, and theoretical calculation. Through the investigation, an unintuitive phenomenon, that the phase transition from the high-temperature phase to the low-temperature phase was accelerated by the applied current. In addition, by analyzing changes in bond lengths of donor molecules and performing theoretical calculations based on their structures, we

have succeeded in clarifying changes in charge distribution and consistently explaining changes in conductive properties and magnetism. Furthermore, by measuring the frequency dependence of AC impedance and extracting components that depend on the dynamics of molecular motion, we clarified the relationship with changes in the conformational patterns of solvent molecules and alkyl chains before and after the phase transition.

We also investigated and demonstrated the mutual switching of conductivity along the orthogonal axes of **TBC3·Br·TCE₂** by repeatedly loading a current. We have developed a new device function with a new operating mechanism that is different from the conventional one, which increases the resistivity in one direction by applying current to the other direction mutually in one of the two intersecting current paths. The conductivity switching is attributable to the change in anisotropy of crystal domains in the merohedral twin as the low-symmetry low-temperature phase of the highly symmetric crystal. The AC-DC simultaneous resistance measurements along the orthogonal axes suggested that the loading current causes the microscopic phase transition to HTP having higher symmetry through the local heating by Joule heat and then the domain structure is settled to the lower resistance direction of LTP structure. This system can be thought of as a model of a molecule-based integrated circuit, as donor molecules in the crystal individually respond to external stimuli and express their function through intermolecular interactions.

The phase transition of a material is a fundamental physicochemical phenomenon, but research focusing on changes in the physical properties of organic crystals that can synthesize various analogs has attracted more attention in recent years, and the phase transition of crystals due to current has been attracting more attention. The system used

in this study resembles the functionality of neural networks⁶⁹ of interest from the perspective of "deep learning" applications, as it improves conductivity with repeated stimuli and resets states with stimuli from different directions. It is thought that the neural network function can be investigated in detail by performing multi-terminal measurement as shown in Figure 5-1. Also due to differences in crystal size, it will also have interested in the difference between the time scale of the reaction by the current application. Actually, as shown in Fig. 5-2, micrometer-level precision measurement under SEM chamber is under investigation. If this system also functions on a nanoscale, it can be expected to work as an unprecedented inter-element wiring as an element that can switch orthogonal conductive paths. On the other hand, various analogues of this salt were prepared with different counter ions and inclusion solvents, which are the constituent units of this crystal, and investigated their effects on the phase transition behavior. It has a great influence on changes in phase transition temperature and physical properties in the preliminary investigations as shown in Figure5-3, and detailed investigation in the future will deepen the understanding of the mechanism of phase transition, and it is expected that the guiding principles to construct similar soft crystals will be established.

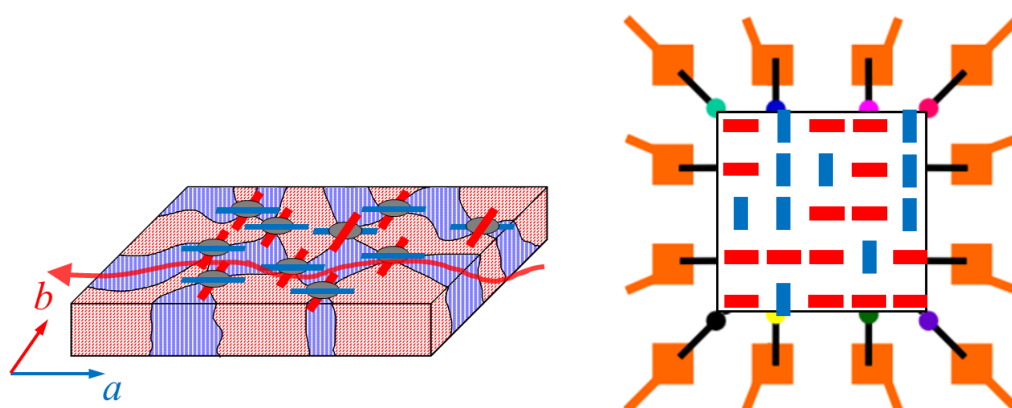


Figure5-1. Proposal for the multi-terminal measurement for crystals with randomly distributed domain structures.

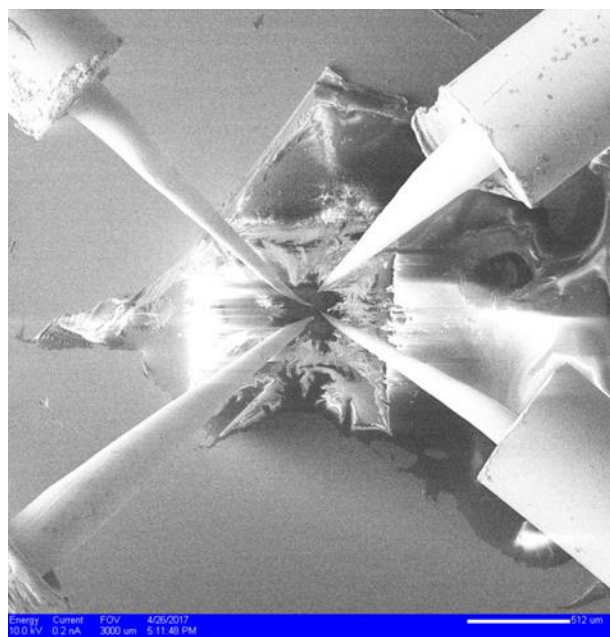


Figure5-2. 4 probe conductivity measurement under SEM observation.
Acknowledgement for Hasegawa Laboratory, University of Tokyo.

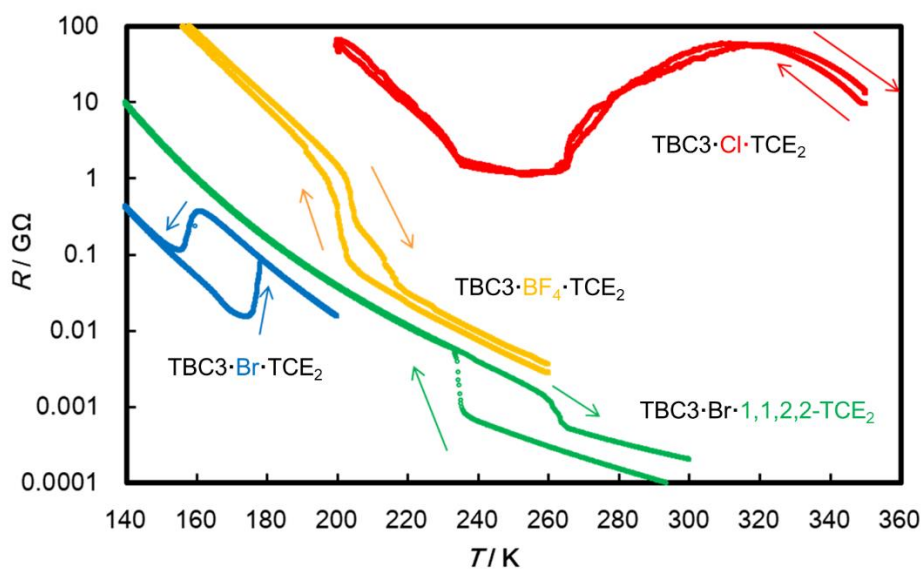


Figure5-3. Temperature dependence of resistivity in $\text{TBC3}\cdot\text{Br}\cdot\text{TCE}_2$, $\text{TBC3}\cdot\text{BF}_4\cdot\text{TCE}_2$, $\text{TBC3}\cdot\text{Cl}\cdot\text{TCE}_2$ and $\text{TBC3}\cdot\text{Br}\cdot 1,1,2,2\text{-TCE}_2$.

References

- [1] H. Akamatu, H. Inokuchi and Y. Matsunaga, *Nature* **173**, 168 (1954).
- [2] A. F. Gareito, A. J. Heeger, *Acc. Chem. Res.*, **7**, 232-249 (1974).
- [3] J. B. Torrance, *Acc. Chem. Res.*, **12**, 79-86 (1979).
- [4] G. Saito, Y. Yoshida, *Bull. Chem. Soc. Jap.*, **80**, 1-137 (2007).
- [5] D. S. Acker, R. J. Harder, W. R. Hertler, W. Mahler, L. R. Melby, R. E. Benson, and W. E. Mochel, *J. Am. Chem. Soc.*, **82**, 24, 6408–6409 (1960).
- [6] D. L. Coffen, J. Q. Chambers, D. R. Williams, P. E. Garrett, and N. D. Canfield *J. Am. Chem. Soc.*, **93**, 9, 2258–2268 (1971).
- [7] J. Ferraris, D. O. Cowan, V. V. Walatka, and J. H. Perlstein, *J. Am. Chem. Soc.*, **95**, 948 (1973).
- [8] H. Shirakawa, E. J. Louis, A. G. MacDiamid, C. K. Chiang and A. J. Heeger, *J. Chem. Soc., Chem. Commun.*, 578 (1977).
- [9] D. Jérôme, A. Mazaud, M. Ribault and K. Bechgaard, *J. Physique Lett.*, **41**, 95-98 (1980).
- [10] N. Thorup, G. Rindorf, H. Soling and K. Bechgaard, *Acta Cryst.*, **B37**, 1236-1240 (1981).
- [11] D. Jerome, A. Mazaud, M. Toriumi and H. Inokuchi, *Solid State Commun.*, **42**, 557-560 (1982).
- [12] H. Kobayashi, R. Kato, A. Kobayashi, S. Moriyama, Y. Nishio, K. Kajita and W. Sasaki, *Mol. Cryst. Liq. Cryst.*, **107**, 33 (1984).
- [13] C. M. Varma, J. Zaanen and K. Raghavachari, *Science*, **254**, 5034, 989-992 (1991)
- [14] G. Horowitz, *Adv. Mater.*, **10**, 365-377 (1998) .

- [15] J. Zaumseil, H. Sirringhaus, *Chem. Rev.*, **107**, 1296-1323 (2007) .
- [16] P. Abhishek, C. J. Kulkaerni, A. B. Tonozola and A. J. Samson, *Chem. Mater.*, **16**, 4556-4573 (2004).
- [17] H. Hoppe, N. S. Sariciftci, *J. Mater. Res.*, **19**, 1924-1945 (2004).
- [18] J. E. Anthony, *Chem. Rev.*, **106**, 5028-5048 (2006).
- [19] R. C. Benson, R. C. Hoffman, R. S. Potember, E. Bourkoffand, and T. O. Poehler, *Appl. Phys. Lett.*, **42**, 855 (1983).
- [20] F. O. Karutz, J. U. von Schutz, H. Wachteland and H. C. Wolf, *Phys. Rev. Lett.*, **81**, 140 (1998).
- [21] S. Koshihara, Y. Tokura, T. Mitani, G. Saito and T. Koda, *Phys. Rev. B*, **42**, 6853 (1990).
- [22] H. Kishida, T. Ito, A. Ito and A. Nakamura, *Applied Physics Express*, **4**, 3, 031601/1-031601/3, (2011).
- [23] Y. Kawasugi, H. M. Yamamoto, M. Hosoda, N. Tajima, T. Fukunaga, K. Tsukagoshi, and R. Kato, *Appl. Phys. Lett.*, **92**, 243508/1-243508/3 (2008).
- [24] M. Kato, H. Ito, M. Hasegawa, and K. Ishii, *Chem. Eur. J.*, **25**, 5105 –5112 (2019).
- [25] G. Gliemann, H. Yersin, *Struct. Bonding*, **62**, 87–153 (1985).
- [26] V. W. Yam, V. K. Au and S. Y. Leung, *Chem. Rev.*, **115**, 7589–7728 (2015).
- [27] T. Ogoshi, Y. Shimada, Y. Sakata, S. Akine and T. A. Yamagishi, *J. Am. Chem. Soc.*, **139**, 5664–5667 (2017).
- [28] S. Takamizawa, Y. Miyamoto, *Angew. Chem. Int. Ed.*, **53**, 6970–6973 (2014).
- [29] S. Takamizawa, Y. Takasaki, *Chem. Sci.*, **7**, 1527–1534 (2016).
- [30] F. Sawano, I. Terasaki, H. Mori, T. Mori, M. Watanabe, N. Ikeda, Y. Nogami and Y. Noda, *Nature*, **437**, 7058, 522-524 (2005).

- [31] M. A. Reed, C. Zhou, C. J. Muller, T. P. Burgin and J. M. Tour, *Science*, **278**, 252 (1997).
- [32] B. Xu, N. J. Tao, *Science*, **301**, 1221 (2003).
- [33] E. C. P. Smits, S. G. J. Mathijssen, P. A. van Hal, S. Setayesh, T. C. T. Geuns, K. A. H. A. Mutsaers, E. Cantatore, H. J. Wondergem, O. Werzer, R. Resel, M. Kemerink, S. Kirchmeyer, A. M. Muzafarov, S. A. Ponomarenko, B. de Boer, P. W. M. Blom and D. M. de Leeuw, *Nature*, **455**, 7215, 956-959 (2008).
- [34] H. Hasegawa, T. Kubota, S. Mashiko, *Thin Solid Films*, **352**, 438-439 (2003).
- [35] D. Tonouchi, M. M. Matsushita, and K. Awaga, *Phys. Rev. B*, **96**, 045116 (2017).
- [36] J. Tanabe, G. Ono, A. Izuoka, T. Sugawara, T. Kudo and T. Saito, *Mol. Cryst. Liq. Cryst.*, **296**, 61-76 (1997).
- [37] J. Tanabe, T. Kudo, M. Okamoto, Y. Kawada, G. Ono, A. Izuoka and T. Sugawara, *Chemistry Letters*, **24**, 7, 579-580 (1995).
- [38] K. Takimiya, Y. Shibata, K. Imamura, A. Kashihara, Y. Aso, T. Otsubo and F. Ogura, *Tetrahedron Letters*, **36**, 28, 5045–5048 (1995).
- [39] B. Mukherjee and M. Mukherjee, *Langmuir*, **27**, 11246 (2011).
- [40] C. K. Chiang, M. J. Cohen, P. R. Newman, and A. J. Heeger, *Phys. Rev. B*, **16**, 5163 (1977).
- [41] Y. Tomkiewicz, R. A. Craven, T. D. Schultz, E. M. Engler, and A. R. Taranko, *Phys. Rev. B*, **15**, 3643 (1977).
- [42] K. Saito, Y. Yamamura, H. Akutsu, M. Takeda, H. Asaoka, H. Nishikawa, I. Ikemoto, and M. Sorai, *J. Phys. Soc. Jpn.*, **68**, 1277 (1999).
- [43] M. J. Cohen, P. R. Newman, and A. J. Heeger, *Phys. Rev. Lett.*, **37**, 1500 (1976).
- [44] M. J. Cohen and A. J. Heeger, *Phys. Rev. B*, **16**, 688 (1977).

- [45] L. Liu and W. Leung, *Phys. Rev. Lett.*, **33**, 1145 (1975).
- [46] Z. Ji, C. Yang, K. Liu, and Z. Ye, *J. Cryst. Growth*, **253**, 239 (2003).
- [47] R. S. Potember, T. O. Poehler, and D. O. Cowan, *Appl. Phys. Lett.*, **34**, 405 (1979).
- [48] Y. Tokura, H. Okamoto, T. Koda, T. Mitani, and G. Saito, *Phys. Rev. B*, **38**, 2215 (1988). [49] R. Kumai, Y. Okimoto, and Y. Tokura, *Science*, **284**, 1645 (1999).
- [50] M. M. Matsushita and T. Sugawara, *J. Am. Chem. Soc.*, **127**, 12450 (2005).
- [51] S. Shin and K. R. Kim, *Jpn. J. Appl. Phys.*, **54**, 06FG07 (2015).
- [52] J. Shim, S. Oh, D. Kang, S. Jo, M. H. Ali, W. Choi, K. Heo, J. Jeon, S. Lee, M. Kim, Y. J. Song, and J. Park, *Nat. Commun.*, **7**, 13413 (2016).
- [53] Marshall. J. Cohen, P. R. Newman, and A. J. Heeger, *Phys. Rev. Lett.*, **37**, 1500 (1976).
- [54] J. R. Cooper, J. Lukatela, M. Miljak, J. M. Fabre, L. Giral, and E. Aharon-Shalom, *Solid State Commun.*, **25**, 949 (1978).
- [55] S. Kagoshima, T. Ishiguro, and H. Anzai, *J. Phys. Soc. Jpn.*, **41**, 2061 (1976).
- [56] K. Awaga, K. Nomura, H. Kishida, W. Fujita, H. Yoshikawa, M. M. Matsushita, L. Hu, Y. Shuku, and R. Suizu, *Bull. Chem. Soc. Jpn.*, **87**, 234 (2014).
- [57] K. Okamoto, T. Tanaka, W. Fujita, K. Awaga, and T. Inabe, *Phys. Rev. B*, **76**, 075328 (2007).
- [58] R. C. Lacoë, H. J. Schulz, D. Jerome, K. Bechgaard, and I. Johannsen, *Phys. Rev. Lett.*, **55**, 2351 (1985).
- [59] R. C. Lacoë, J. R. Cooper, D. Jerome, F. Creuzet, K. Bechgaard, and I. Johannsen, *Phys. Rev. Lett.*, **58**, 262 (1987).
- [60] W. Wonneberger and F. Gleisberg, *Solid State Commun.*, **23**, 665 (1977).
- [61] K. Takimiya, Y. Shibata, K. Imamura, A. Kashihara, Y. Aso, T. Otsubo, F. Ogura, *Tetrahedron Letters*, **36**(28) 5045–5048 (1995)

- [62] S. Triki, L. Ouahab, J. F. Halet, O. Pena, J. Padiou, D. Grandjean, C. Garrigou-Lagrange, P. Delhaes, *J. Chem. Soc. Dalton Trans.*, 1217–1227 (1992)
- [63] P. Guionneau, C. J. Kepert, G. Bravic, D. Chasseau, M. R. Truter, M. Kurmoo and P. Day, *Synth. Met.* 86, 1973 (1997).
- [64] U. Geiser, H. H. Wang, J. A. Schlueter, S. L. Hallenbeck, T. J. Allen, M. Y. Chen, H. C. I. Kao, K. D. Carlson, L. E. Gerdom and J. M. Williams, *Acta Cryst.*, **C44**, 1544 (1988).
- [65] T. Mallah, C. Hollis, S. Bott, M. Kurmoo, P. Day, M. Allan and R. H. Friend, *J. Chem. Soc. Dalton.*, **859** (1990).
- [66] P. Day, M. Kurmoo, T. Mallah, I. R. Marsden, R. H. Friend, F. L. Pratt, W. Hayes, D. Chasseau, J. Gaultier, C. Bravic and L. Ducasse, *J. Am. Chem. Soc.*, **114**, 10722 (1992).
- [67] G. H. Ibrahim, U. Zschieschang, H. Klauk and L. Reindl, *IEEE Transactions on Electron Devices*, **67**, 6, 2365-2371 (2020).
- [68] A. S. Martin, J. R. Sambles, and G. J. Ashwell, *Phys. Rev. Lett.*, **70**, 218 (1993).
- [69] S. Ruslan and H. Geoffrey, *Neural computation*, **24**(8), 1967-2006(2012).

Acknowledgements

First, I would like to gratefully thank Professor Kunio Awaga for his guidance and support throughout the course of this research. He introduced me to a very attractive scientific field: solid state physics related to organic electronics. I am also indebted to Professor Akiyoshi Hishikawa for his support and comments.

I am extremely grateful to Professor Michio M. Matsushita for kindly instructing me in various experimental techniques, including device fabrications and measurements. I also appreciate the support of Professor Tadashi Sugawara, and his many valuable comments about physical organic chemistry and electronic spintronics.

Thanks also go to my friends, colleagues, and the department faculty and staff for making my time at Nagoya University such a great experience. I'd especially like to thank to Ms. Sayuri Handa, the secretary at Awaga Laboratory for supporting my research lives.

Finally, I offer my sincere thanks to all the members of Awaga Lab and my family.

Daiki Tonouchi

List of publications

- 1) Daiki Tonouchi, Michio M. Matsushita, Kunio Awaga, “Negative differential resistance in the Peierls insulating phases of TTF-TCNQ”, *Phys. Rev. B*, **96**, 045116, 2017.
- 2) Nicholas Black, Daiki Tonouchi, Michio M. Matsushita, J. Derek Woollins, Kunio Awaga and Neil Robertson, “Giant negative magnetoresistance in Ni(quinoline-8-selenoate)₂”, *Physical Chemistry Chemical Physics*, **20**(1), 514-519, 2018.
- 3) Yassine Beldjoudi, Mitchell A. Nascimento, Yong Joo Cho, Hyeonghwa Yu, Hany Aziz, Daiki Tonouchi, Keitaro Eguchi, Michio M. Matsushita, Kunio Awaga, Igor Osorio-Roman, Christos P. Constantinides, and Jeremy M. Rawson, “Multifunctional Dithiadiazolyl Radicals: Fluorescence, Electroluminescence, and Photoconducting Behavior in Pyren-1'-yl-dithiadiazolyl”, *Journal of the American Chemical Society*, **140**(20), 6260-6270, 2018

List of conferences

(Oral)

- 1) ○殿内大輝・松下未知雄・阿波賀邦夫、「TTF-TCNQ のパイエルズ転移に伴う FET 特性と負性微分抵抗」、日本化学会 第 95 春季年会、千葉、2015 年 3 月
- 2) ○Daiki Tonouchi, Michio M. Matsushita, Kunio Awaga, Tadashi Sugawara, “Current-induced mutual conductivity change along orthogonal crystal axes in an ion-radical salt of cyclophane-type donor.”, JSPS Core-to-Core/Leverhulme Trust Joint Workshop, Moscow, 2015/10
- 3) ○殿内大輝・松下未知雄・阿波賀邦夫、菅原正「交差シクロファン型ドナーのイオンラジカル塩における直交する結晶軸間の可逆的な相互導電性変換」、第 25 回有機結晶シンポジウム、京都、2016 年 9 月

- 4) ○Daiki Tonouchi, Michio M. Matsushita, Kunio Awaga, Tadashi Sugawara, “Current-induced mutual structure-conductivity change along orthogonal crystal axes in an ion-radical salt of cyclophane-type donor.”, JSPS Core-to-Core/Leverhulme Trust 5th Joint Workshop, Novosibirsk, 2016/9
- 5) ○Daiki Tonouchi, Michio M. Matsushita, Kunio Awaga, Tadashi Sugawara, “Current-induced mutual structure-conductivity transformation along orthogonal crystal axes in a TTF-based dimeric donor salt”, JSPS Core-to-Core/Leverhulme Trust 6th Joint Workshop, Montreal, 2017/5
- 6) ○殿内大輝・松下未知雄・阿波賀邦夫、菅原正、「交差シクロファンツインドナーのイオンラジカル結晶の対称性の変化を伴う構造相転移の制御」、第13回分子科学討論会、名古屋、2019年9月

(Poster)

- 1) ○殿内大輝・加藤篤史・松下未知雄・阿波賀邦夫、「TTF-TCNQの低温絶縁相における負性抵抗とFET特性」、第8回分子科学討論会、広島、2014年9月
- 2) ○殿内大輝・加藤篤史・松下未知雄・阿波賀邦夫、「TTF-TCNQの低温絶縁相における負性抵抗効果」、第5回分子アーキテクトニクス研究会、大阪、2014年11月
- 3) ○殿内大輝・松下未知雄・阿波賀邦夫・菅原正、「交差シクロファン型ドナー・イオンラジカル塩における構造・物性変化の電流による誘導」、第9回分子科学討論会、東京、2015年9月
- 4) ○Daiki Tonouchi, Michio M. Matsushita, Kunio Awaga, “Negative differential resistance and FET characteristics in TTF-TCNQ at low-temperature”, The 2015 International Chemical Congress of Pacific Basin Societies (Pacifichem2015), Honolulu, 2015/12
- 5) ○殿内大輝・松下未知雄・阿波賀邦夫・菅原正、「交差シクロファン型ドナーのイオンラジカル塩における直交する結晶軸間の抵抗の可逆的相互変換」、日本化学会第96春季年会、京都、2016年3月

- 6) ○殿内大輝・松下未知雄・阿波賀邦夫・菅原正、「交差シクロファン型ドナー・イオンラジカル塩の直交軸間における導電性の可逆的相互変換」、統合物質創製化学研究推進機構キックオフシンポジウム、名古屋、2016年6月
- 7) ○Daiki Tonouchi, Michio M. Matsushita, Kunio Awaga, Tadashi Sugawara, “Current-induced mutual conductivity change along orthogonal crystal axes in a TTF-based dimeric donor salt”, Pre-ICMM, Nagoya, 2016/9
- 8) ○殿内大輝・松下未知雄・阿波賀邦夫・菅原正、「交差シクロファン型ドナー・イオンラジカル塩における直交する結晶軸方向間の抵抗の相互スイッチング」、第7回分子アーキテクトニクス研究会、福岡、2016年10月
- 9) ○殿内大輝・松下未知雄・阿波賀邦夫、「TTF-TCNQのパイエルズ絶縁相における負性微分抵抗」、第11回分子科学討論会、仙台、2017年9月
- 10) ○殿内大輝・松下未知雄・阿波賀邦夫・菅原正、「交差シクロファン型ドナーのイオンラジカル塩における電子物性」、統合物質創製化学研究推進機構第3回国内シンポジウム、京都、2017年10月
- 11) ○殿内大輝・松下未知雄・阿波賀邦夫・菅原正、「交差シクロファン型ドナーのイオンラジカル塩の物性・構造相転移における対イオンおよび結晶化溶媒の効果」、第26回有機結晶シンポジウム、山形、2017年11月
- 12) ○Daiki Tonouchi, Michio M. Matsushita, Kunio Awaga, “Negative differential resistance in the Peierls insulating phases of TTF-TCNQ”, JSPS CtC/Leverhulme Trust 7th Joint Workshop, Nagoya, 2017/11
- 13) ○殿内大輝・松下未知雄・阿波賀邦夫・菅原正、「交差シクロファン型ドナーのイオンラジカル塩における直交する結晶軸間の可逆的な構造・物性制御」、第12回分子科学討論会、福岡、2018年9月
- 14) ○殿内大輝・松下未知雄・阿波賀邦夫・菅原正、「有機導電体結晶中の分子構造変形に基づく導電性の可逆的変化・誘導 (3)」、第10回分子アーキテクトニクス研究会、福岡、2019年11月

- 15) ○殿内大輝・松下未知雄・阿波賀邦夫・菅原正、「電流印加による有機導電性結晶の構造・物性変化」、第 28 回有機結晶シンポジウム、香川、2019 年 11 月

List of awards

- 1) 殿内大輝 第 11 回分子科学討論会(仙台)2017 分子科学会優秀ポスター賞、2017 年 9 月
- 2) 殿内大輝 日本化学会東海支部長賞 2018 年 3 月